Technische Universität München
TUM School of Computation, Information and Technology

Development of Optical Ultrasound Sensors for Optoacoustic Imaging

Tai-Anh La

Vollständiger Abdruck der von der TUM School of Computation, Information and Technology der Technischen Universität München zur Erlangung eines

Doktors der Ingenieurwissenschaften (Dr.-Ing.)

genehmigten Dissertation.

Vorsitz: Prof. Dr.-Ing. Amelie Hagelauer

Prüfende der Dissertation:

1. Prof. Dr. Vasilis Ntziachristos
2. Prof. Dr. Eva Weig

Die Dissertation wurde am 20.11.2023 bei der Technischen Universität München eingereicht und durch die TUM School of Computation, Information and Technology am 10.06.2024 angenommen.

Abstract

Optoacoustic imaging encodes optical absorption into ultrasound, which propagate in tissues with attenuation that is two-three orders of magnitude smaller than light does. Thus, optoacoustic imaging provides rich optical contrast at ultrasonic resolution and penetration depth, opens new windows for observation of structural and functional anatomy inside the living body. Optoacoustic imaging systems usually rely on ultrasound detection based on piezoelectric transducers adopted from classical ultrasonography. While being widely accessible and suitable for early demonstrations, piezoelectric transducers start to possess incompatibilities as the optoacoustic system continues to evolve. Ultrasound detectors using optical resonators were investigated as alternatives for piezoelectric transducers in optoacoustic implementations due to the compatibility of the detection channel with the excitation channel. However, state-of-the-art focused piezoelectric transducer employing $LiNbO_3$ crystal and acoustic lens is strongly favour over optical resonator-based detector as the former features simultaneously high sensitivity, large bandwidth, and a small synthetic aperture, which are all necessary for high-contrast and high-resolution optoacoustic images.

Driven by the clinical demand of minimal invasive optoacoustic imaging and multimodal optic-otoacoustic imaging – where the miniaturization of the optoacoustic imaging hardware is essential, this thesis focused on the development of micrometer-scale optical resonators as ultrasound detectors for optoacoustic systems. After carefully analysing different types of optical resonators, it was proved theoretically challenging for optical resonators to achieve simultaneously comparable sensitivity and resolution to focused piezoelectric transducers.

To overcome the resolution challenge, a novel optical resonator design was proposed, which combines Fabry-Perot etalon with Bragg grating, to drastically shrink the ultrasound detection aperture. A custom modelling approach based on the transfer matrix method was presented as a powerful tool to study the optical properties and a good visual indicator to fabricate this challenging resonator design. Thanks to the modelling, this design was then successfully realized and carefully characterized in the two most common optical platforms: photonic integrated circuits and optical fiber. Remarkably, the new fiber detector (named Embedded Etalon Resonator - EER) has a 30-fold-smaller in physical dimension of state-of-the-art

piezoelectric transducers, while demonstrating comparable imaging resolution and sensitivity. This detector marked the world best catheter as it provides optical contrast with resolution of < 20 µm at millimeter-depth-scale and encapsulated in two fibers with total diameter of less than 400 µm – outperforming all current solutions of intravascular ultrasound and intravascular Optical Coherence Tomography.

Regarding the sensitivity challenge, the insight obtained from analysing the first detector has revealed a new approach for sensitivity enhancement in optical resonator-based ultrasound detectors, which is to maximize the interaction between the ultrasound and the optical fields. This approach has shed light on the principle of one of the most sensitive broad-band optical ultrasound detector to-date called D-shape Fiber Bragg Grating (DFBG). A novel optoacoustic imaging method (named Optoacoustic Mapping of Optical Distribution - OMOD) was developed to visualize the optical energy distribution inside an optical resonator, which is a first-of-its-kind according to the author's knowledge. Using the OMOD method, the interaction between light and ultrasound in the DFBG was precisely controlled at the spatial resolutions of only a few micrometers, leading to unprecedented sensitivity. Side-by-side comparison of the DFBG and high-performance focused piezoelectric transducers employed in commercial optoacoustic systems was conducted to highlight the sensitivity advantage of the DFBG in optoacoustic sensing applications despite the fact that the DFBG is several orders of magnitude smaller than those piezoelectric transducers, enabling optoacoustic contrast to be seamlessly integrated into optical systems.

These developments are expected to facilitate the dissemination of optoacoustic imaging in applications necessitating system miniaturization such as minimally invasive procedures and optical/ optoacoustic hybrid imaging.

Zusammenfassung

Bei der optoakustischen Bildgebung wird die optische Absorption in Ultraschall umgewandelt, der sich im Gewebe mit einer Dämpfung ausbreitet, die zwei bis drei Größenordnungen geringer ist als die von Licht. Daher bietet die optoakustische Bildgebung einen hohen optischen Kontrast bei einer hohen Auflösung und Eindringtiefe des Ultraschalls und eröffnet neue Möglichkeiten zur Beobachtung der strukturellen und funktionellen Anatomie im lebenden Körper. Optoakustische Bildgebungssysteme beruhen in der Regel auf der Ultraschalldetektion mit piezoelektrischen Wandlern, die aus der klassischen Sonographie übernommen wurden. Während piezoelektrischen Wandlern weithin zugänglich und für erste Demonstrationen geeignet sind, beginnen sie mit der Weiterentwicklung des optoakustischen Systems Inkompatibilitäten aufzuweisen. Ultraschalldetektoren, die optische Resonatoren verwenden, wurden aufgrund der Kompatibilität des Detektionskanals mit dem Anregungskanal als Alternativen für piezoelektrischen Wandlern in optoakustischen Anwendungen untersucht. Den fokussierten piezoelektrischen Wandlern mit LiNbO3-Kristall und akustischer Linse ist jedoch dem Detektor mit optischem Resonator vorzuziehen, da er gleichzeitig eine hohe Empfindlichkeit, eine große Bandbreite und eine kleine synthetische Apertur aufweist, die alle für kontrastreiche und hochauflösende optoakustische Bilder erforderlich sind.

Angetrieben durch den klinischen Bedarf an minimalinvasiver optoakustischer Bildgebung und multimodaler optisch-otoakustischer Bildgebung, bei der die Miniaturisierung der optoakustischen Bildgebungshardware von entscheidender Bedeutung ist, konzentrierte sich diese Arbeit auf die Entwicklung optischer Resonatoren im Mikrometerbereich als Ultraschalldetektoren für optoakustische Systeme. Nach sorgfältiger Analyse verschiedener Arten von optischen Resonatoren erwies es sich als theoretische Herausforderung, dass optische Resonatoren eine vergleichbare Empfindlichkeit und Auflösung wie fokussierten piezoelektrischen Wandlern erreichen.

Um das Auflösungsproblem zu überwinden, wurde ein neuartiger optischer Resonator entwickelt, der ein Fabry-Perot-Etalon mit einem Bragg-Gitter kombiniert, um die Apertur für die Ultraschalldetektion drastisch zu verkleinern. Ein kundenspezifischer

Modellierungsansatz, der auf der Transfermatrix-Methode basiert, wurde als leistungsstarkes Werkzeug zur Untersuchung der optischen Eigenschaften und als guter visueller Indikator für die Herstellung dieses anspruchsvollen Resonatorentwurfs vorgestellt. Dank der Modellierung wurde dieses Design dann erfolgreich realisiert und sorgfältig in den beiden gängigsten optischen Plattformen charakterisiert: photonische integrierte Schaltungen und Glasfasern. Bemerkenswerterweise ist der neue Faserdetektor (Embedded Etalon Resonator - EER) um das 30-fache kleiner als moderne piezoelektrischen Wandlern, während er eine vergleichbare Bildauflösung und Empfindlichkeit zeigt. Dieser Detektor markiert den weltweit besten Katheter, da er einen optischen Kontrast mit einer Auflösung von < 20 µm in Millimeter-Tiefe bietet und in zwei Fasern mit einem Gesamtdurchmesser von weniger als 400 µm eingekapselt ist - und damit alle derzeitigen Lösungen für intravaskulären Ultraschall und intravaskuläre OCT übertrifft.

Was die Empfindlichkeit betrifft, so haben die Erkenntnisse aus der Analyse des ersten Detektors einen neuen Ansatz zur Verbesserung der Empfindlichkeit von Ultraschalldetektoren auf der Grundlage optischer Resonatoren aufgezeigt, nämlich die Maximierung der Wechselwirkung zwischen dem Ultraschall und den optischen Feldern. Dieser Ansatz hat das Prinzip eines der bisher empfindlichsten optischen Breitband-Ultraschalldetektoren, des D-förmigen Faser-Bragg-Gitters (DFBG), erhellt. Eine neuartige optoakustische Bildgebungsmethode (Optoacoustic Mapping of Optical Distribution - OMOD) wurde entwickelt, um die optische Energieverteilung in einem optischen Resonator zu visualisieren, was nach Kenntnis des Autors eine Premiere darstellt. Mit der OMOD-Methode konnte die Wechselwirkung zwischen Licht und Ultraschall im DFBG mit einer räumlichen Auflösung von nur wenigen Mikrometern präzise kontrolliert werden, was zu einer noch nie dagewesenen Empfindlichkeit führte. Der Vergleich zwischen dem DFBG und fokussierten Hochleistungs-piezoelektrischen Wandlern, die in kommerziellen optoakustischen Systemen eingesetzt werden, zeigt den Empfindlichkeitsvorteil des DFBG in optoakustischen Sensoranwendungen, obwohl der DFBG um mehrere Größenordnungen kleiner ist als diesen piezoelektrischen Wandlern.

Diese Entwicklungen dürften die Verbreitung der optoakustischen Bildgebung in Anwendungen erleichtern, die eine Miniaturisierung des Systems erfordern, wie z. B. minimalinvasive Verfahren und optisch-optoakustische Hybridbildgebung.

Contents

Acknowledgements

Someone used to say: “PhD research is a tough journey that only rewards men who stand till last”, and I totally agree with this saying. This 4.5-year-journey is one of the most memorable periods of my life, wherein the number of sunny days is as many as the number of miserable nights. The happiness was multiplied by sharing with others, and the difficulties were also simplified by sharing with other. I could never be able to walk through this journey at IBMI without the tremendous support from my friends, my colleagues and my family. I would like to thank the following people from the bottom of my heart:

Prof. Vasilis Ntziachristos, who supervised and support my thesis and research matters. He provides an excellent research environment, allowing conducting state-of-the-art research that is impossible to conduct in any other places. He gave me freedom to word on my research, which is often addressed by insightful comments that enlightened me and pushed me out of my limitation.

Dr. Roman (Rami) Shnaiderman, who directly guided me through my research and the completion of this thesis. He is more like a big brother to me rather than just a group leader. I cannot list all the things that he helped me with in work as well as in life. I am thankful that my PhD life involves having a phone call with him at 10 p.m. from bed, talking about effective sensing length of the sensor; or discussing with him about world’s dictators during optical measurement – which would not happen if I were working with anyone else.

Okan Ülgen, who shared the office and the workspace with me for all my PhD. You always look calm, which really stabilized me a lot when I was shaking from the inside. I was never really into beer that much, but the part of talking to you about life, family, friends and philosophy was what really pulled me 2 miles from walking from lab to Isar river.

And a lot of other colleagues – who did things they might consider small, but mean a lot to me: Dr. Christian Zakian, who always leaves his office door open to all of my questions and would patiently listen to me for hours about some silly ideas. Dr. Andriy Chmyrov, who looks kind of cold from the outside (to me), but his passion and enthusiastic for research had burned up my research ambition for many times. Dr. Yu Shan Huang, who often shared the latest bus with me from Helmholtz to Am Hart and her perspective for life that she shared with me did really reactivate my brain after a long working day. Dr. Jaber Malekzadeh, who always gave me fast but hilarious encounter at the IBMI kitchen on weekends. Dr. Chapin Rodriguez - a true conversational master, who never let me feel left out when he is talking and made me feel really involved into IBMI. Any many other!

The research conducted in this thesis could not be completed without the help of the administration team at IBMI regarding document work and biological sample preparation. My big thanks to Susanne, Andy, Lidia, Ines, Robert, Serene, Elisa and Sarah.

I would like to spend the last past of this section to appreciate my family: my birth parents and my parents-in-law – who are always so sophisticated and stable that I feel safe to lean on; my little girl – the angel that came to me near the end of this journey as a gift and also as a reminder that I should always be strong enough to keep that innocent smile on her face. And finally, to my beloved wife – who I cannot express how grateful I am to have her with me through this whole journey. Ánh, none of any stage in this journey, from the start till the end, could have ever been possible if it was not because of you and for you; and I cannot wait to embark onto the next chapters of my life with you by my side.

List of Figures

List of Tables

List of Abbreviations

1D	1-dimensional
2D	2-dimensional
3D	3-dimensional
AC	Alternating Current
AR	Acoustic-Resolution
BG	Bragg Grating
CAD	Coronary Artery Disease
DC	Direct Current
DFBG	D-shape Fiber Bragg Grating
EER	Embedded Etalon Resonator
FBG	Fiber Bragg Grating
FPR	Fabry-Perot Resonator
FWHM	Full Width Half Maximum
hpBG	Hybrid pi-shifted Bragg Grating
IVUS	Intravascular Ultrasound
MMF	Multimode Fiber
MRI	Magnetic Resonance Imaging
NEP	Noise Equivalent Pressure
NEPD	Noise Equivalent Pressure Density

OCT	Optical Coherence Tomography
OMOD	Optoacoustic Mapping of Optical Distribution
OR	Optical-Resolution
pBG	Pi-shifted Bragg Grating
pFBG	Pi-shifted Fiber Bragg Grating
PhC	Photonics Crystal
PIC	Photonics Integrated Circuit
PMF	Polarization Maintaining Fiber
PSF	Point Spread Function
RSOM	Raster-Scanning Optoacoustic Mesoscopy
SAW	Surface Acoustic Wave
SNR	Signal-to-Noise Ratio
SOF	Silica Optical Fiber
SOI	Silicon-On-Insulator
SPF	Side Polished Fiber
SWED	Silicon Waveguide Etalon Detector
TMM	Transfer Matrix Method
WGB	Waveguide Bragg Grating
WGM	Whispering Gallery Mode

Chapter 1 : Introduction

1.1 Biomedical imaging

Biomedical imaging is one of the most important biomedical tools. It has impact spreading from fundamental biological research to applied medicine and engineering. The general structure of a biomedical imaging system is depicted in Figure 1.1. Therein, an emitter generates a physical excitation toward the imaging object - which could be cells/ tissues, organs, small animals, or whole human body. Inside the imaging object, there exists contrast agents that alter the physical excitation by a mechanism called “contrast mechanism”. Under the contrast mechanism, the physical excitation could either be attenuated in intensity, changed in phase, converted into other type of physical quantities, etc. and then escapes the imaging object under the form of a physical output – which carries the information about the contrast agents. A detector collects the physical output and performing relevant processing steps to produce the final image of the contrast agents inside the imaging object.

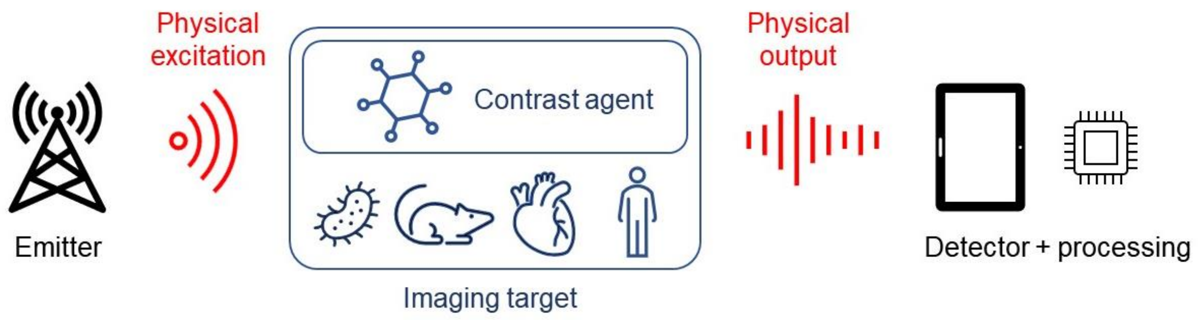

Figure 1.1 - General structure of biomedical imaging systems. An emitter emits a certain excitation toward the imaging target, which triggers the contrast agent inside the target to response to the excitation and release a physical response. This output is captured by a detector before processing and displaying of the image.

Table 1.1 presents the physical excitations, contrast mechanisms and physical outputs of several popular imaging modalities. Depending on the desired contrast, the proper imaging modality should be chosen for specific applications. Apart from the contrast mechanism, other important properties of an imaging modality are spatial resolutions and penetration depth. Obviously, one always wishes to image with highest possible resolution at deepest possible penetration depth. However, this is not technically possible regardless of imaging modalities, as the common depth per resolution ratios of most imaging modalities often fall around 100 (Figure 1-2).

Table 1.1 - Properties of several popular imaging modalities

Modalities	Excitation	Output	Contrast mechanism
Optical microscopy	Light	Light	Optical scattering
Ultrasonography	Ultrasound	Ultrasound	Elastic scattering
X-ray Computed Tomography (XCT)	X-ray	X-ray	X-ray absorption
Magnetic Resonance Imaging (MRI)	Radio frequency wave	Magnetic field	Relaxation of hydrogen atoms
Optoacoustic Imaging	Light	Ultrasound	Optoacoustic effect

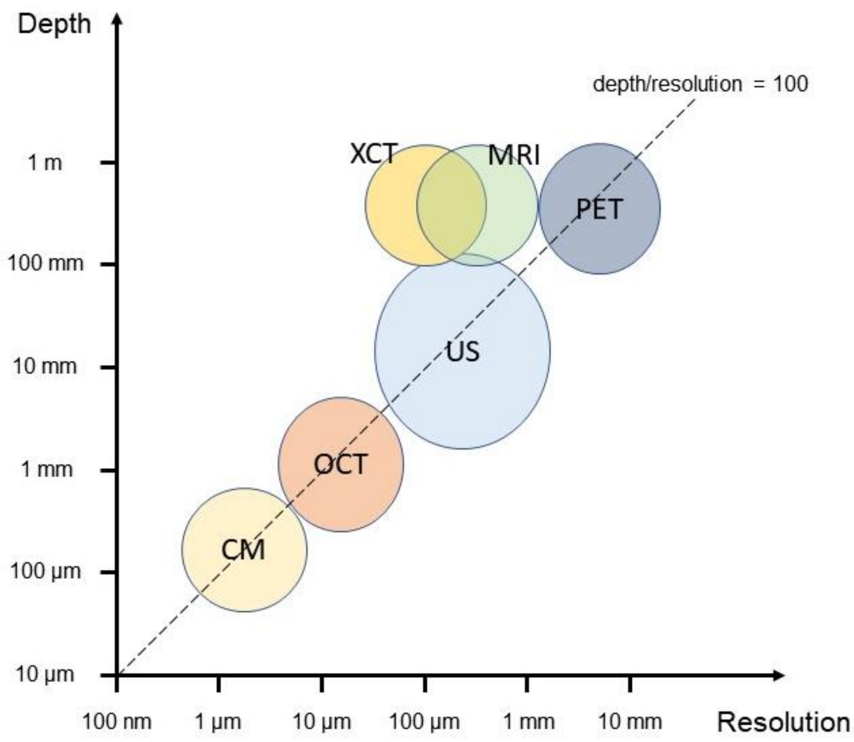

Figure 1.2 - Imaging depth versus resolution of different imaging modalities. CM: Confocal Microscopy, OCT: Optical Coherence Tomography, US: Ultrasonography, PET: Positron Emission Therapy, MRI: Magnetic Resonance Imaging, XCT: X-ray Computed Tomography.

1.2 Motivation

Optoacoustic imaging or photoacoustic imaging is a fast-growing imaging modality that offers an alternative to purely optical imaging modalities. In optoacoustic imaging, the physical excitation is light, which is often delivered by a laser to provide sufficient optical energy. Under specific conditions, light is absorbed and the optical energy is converted to mechanical energy via the contrast mechanism called "optoacoustic effect" [1]. This mechanical energy escapes the imaging object as ultrasound wave and is captured by ultrasound detectors. Even though the optoacoustic effect has been discovered more than 100 years ago, optoacoustic imaging was only demonstrated two decades ago thanks to advancement of both laser technology and piezoelectric fabrication [2,3].

In the initial stage of optoacoustic imaging, the adaptation of piezoelectric transducers from classical ultrasonography for ultrasound detection had enable quick and effective optoacoustic imaging systems. However, as optoacoustic imaging systems evolved quickly to meet the custom requirements for specific applications, piezoelectric transducers have shown several incompatibilities with optoacoustic imaging. First, piezoelectric transducers are optically opaque, which often lead to sub-optimal optical excitation. Recently, transparent piezoelectric transducers have been demonstrated to increase the compatibility of piezoelectric transducers with optoacoustic imaging [4], but the degree of transparency has not yet to be really consider "transparent" and the fabrication possesses many challenges at large scale production. Secondly, in applications that necessitate multimodal imaging, piezoelectric transducers induce several technical problems such as being sensitive to electro-magnetic interference, which is problematic when cooperating optoacoustic with magnetic resonance imaging. Most importantly, piezoelectric transducers have their sensitivity degrade quadratically with dimension, significantly reducing the performance of optoacoustic imaging systems in applications that favor hardware miniaturization such as minimally invasive guidance and diagnosis.

Ultrasound detectors based on optical methods have been increasingly considered to replace piezoelectric transducers on optoacoustic imaging systems due to their optical transparency, the immunity to electro-magnetic interference and the great miniaturization capability. However, optical ultrasound detectors remain unfavored because their advantages have not yet overshadowed their limited performance.

Nevertheless, in some important applications, the miniaturization of the imaging system (or at least the imaging probe – which includes the ultrasound detector and the optical illumination unit) is absolute essential. Typical examples could be:

- Intravascular imaging: intravascular catheter is an important tool to diagnose the atherosclerosis associated with coronary artery disease (CAD) [5]. Herein, the imaging probe in inserted into the artery to measure the fibrous cap thickness, which has the value of approximately 23 µm for ruptured plaques [6]. Accurate measurement of the fibrous cap thickness is the major task for intravascular imaging in CAD diagnosis, and this task requires the imaging resolution of 20 µm or better. In addition, the imaging probe should be small enough to fit into standard catheters, which have the smallest diameter of only 1 mm (3F sheath). The most common modality for intravascular imaging is intravascular ultrasound (IVUS). Conventional IVUS sheath provides (axial) resolution of approximately 50-150 µm, which is insufficient for accurate measurement of the cap thickness. OCT has recently applied in intravascular imaging as the optical contrast provided greatly improves the accuracy of the measurements and the resolution could easily reach < 20 µm. However, the penetration depth of OCT is shallow (< 1 mm in tissue) [7]. Optoacoustic could combine the resolution of OCT and penetration depth of ultrasound, bringing unprecedented value for intravascular imaging. Nevertheless, the miniaturization of optoacoustic hardware has been proven challenging due to the size of the piezoelectric transducers used, leading to probe diameter of > 3 mm[8,9].
- Hybrid optical/ optoacoustic imaging: the combination of different contrast mechanisms has shown great values in studying biological process using multi-modal optical microscopy [4,10]. Due to the optical opacity and bulkiness of piezoelectric transducers, conventional approaches to integrate optoacoustic into multimodal microscopy includes using either transmission-mode with piezoelectric transducers located on the other side of the objective, or acoustic mirror to separate the optical path from acoustic path. The former approach is not as favorable as reflection-mode microscope due to the capability of imaging thick samples or samples with restricted access from one side only. The latter approach increases the distance between the objective and the sample and prevents the usage of high numerical aperture (NA) objective for high spatial resolution. Miniaturized and transparent ultrasound detectors

using optical resonators [11] have been proven to allow seamless integration of optoacoustic into multi-modal microscopy with minimal interference on the optical path.

Therefore, it is imperative that the miniaturization of ultrasound detectors should not sacrifice the detector's performance, i.e., its detection bandwidth and sensitivity.

1.3 Objective

Following the analysis presented Section 1.2, the research presented in this thesis aims to theoretically investigate and experimentally demonstrate new optical ultrasound detectors that are expected to replace piezoelectric transducers in specific applications that necessitate hardware miniaturization. The detailed objectives are as follows:

1. Conduct a general analysis about state-of-the-art technologies for optical ultrasound detectors from the viewpoint of optoacoustic imaging. From the theoretical framework of optoacoustic imaging, the thesis should elaborate on specific requirements of an ultrasound detector to achieve good imaging performance, i.e., high resolution and high contrast. These requirements then should be projected onto current detector technologies to analyze whether those requirements can be meet, and what should be further considered to address those requirements.

2. Demonstration of a new optical ultrasound detector that is capable of address the requirements pointed out in the literature review, thus providing unprecedented imaging resolution and sensitivity for intravascular endoscopic applications. The demonstration should involve both theoretical analysis and experimental measurements to support the claims of the imaging performance.

3. From the detector demonstrated, conducting further analysis on the finding and new physical insight into the process of ultrasound detection using light. This objective was defined only at a late stage of this research, but could pave the way for further improvement of imaging performances for next generation of optical ultrasound detectors

1.4 Thesis Outline

This dissertation is structured into six chapters:

Chapter 1 gives a brief intuition about optoacoustic imaging in the context of biomedical imaging and the challenge for future development – which motivated the conduction of this research.

Chapter 2 provides fundamentals of optoacoustic imaging, in particular the theory of the optoacoustic image formation and the physical implementation of the modalities (microscopy, tomography and mesoscopy).

Chapter 3 focuses on the most promising type of optical structure for detector construction: optical resonators. Various settings of optical resonators are discussed regarding their physical configuration and properties that directly affect their imaging performance.

Chapter 4 proposes a new optical ultrasound detector based on optical resonator in fiber that possesses an unprecedented combination of resolution and sensitivity. The theoretical tool is presented to study the physics of the detector. Experimental data is shown to justify the characteristics and imaging performance of the new detectors.

Chapter 5 presents a different optical ultrasound detector which achieves one of the highest sensitivities ever reported for optical ultrasound detector. The premise of this detector follows the new physical insights provided by the detectors presented in Chapter 4. Size-by-size comparison with state-of-the-art piezoelectric transducers employed in commercial optoacoustic imaging systems are exhibited to highlight the sensitivity of the new detector.

Chapter 6 completes the dissertation by summarizing all the findings of this research and discussing potential outcomes.

Chapter 2 : Optoacoustic Imaging and Optoacoustic Modalities

2.1 Introduction

Optoacoustic imaging is a "light in, sound out" technique. The special combination of light and ultrasound distinguished optoacoustic from either pure optical- or pure ultrasound- based imaging modalities due to several special requirements for optoacoustic effect to be triggered. This chapter deals with the most fundamental mechanism of optoacoustic imaging, followed by a reviews of current optoacoustic imaging systems, their working principles and potential applications.

2.2 The Optoacoustic Effect

2.2.1 Overview of optoacoustic systems

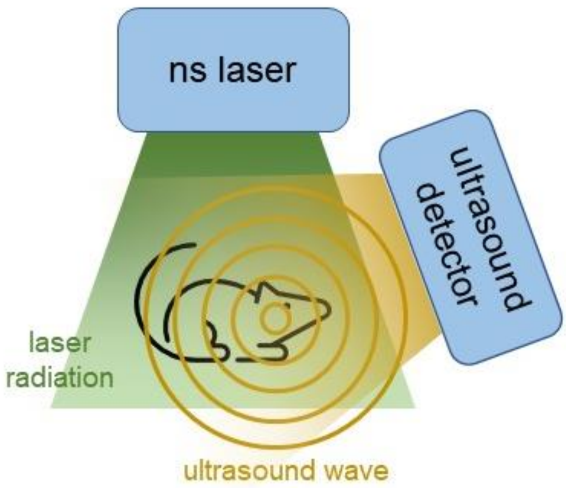

Figure 2.1 - Optoacoustic imaging systems. ns laser stands for nano-second laser – which is the conventional choice for optoacoustic imaging systems.

In order to harvest optoacoustic effect for biomedical imaging, a typical system as depicted in Figure 2-1 is required. Here, the biological sample is irradiated by non-ionizing laser pulses. Due to relevant absorbers that exist inside the sample, optical energy is absorbed and converted into thermal energy. Under some special conditions that will be discussed in detail in Section 2.2.2, the subsequent heating process induces thermo-elastic expansion in the form of ultrasound wave. These ultrasound signals are then recorded using an ultrasound detector and processed to produce an image of the optical absorbers.

Optoacoustic imaging system combines optical excitation and ultrasonic detection. On the excitation side, the laser wavelength can be varied greatly depending on the desired absorbers or penetration depth [12]. On the illumination side, the well-developed piezoelectric technology makes them the conventional choice [13]. However, as will be analyzed in section 2.2.3, the ultrasound signal generated from optoacoustic effect has unusual properties when being compared with ultrasonography, making piezoelectric detector case-by-case not the ideal choice.

2.2.2 Conditions for the generation of the optoacoustic signal

Not any arbitrary kind of laser excitation can generate proper optoacoustic signal. There are several different mechanisms of interaction between light and biological samples, and only under special conditions that optoacoustic effect occurs [14]. This section reviews those conditions and how the initial optoacoustic signal depends on the intrinsic properties of the optical excitation and the sample itself.

For an ideal volume with spherical shape and diameter d_V, the thermal diffusion time τ_{th} is defined as the time duration for internal heat to diffuse into the surrounding medium and is given by:

$$\boldsymbol{\tau_{th} = \frac{d_V^2}{\alpha_{th}}} \qquad \mathbf{(2.2.1)}$$

where α_{th} is the thermal diffusivity of the volume's material. If the optical excitation time is shorter than τ_{th}, the heating is then localized in space. This condition is referred as "heat confinement".

The stress relaxation time τ_S is defined as the time duration for internal stress to propagate outside of the mentioned volume and is given by:

$$\tau_S = \frac{d_V}{v_s} \qquad (2.2.2)$$

where υ_s is the speed of sound of the volume's material. If the duration of the laser excitation is shorter than τ_S, the excitation can be assumed instantaneous and the optoacoustic signal generation is localized in time. This condition is referred as "stress confinement".

In order to achieve good signal-to-noise ratio (SNR) and spatial resolution, both heat confinement and stress confinement conditions should be satisfied. A typical biological absorber has $d_V = 50\ \mu\text{m}$, $\alpha_{th} = 0.1\ \text{mm}^2/\text{s}$ and $\upsilon_s = 1500\ \text{m}/\text{s}$, which give $\tau_{th} = 25\ \mu\text{s}$ and $\tau_S = 33.33\ \text{ns}$. A pulse laser with pulse duration in the order of few nanoseconds therefore becomes the standard for excitation source in optoacoustic imaging. Even though optoacoustic effect had been discovered for one hundred year [1], it has to wait for the explosion of high-speed Q-switch laser with nanoseconds pulse duration in the last couple of decades to become a powerful tool in biomedical imaging.

In such case, the heat energy is immediately converted into pressure. The initial induced pressure p_0 at a given point $\boldsymbol{r}$ can be expressed as:

$$p_0(\boldsymbol{r}) = \Gamma H(\boldsymbol{r}) = \Gamma\mu_a(\boldsymbol{r})\Phi(\boldsymbol{r}) \tag{2.2.3}$$

where $H(\boldsymbol{r})$ is absorbed optical energy distribution, $\mu_a(\boldsymbol{r})$ is the local absorption coefficient and $\Phi(\boldsymbol{r})$ is the optical fluence. Γ is known as the Grüneisen coefficient (dimensionless), represents the measure of the amount of thermal energy converted into pressure and thus can be interpreted as the optoacoustic conversion efficiency. The final optoacoustic image is a representation of p_0 in space. Assuming a constant Grüneisen coefficient and homogeneous illumination over the whole imaging volume, the optoacoustic image can be considered as a map of local absorption coefficient of the corresponding optical wavelength.

2.2.3 Optoacoustic signal in homogeneous and lossless medium

After being generated, the initial pressure p_0 has to propagate with ultrasonic frequency through tissue and ultrasound coupling medium to reach the ultrasound detector. In order to resolve the p_0 map accurately, it is important to understand all the processes that happen in between the source and the detector. This section takes in to account the propagation of ultrasound wave in homogeneous and lossless medium, while the next section deals with phenomena that happen in real imaging condition.

The propagation of optoacoustic wave in homogeneous and lossless medium can be asserted accurately using the acoustic wave equation:

$$\left(\nabla^2 - \frac{1}{v_s^2}\frac{\partial^2}{\partial t^2}\right)p(\boldsymbol{r},t) = -\frac{\Gamma}{v_s^2}\frac{\partial}{\partial t}H(\boldsymbol{r},t) \tag{2.2.4}$$

where the source term $H(\boldsymbol{r},t)$ is the product of the absorbed optical energy distribution $H(\boldsymbol{r})$ and the temporal profile of the excitation pulse $H(t)$. By using pulse duration in the order of nanosecond, the heating can be assumed instantaneous and thus $H(t) \approx \delta(t)$, with $\delta(t)$ represents the Dirac-delta function.

The Green's function of the operator on the left side of Equation 2.2.4 is well-known to have the form:

$$G(\boldsymbol{r},\boldsymbol{r}',t) = \frac{\delta\left(t - \frac{|\boldsymbol{r}-\boldsymbol{r}'|}{v_s}\right)}{4\pi|\boldsymbol{r}-\boldsymbol{r}'|} \tag{2.2.5}$$

The propagating acoustic pressure $p(\boldsymbol{r},t)$ then has the general form:

$$p(\boldsymbol{r},t) = \frac{1}{4\pi v_s^2}\frac{\partial}{\partial t}\left[\frac{1}{v_s t}\int p_0(\boldsymbol{r}')\delta\left(t - \frac{|\boldsymbol{r}-\boldsymbol{r}'|}{v_s}\right)d\boldsymbol{r}'\right] \tag{2.2.6}$$

In a typical case of optoacoustic imaging, the absorber is a sphere with radius a and absorption coefficient μ_a under homogeneous radiation with fluence Φ. The time-dependent acoustic field at a distance r from the center of the sphere then can be simplified as:

$$p(r,t) = \frac{a\mu_a\Gamma\Phi}{2r}(1-\hat{\tau})\Xi_{0,2}(\hat{\tau}) \tag{2.2.7}$$

where $\hat{\tau}$ is a dimensionless retarded time expressed as:

$$\hat{\tau} = \frac{v_s}{a}\left(t - \frac{r-a}{v_s}\right) \tag{2.2.8}$$

and $\Xi_{0,2}(\hat{\tau})$ is a boxcar function such that $\Xi_{0,2}(\hat{\tau}) = 1$ if $\hat{\tau} \in [0,2]$ and 0 otherwise. Using Equation 2.1.7, the ultrasound signals generated from three spherical absorbers made by the same material and different sizes were simulated as in Figure 2.2. All the signals are recorded by a virtual detector placed at a distance of 1 mm from the center of the sphere.

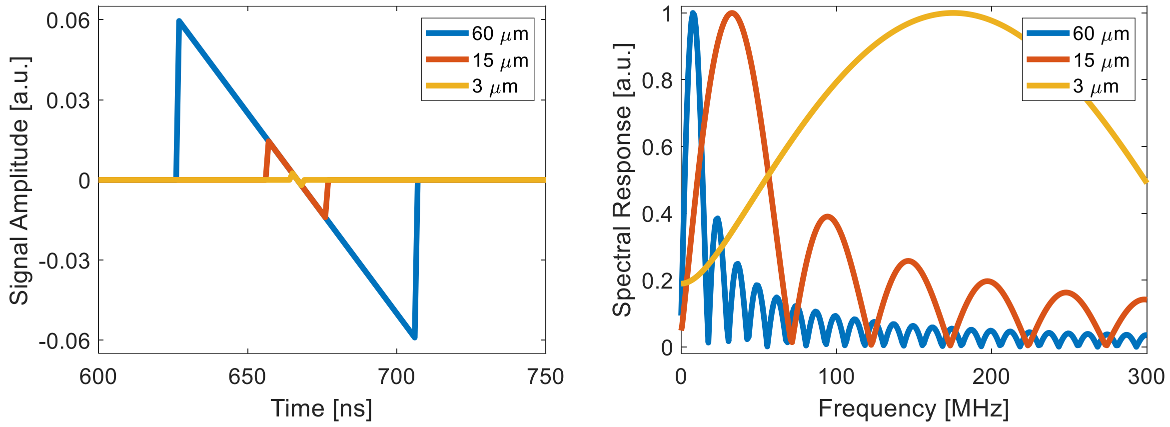

Figure 2.2 - Simulated optoacoustic signals generated by spherical absorbers of different radiuses. (a) Signals in time-domain from three absorption spheres with radius of 60 µm, 15 µm and 3 µm. (b) The corresponding spectrums of the three signals in (a).

Some interesting properties can be observed from Equation 2.2.7 and Figure 2.2. Regarding the signal in time-domain, the signal amplitude is proportional to the size of the absorber and inversely proportional to the distance from the absorber to the detector. The former can be interpreted as large objects absorbs more optical energy and thus produces stronger acoustic pressure, while the later property is due to the spherical spreading of the optoacoustic wave.

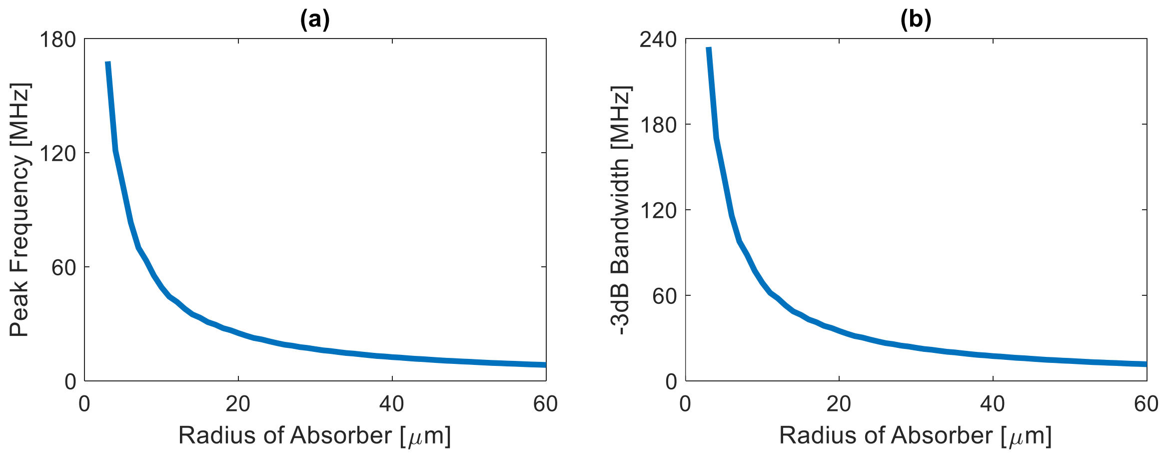

Figure 2.3 - Spectral properties of optoacoustic signals generated by spherical absorbers of different sizes. (a) Peak frequency. (b) Bandwidth of generated OA signals.

Regarding the frequency component, the smaller absorber emits higher frequency and spreads over a larger bandwidth. These spectral properties are illustrated in detail in Figure 2.3. The peak frequency component and the respective -3 dB bandwidth of the optoacoustic emission spectrum were plotted for absorbers with a large size range. It can be clearly seen that the trends increase rapidly when the radius of the object becomes less than 15 µm, inferring a much heavier burden on the ultrasound detector in order to collect the optoacoustic signal efficiently. For example, detecting optoacoustic signal of a human egg (~ 50 µm in radius) requires an ultrasound detector with 10 MHz center frequency and 14 MHz bandwidth. On the other hand, effectively harvesting optoacoustic signal of an object that has similar size of a red blood cell (~ 4 µm in radius) craves an ultrasound sensor covering the frequency range from 35 to 215 MHz, which cannot be reasonably satisfied with conventional medical ultrasound transducers.

2.2.4 Propagation-related phenomena

a) Attenuation

While propagating in tissue and ultrasound coupling medium, optoacoustic wave loses energy due to viscous losses in the medium. Acoustic attenuation is dependent on the frequency of the wave and the thermodynamical properties of the medium [15]. Despite being small for the frequency below 30MHz, this attenuation becomes trivial for high frequency band and cannot be neglected.

The ultrasonic attenuation coefficient $\propto (f)$ in a wide range of lossy media has been established empirically to have the form [16]:

$$\propto (f) = \propto_{0f} \, |f|^n \tag{2.2.9}$$

where $\propto_{0f}$ is the attenuation constant and n is a positive number. In water, the power number n was experimentally measured to be approximately 2 and the attenuation constant $\propto_{0f} = 0.00217$ dB.MHz^{-2}.cm^{-1}, while $n \approx 1$ and $\propto_{0f} \approx 0.5$ dB.MHz^{-1}.cm^{-1} for many biological tissues [15]. Figure 2.4(a) illustrates the average attenuation coefficient for water and tissue as a function of optoacoustic frequency.

Because optoacoustic signal of high frequency (>100 MHz) attenuates at a much higher rate than the low frequency components, the detected signal has a narrower spectrum than the originally emitted signal. Therefore, the optoacoustic gets broaden in time-domain during propagation as a consequence of the frequency-dependent signal attenuation. Assuming the initial pressure p_0 having the form of a Dirac's delta function with negligible pulse width, the pulse with of the optoacoustic signal as a function of imaging distance r in tissue Δt_t and in water Δt_w can be given by [17]:

$$\Delta t_t = 2\alpha_{0\omega,t} r \tag{2.2.10}$$

and

$$\Delta t_w = 4\sqrt{\alpha_{0\omega,w} ln2} \tag{2.2.11}$$

The pulse width broadening effect is illustrated in Figure 2.4(b). Within the scope of this thesis, the interesting imaging depth generally lies between 0 and 1 cm, so the signal broadening effect can be neglected.

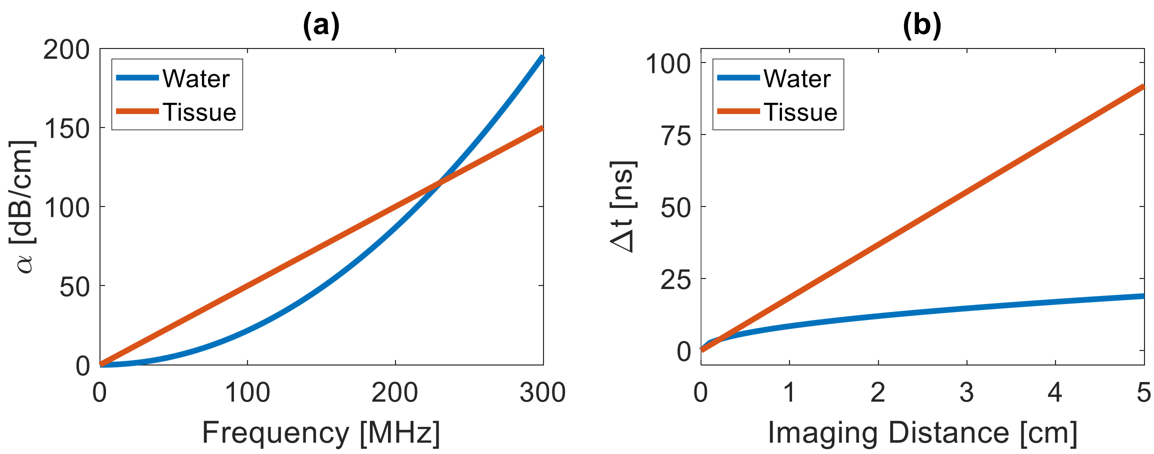

Figure 2.4 - The effect of ultrasound attenuation to optoacoustic signals in water and in tissues. (a) Attenuation coefficient with respect to frequency. (b) Pulse width broadening as a function of imaging distance.

b) Refraction and Reflection

Similar to the way electromagnetic wave being reflected and refracted from interface between two mediums having different optical properties, ultrasound wave experiences the same effect from interface between two medium having different acoustic properties.

In analogy to the refractive index of electromagnetic wave propagation, the acoustic impedance Z is introduced to represent the acoustic properties of a medium and is defined as:

$$Z = \rho v_s \tag{2.2.12}$$

where ρ is the density and υ_s is the speed of sound of the medium. Acoustic impedance of some relevant medium in this thesis are given in Table 2.1.

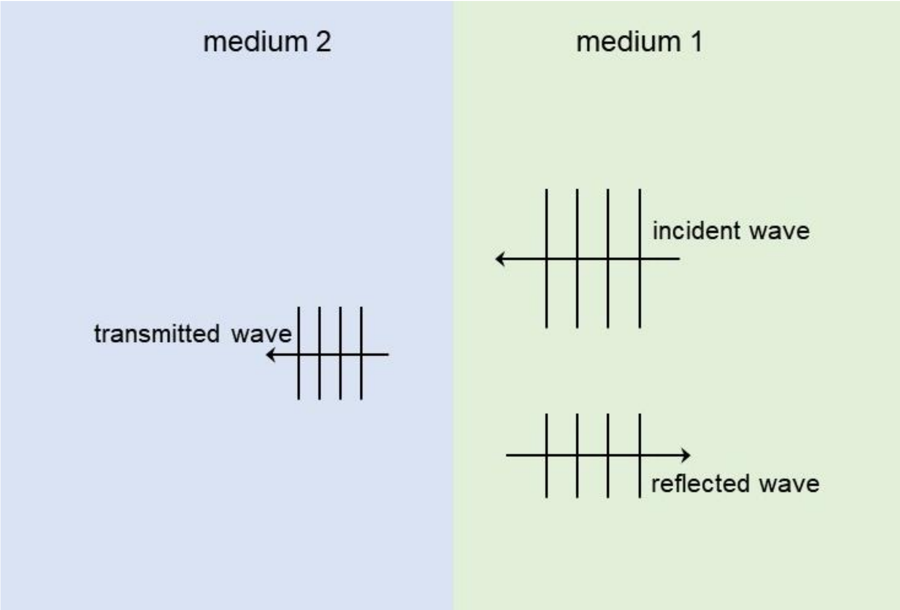

Figure 2.5 - Ultrasound reflection from an acoustic interface.

When propagating from a medium with acoustic impedance Z_1 to another medium with acoustic impedance Z_2, ultrasound is reflected with the reflection coefficient given by:

$$r = \frac{p_r}{p_i} = \frac{Z_2 - Z_1}{Z_2 + Z_1} \tag{2.2.13}$$

The transmission coefficient is:

$$t = \frac{p_t}{p_i} = \frac{2Z_2}{Z_2 + Z_1} \tag{2.2.14}$$

The corresponding reflectance and transmission are given by:

$$R = r^2 = \left(\frac{Z_2 - Z_1}{Z_2 + Z_1}\right)^2 \tag{2.2.15}$$

and

$$T = \frac{Z_1}{Z_2} t^2 = \frac{4Z_2 Z_1}{(Z_2 + Z_1)^2} \tag{2.2.16}$$

Note that $R + T = 1$ is always satisfied, which represents the law of conservation of energy.

It should be noted that the interpretation of acoustic reflection and transmission from an acoustic boundary in this section is simplified to the case of normal incident and longitudinal acoustic wave propagation only - which holds true for liquid-liquid interface or liquid-tissue interface only. Once the interface with solid and oblique incidence is considered, the situation becomes rather complex due to the existence of various types of acoustic waves in solid. A full derivation in such cases can be found in other references [18].

Table 2.1 - Acoustic properties of some relevant materials

Materials	Density [kg/m^3]	(Longitudinal) Speed of sound [m/s]	Acoustic impedance [MRay]
Air	1.23	340	0.0004
Water	999	1480	1.48
Tissue	1050	1500	1.58
Glass (silica)	2500	5000	12.50
Silicon	2330	8200	19.11

2.3 Optoacoustic Imaging Modalities

2.3.1 Optoacoustic microscopy

Optoacoustic microscopy can be categorized into optical-resolution (OR) and acoustic-resolution (AR) optoacoustic microscopy. OR optoacoustic microscopy utilizes an objective lens with high numerical aperture to tightly focus light onto a micrometer-size spot, which determines the lateral resolution. On the other hand, AR optoacoustic microscopy relies on a focused ultrasound detector with the lateral resolution is the size of the detector's focal spot. In general, because optical wavelength is much smaller than ultrasound wavelength, light can be focused to a smaller spot than ultrasound can be. Therefore, OR optoacoustic microscopy normally achieves a finer lateral resolution than AR optoacoustic microscopy, albeit at more superficial imaging depth due to strong optical scattering in tissue. OR optoacoustic microscopy with lateral resolution of 0.22 µm at < 0.1 mm depth has been demonstrated [19], while AR optoacoustic microscopy could produce ~ 45 µm lateral resolution at depth of approximately 3 mm [20,21]. In both modalities, the axial resolution R_a is defined by the detection bandwidth of the employed ultrasound sensor through the same relation [22]:

$$R_a = 0.88 \frac{v_s}{f_{BW}} \quad (2.3.1)$$

where f_{BW} is the detection bandwidth of the ultrasound detector.

The image is conventionally formed by directly assessing the time-resolved ultrasound signal obtained at each scanning point with maximum amplitude or maximum intensity projection. To fully retain the characterized resolution of the optoacoustic microscopy system, the scanning step should be retained smaller than half of the lateral resolution to satisfy the Nyquist sampling condition.

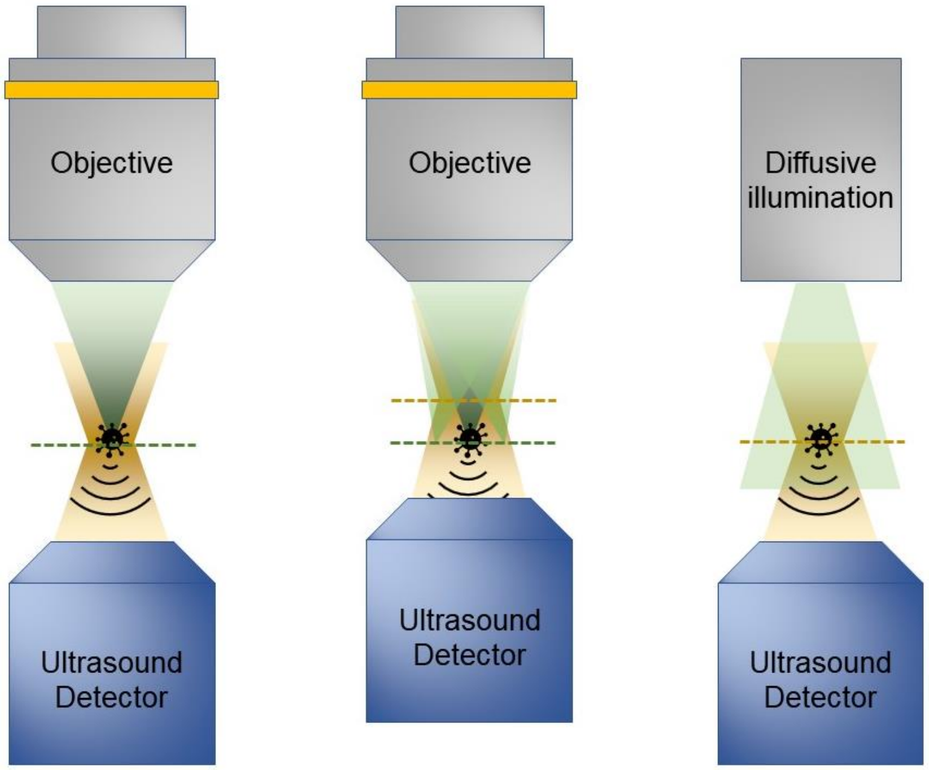

Figure 2.6 - Optoacoustic microscopy: Optical resolution (OR - left and middle) and acoustic resolution (AR - right). The green region depicts the optical illumination field. The yellow region depicts the sensitivity field of the ultrasound detector. The green dashed line denotes the focal plane of the optical focus. The yellow dashed line denotes the focal plane of the acoustic focus.

Even though acoustic focusing is not a must in OR optoacoustic microscopy, majority of OR optoacoustic microscopy systems use focused ultrasound detectors due the great advantage of sensitivity enhancement. Figure 2.6 illustrates popular configurations of optoacoustic microscopy systems. In the first configuration of OR optoacoustic microscopy, the microscope objective and ultrasound detector are co-focused, resulting in the overlap of the acoustic and optical focal planes. Herein, in order to obtain a volumetric image, the sample is normally raster-scanned using a two-dimensional translation stage. The scanning speed of the stage and the repetition rate of the laser are usually the rate-determining steps of the imaging process. For example, to raster scan 200×200 points within 1 s and 2 μm-step size, the laser pulse repetition rate must be at least $40\,\mathrm{kHz}$ and the stage has to travel with average speed of $80\,\mathrm{mm/s}$. While state-of-the-art pulse laser can provide repetition rate in the order of few hundreds kHz, it is challenging for mechanical linear stages to move much faster than $100\,\mathrm{mm/s}$ but still maintains highly precise motion. One common solution to circumvent this limitation is to employ the galvanometric mirrors to scan the optical beam, as depicted in the middle scheme of Figure 2.6 [23]. Herein, the optical focus is scanned over the optical focal plane with speed as fast as hundreds of kHz. However, a drawback of this configuration is the acoustic focal spot commonly does not sufficiently cover the optical scanning region. Therefore, the focused ultrasound detector has to be defocused, leading to a reduction in the sensitivity of the optoacoustic microscopy system. For AR optoacoustic microscopy, the combination of the ultrasound detector and the optical illumination is often raster-scanned rather than the sample [20,21].

2.3.2 Optoacoustic tomography

In optoacoustic tomography, light is diffused and ultrasonic detection is performed by an array (Figure 2.7). Depending on the intended applications, real physical implementation of optoacoustic tomography can be configured with 1D ultrasonic detector array, 2D ultrasonic detector array or a virtual scanning detector array [24,25].

Unlike in AR optoacoustic microscopy, where high-frequency ultrasound detection is employed, optoacoustic tomography detects low frequency ultrasound (e.g., 5 MHz) [26]. The penetration depth therefore is limited by optical fluence dissipation rather than ultrasound attenuation and could reach up to 7 cm [26]. The axial resolution R_a and lateral resolution R_l in optoacoustic tomography can be estimated by the following equations [27]:

$$R_a \approx 0.8 \frac{v_s}{f_c} \tag{2.3.2}$$

and

$$R_l = \sqrt{R_a^2 + \phi^2} \tag{2.3.3}$$

where f_c is the cut-off frequency of the ultrasound detector and ϕ is the aperture size of a single detector element. The spatial resolution of optoacoustic tomography is relaxed to few hundreds of micrometers as the consequence of the low ultrasonic frequency and large element size of the transducer array [25].

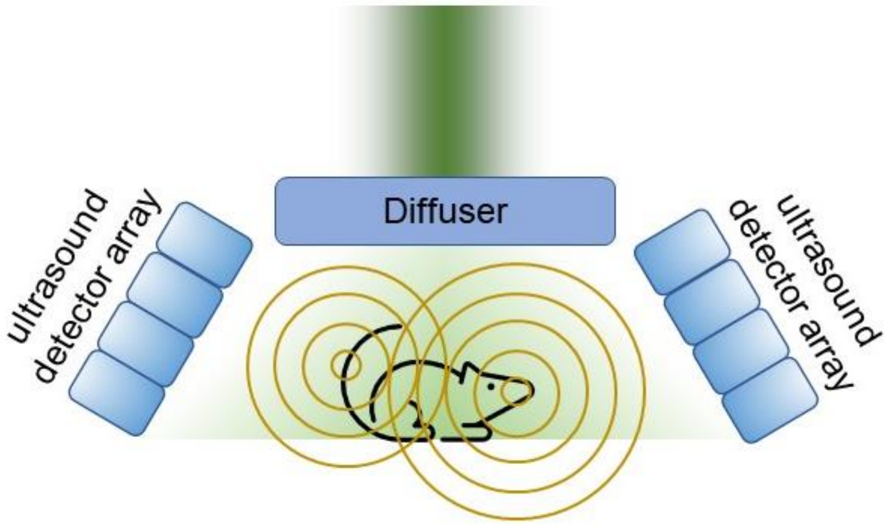

Figure 2.7 - Configuration of the optoacoustic tomography systems.

Because the whole object is illuminated, every absorber emits ultrasound at the same time. The recorded signal from a single sensor is the superposition of optoacoustic signals from all the absorbers in the object. Therefore, a reconstruction algorithm is required to form an image from the collected data. The most popular reconstruction algorithm is the back-projection in the time domain [28]. In this algorithm, the initial pressure $p_0(\boldsymbol{r}')$ is back-propagated by inverting equation 2.2.6:

$$p_0(\boldsymbol{r}') = \int \left[2p(\boldsymbol{r}, t) - 2t \frac{\partial p(\boldsymbol{r}, t)}{\partial t} \right] |_{t=|r'-r|/v_s} \frac{d\Omega}{\Omega_0} \quad (2.3.4)$$

where $d\Omega/\Omega_0$ is the weighting factor which presents the solid angle subtended by the point $\boldsymbol{r}'$ at the sensor position $\boldsymbol{r}$.

Theoretically, using 2D ultrasound array can generate a complete 3D image of the object with a single laser pulse. However, multiplexed data acquisition is often employed to reduce the overall system cost. The speed of the multiplexed data acquisition process in combination with the pulse repetition rate of the laser sets a limit on imaging speed of OAT. 3D OAT imaging system with real-time rate up to $50\,\text{Hz}$ over a $15 \times 15 \times 7\,\text{mm}^3$ field-of-view has been demonstrated [29].

2.3.3 Optoacoustic mesoscopy

Optoacoustic mesoscopy is an emerging technology that bridges the gap between optoacoustic microscopy and tomography. Optoacoustic mesoscopy combines tomographic reconstruction method with a physical system that employs high frequency ultrasound detectors of optoacoustic microscopy in a raster-scan [30,31] or a curved detection surface [32] (Figure 2.8).

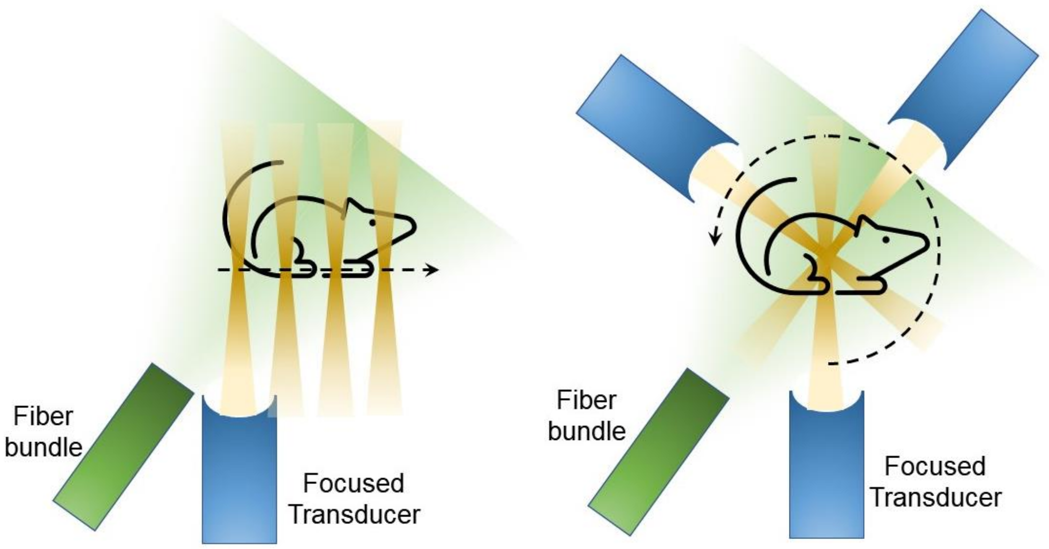

Figure 2.8 - Optoacoustic mesoscopy configurations: raster scanned (left) and curved scanned (right). The green region depicts the optical excitation region. The yellow region depicts the sensitivity field of the focused ultrasound detector.

Despite providing a better image quality than the raster-scanned geometry, curved detection optoacoustic mesoscopy requires sample access from an enclosed surfaced around the sample, which is not well-fitted for many biomedical applications. Within the scope of this thesis, raster scanned optoacoustic mesoscopy (RSOM) remains the interested modality and is inherently inferred when mentioning optoacoustic mesoscopy.

By employing detection frequency up to > 100 MHz, optoacoustic mesoscopy could visualize biological structure with lateral resolution below $100\ \mu\text{m}$ at penetration depth of almost 10 mm [30]. The spatial resolution of optoacoustic mesoscopy follows equation 2.3.2 and 2.3.3 of optoacoustic tomography. However, a virtual aperture formed by using focused ultra-wide bandwidth lithium niobate-based detector helps achieving such resolution [30,31,33]. This performance makes optoacoustic mesoscopy perfectly suited for studying small animal models [34] or dermatology applications [35-38].

The imaging speed of RSOM is principally bounded by the repetition rate of the excitation laser, which is inherently limited by the maximum exposure limit [39]. Typical RSOM utilizing fiber bundle system could scan an area of 8 mm $\times 8$ mm within 320 s using laser repetition rate of 500 Hz [38]. Building a single-fiber illumination with through-hole transducer helps increasing the laser repetition rate to 1.4 kHz, making imaging a section of 4 mm $\times 2$ mm possible within a single breath hold [36].

Chapter 3 : Ultrasound Detectors based on Optical Resonators

3.1 Introduction

Ultrasound detection in optoacoustic imaging requires detection characteristics far different from those in traditional ultrasonography. High optoacoustic contrast requires the ultrasound detectors to be highly sensitive because amplitude of the ultrasound signal in optoacoustic typically range from several to hundreds of Pascals – which is orders of magnitude weaker than that in ultrasonography. High spatial resolution requires the ultrasound detectors to be broad band and small in aperture – unless one intends to image superficially using OR optoacoustic microscopy. Unfortunately, conventional piezoelectric transducers have their sensitivity degrade quadratically with detection area. Therefore, it is impossible for piezoelectric elements to have simultaneously small size (few tens of micrometer in diameter) and sufficient sensitivity for optoacoustic detection. Conventional approach to overcome this size-sensitivity trade-off in piezoelectric transducers is to use focused piezoelectric transducers via the synthetic aperture approach. Using this approach, the virtual aperture on the order of few tens of micrometers in diameter was demonstrated with centimeter sized piezoelectric transducers [40,41]. However, this approach results in several disadvantages, such as the incapability of array generalization, performance deterioration outside of the focal plane of the focused piezoelectric transducers and difficulty in achieving optimal optical illumination.

Optical detection of ultrasound is an emerging technology and have shown great potential to replace piezoelectric transducers in certain implementations. In contrast to piezoelectric transducers, optical ultrasound detectors have their sensitivity generally independent of size, thus being promising for applications those necessitate miniaturization such as intravascular and endoscopic imaging. In additional, optical ultrasound detectors offer the ease of integration with the illumination channels and electromagnetic immunity – which has great utility in multimodal imaging with other modalities such as MRI.

Light can be used to detect ultrasound via various mechanisms, namely: refractometric, interferometric and resonance. This thesis focuses on resonator-based on waveguides and integrated optics platforms as the other method showing unclear sensitivity advantage when comparing with other optical techniques.

In this chapter, we first review the basic structures of optical resonators and the underlying principle for optical resonance at each structure. Next, we use the perspective of a good optoacoustic image, i.e., high contrast and high resolution, to trace back into those optical resonators and investigate their expected performance. We also discuss the method to improve both contrast and resolution of an AR optoacoustic image via altering the design and fabrication of the optical resonators.

3.2 Optical Resonator Structures

3.2.1 Fabry-Perot resonators

<u>*a) Fundamental of optical resonators*</u>

Fabry-Perot resonator (FPR) is the most fundamental optical resonator structure and thus is used to study the most basic properties of optical resonators. All the characteristic of an optical resonator can be best understood and derived through FPR.

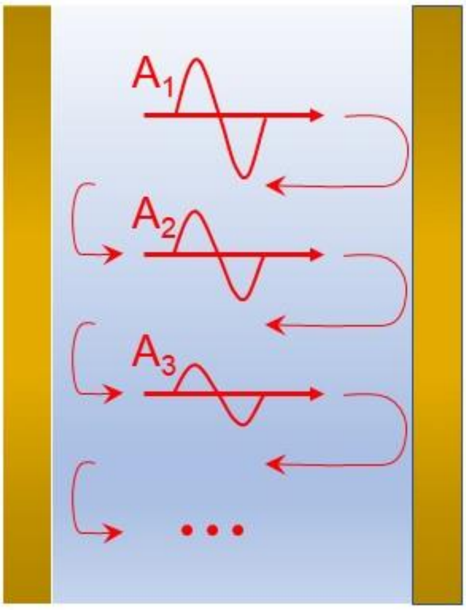

Figure 3.1 - Optical reflection inside a Fabry-Perot resonator (FPR). The FPR is formed by a cavity (light blue colour) sandwiched between tow reflective mirror (gold colour). The red arrow represents the direction of the propagation of the optical plane waves.

A basic FPR comprises of two parallel optical mirrors placing at $z = 0$ and $z = d$ (Figure 3.1). The volume between the two mirrors is filled by a medium with refractive index n. Considering a monochromatic plane wave with complex amplitude A_0 at $z = 0$ travelling to the z direction. The wave is reflected at mirror 2, propagates back to mirror 1 and is again reflected. So, after one "round trip", the amplitude of the wave becomes:

$$A_1 = A_0 \varsigma e^{-i\varphi_{rt}} \tag{3.2.1}$$

where φ_{rt} is the accumulated phase after one round trip and ς is the round-trip loss. Another round-trip results in a wave of complex amplitude A_2:

$$A_2 = A_1 \varsigma e^{-i\varphi_{rt}} \tag{3.2.2}$$

and so on. All of the partial wave $A_0, A_1, A_2, \ldots$ are monochromatic and perpetually coexist. The total wave amplitude A_{total} is therefore the sum of the complex amplitude of all the coexisting waves:

$$A_{total} = A_0 + A_1 + A_2 + \cdots = \frac{A_0}{1 - \varsigma e^{-i\varphi_{rt}}} \tag{3.2.3}$$

The optical intensity inside the resonator is found to be:

$$I_{total} = |A_{total}|^2 = \frac{|A_0|^2}{(1-\varsigma)^2 + 4\varsigma \sin^2(\varphi_{rt}/2)} \tag{3.2.4}$$

Under a special condition called "resonant condition", the accumulated phase after a single round trip φ_{rt} is an integer multiply of 2π, all of the partial wave interfere constructively. I_{total} then reaches its maximum value of:

$$I_{max} = \frac{|A_0|^2}{(1-\varsigma)^2} \tag{3.2.5}$$

The resonant condition can be formulated as:

$$\varphi_{rt} = k_0 n 2d = m2\pi \tag{3.2.6}$$

where $k_0 = 2\pi/\lambda_0$ is the wavenumber of the optical monochromatic wave in vacuum, λ_0 is the vacuum wavelength, m is an arbitrary positive integer. The optical frequency that satisfies the resonant condition is called "resonant frequency" and can be derived from equation 3.2.6 as:

$$f_m = m\frac{c}{2nd} \tag{3.2.7}$$

where $n = 299792458\,\mathrm{m}/s$ is the speed of light in vacuum. Two adjacent resonant frequencies are separated by a constant frequency different named free spectral range of the resonator:

$$f_{FSR} = \frac{c}{2nd} \tag{3.2.8}$$

To characterize the spectral response of the FPE, Equation 3.2.5 is often rewritten as:

$$I_{total} = \frac{I_{max}}{1 + \left(\frac{2\mathcal{F}}{\pi}\right)^2 \sin^2(\pi f / f_{FSR})} \tag{3.2.9}$$

where $\mathcal{F} = (\pi\sqrt{\varsigma})/(1 - \varsigma)$ is a parameter known as the finesse of the resonator and represents the ability of a resonator to keep light circulating inside itself. The relationship between I_{total} and optical frequency is plotted in Figure 3.2. When the round-trip loss is small ($\varsigma \to 1$), the finesse $\mathcal{F}$ is large and the full-width half maximum (FWHM) of the resonance peak can be approximated as:

$$\delta f = \frac{f_{FSR}}{\mathcal{F}} \tag{3.2.10}$$

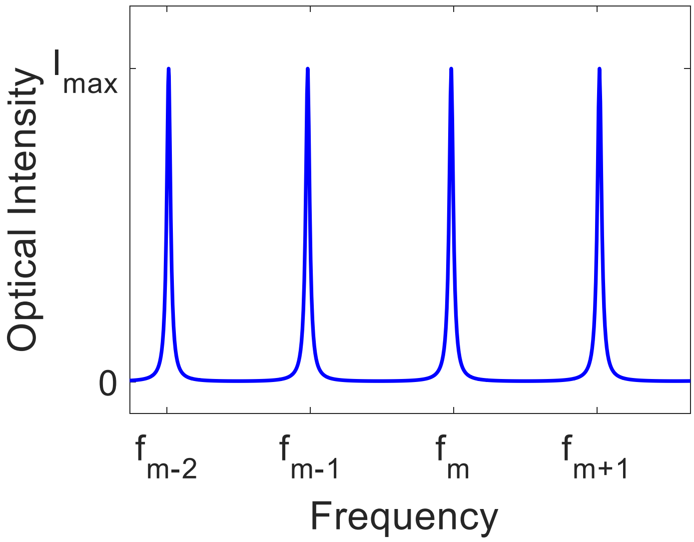

Figure 3.2 - Spectrum of an optical resonator. The resonator is capable of storage optical energy at some specific frequencies called resonant frequencies.

In practical situation, the optical confinement ability of the resonator is normally characterized by a parameter named quality factor Q, which is defined as the ratio between the stored energy and the energy loss per optical cycle. Q can be easily obtained by measuring the spectral response of a resonator and is related to the finesse by [42]:

$$Q = \frac{f_0}{\delta f} = \frac{f_0}{f_{FSR}}\mathcal{F} \tag{3.2.11}$$

Q of conventional optical resonators can have value varying greatly from few hundred to several billions.

b) Realization of Fabry-Perot Resonator

FPR can be realized as a slabs on a transparent plate [43] or on the tip of an optical fiber [44]/ fiber bundle [45]. Fabrication of FPR normally involves three steps corresponding to the making of three components. First, the first reflective mirror is formed, subsequently followed by formation of the cavity layer. Finally, the second mirror is created on top of the cavity layer.

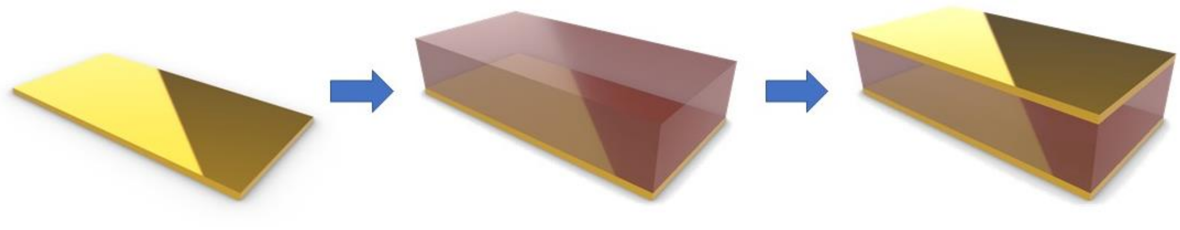

Figure 3.3 - Fabrication of a FPR. The first reflective mirror is formed on top of a substrate, followed by adding the cavity layer and finished by applying the second reflective mirror.

3.2.2 Phase-shifted Bragg grating

Strictly speaking, phase-shifted Bragg grating (pBG) is a special type of FPR. However, instead of using highly reflective mirror coating as in FPR, pBG use a reflective mechanism called "distributed reflector" using Bragg gratings. A Bragg grating is a structure with periodic modulation of effective refractive index n_{eff} in the propagation direction of an optical mode. This modulation is normally induced by varying the refractive index or the physical dimension of the waveguide (Figure 3.3). A Bragg grating can be fully identified by the type of grating, the "DC" index change $\overline{\delta n_{eff}}$, the "AC" index change δn_{eff}, the grating period Λ, and the total grating length L. Within this thesis, only uniform Bragg grating in single-mode waveguides is considered.

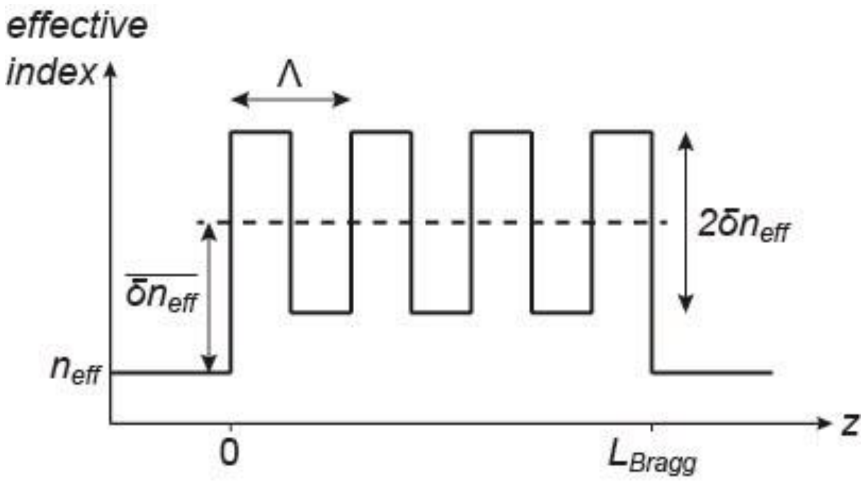

Figure 3.4 - The profile of the waveguide's effectove index of a grating along its propagation direction. The effective index is modulated with amplitude of $\boldsymbol{\delta n_{eff}}$ (also called "AC index modulation") and period $\boldsymbol{\Lambda}$. The grating section has length $\boldsymbol{L_{Bragg}}$ and average effective index of $\boldsymbol{n_{eff}} + \overline{\boldsymbol{\delta n_{eff}}}$, with $\boldsymbol{n_{eff}}$ is the effective index of the non-grating section and $\overline{\boldsymbol{\delta n_{eff}}}$ is the offset from the non-grating index (also called "DC index modulation").

Due to the minor refractive index different at each boundary, light is reflected partially. All the reflected signals interfere constructively only in a narrow band around one particular wavelength, namely the Bragg wavelength and is given by:

$$\lambda_{Bragg} = 2n_{eff}\Lambda \tag{3.2.12}$$

To quantitatively understand how Bragg grating reflects light, it is the best to use the coupled-mode theory approach [46]. In this approximation, the transverse component of the electrical field of the fundamental mode can be written as the superposition of two counter-propagating waves:

$$\boldsymbol{E_t}(\boldsymbol{r}, t) = \left[A(z)e^{i\beta z} + B(z)e^{-i\beta z}\right]\boldsymbol{E}(x, y)e^{-i\omega t} \tag{3.2.13}$$

where $\beta = (2\pi/\lambda_0)n_{eff}$ is the propagation constant of the fundamental mode, λ_0 is the vacuum wavelength. $A(z)$ and $B(z)$ are the slowly varying amplitude of the mode travelling in $+z$ and $-z$ directions, and $\boldsymbol{E}(x, y)$ describes the transverse profile of the mode. By defining a z-independent detuning parameter δ which is given as:

$$\delta = \beta - \beta_{Bragg} = 2\pi n_{eff}\left(\frac{1}{\lambda_0} - \frac{1}{\lambda_{Bragg}}\right) \tag{3.2.14}$$

the coupled-mode equation for the two counter-propagating modes can be simplified to have the form [Fiber Grating Spectra, 1997]:

$$\frac{dR}{dz} = i\hat{\sigma}R(z) + i\kappa S(z) \tag{3.2.15}$$

$$\frac{dS}{dz} = -i\hat{\sigma}S(z) + i\kappa^* R(z) \tag{3.2.16}$$

where the amplitudes R and S are $R(z) = A(z)e^{i\delta z}$ and $S(z) = B(z)e^{-i\delta z}$. In Equation 3.2.15 and Equation 3.2.16, κ is the "AC" coupling coefficient and $\hat{\sigma}$ is the "DC" self-coupling coefficient:

$$\kappa = \kappa^* = \frac{\pi}{\lambda}\delta n_{eff} \tag{3.2.17}$$

$$\hat{\sigma} = \delta + \frac{2\pi}{\lambda}\overline{\delta n_{eff}} \tag{3.2.18}$$

By applying the boundary conditions $R(z = 0) = 1$ and $S(z = L) = 0$, which means a forward-going interrogation wave incident from $z = -\infty$, the reflection coefficient r and reflectivity R can be shown to be [46]:

$$r = \frac{S(z = 0)}{R(z = 0)} = \frac{-\kappa \sinh\left(\sqrt{\kappa^2 - \hat{\sigma}^2}L\right)}{\hat{\sigma}\sinh\left(\sqrt{\kappa^2 - \hat{\sigma}^2}L\right) + i\sqrt{\kappa^2 - \hat{\sigma}^2}\cosh\left(\sqrt{\kappa^2 - \hat{\sigma}^2}L\right)} \tag{3.2.19}$$

$$R = |r|^2 = \frac{\sinh^2\left(\sqrt{\kappa^2 - \hat{\sigma}^2}L\right)}{\cosh^2\left(\sqrt{\kappa^2 - \hat{\sigma}^2}L\right) - \frac{\hat{\sigma}^2}{\kappa^2}} \tag{3.2.20}$$

The relationship between R and optical frequency of Bragg gratings with varying grating parameters are plotted in Figure 3.5. One of the most important properties of a Bragg grating is its maximum reflectivity, which then can be derived from Equation 3.2.20 as:

$$R_{max} = \tanh^2(\kappa L) \tag{3.2.21}$$

and it occurs at the wavelength:

$$\lambda_{max} = \left(1 + \frac{\overline{\delta n_{eff}}}{n_{eff}}\right) \lambda_{Bragg} \tag{3.2.22}$$

From Equation 3.2.21, it can be seen that increasing either the strength or length of the grating help improving the reflectivity of the Bragg mirror. However, as $\kappa L > 3$, the grating enters the "strong grating regime" [47]. Here light does not penetrate the full length of the grating, thus the reflectivity is almost independent of grating length.

Another important characteristic of the Bragg grating is the band gap, which is the frequency band that the Bragg grating is reflective. The band gap of the Bragg grating is commonly defined as the spacing between two band-edges – the point where $|\hat{\sigma}| < \kappa$. Inside the band gap, the wave amplitude R and S grow and decay exponentially along z direction; outside the band gap, those amplitude evolve sinusoidally. The reflectivity at the band edge is [46]

$$R_{band\ edge} = \frac{(\kappa L)^2}{1 + (\kappa L)^2} \tag{3.2.23}$$

and the band edges occur at

$$\lambda_{band\ edge} = \lambda_{max} \pm \frac{\delta n_{eff}}{2 n_{eff}} \lambda_{Bragg} \tag{3.2.24}$$

To form an optical resonator, two Bragg grating should be place next to each other in the same waveguide and be separated by a cavity. The length of this cavity must be precisely design so that at least one of its resonant frequencies (Equation 3.2.7) falls into the band gap of the Bragg grating. The smallest cavity length that supports the optical resonant effect corresponds to a phase shift of π for the Bragg wavelength. This structure is referred as "pi-shifted Bragg grating" (pBG). The reflection coefficient of a pBG can also be analyzed using coupled mode theory to have the final form [47]:

$$r = \frac{\hat{\sigma}}{\kappa} \frac{1}{\left({}^{\gamma}/_{\kappa \tanh\left(\gamma L_{Bragg}/2\right)} - {}^{i\hat{\sigma}}/_{2\kappa}\right)^2 - 1} \tag{3.2.25}$$

where

$$\gamma = \sqrt{\kappa^2 - \left({}^{\delta}/_{2}\right)^2} \tag{3.2.26}$$

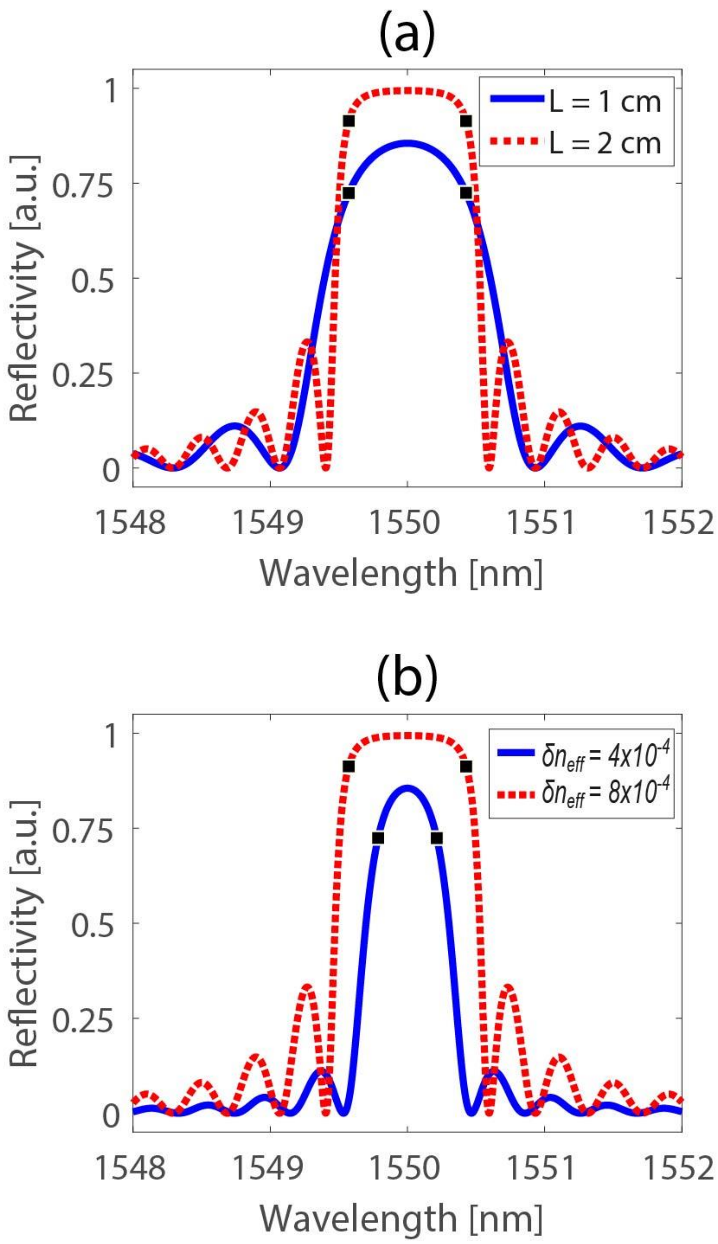

Figure 3.5 - Reflection spectrum of Bragg gratings with different grating parameters. (a) Two gratings with $\boldsymbol{\delta n_{eff} = 8 \times 10^{-4}}$ and different grating length $\boldsymbol{L = 1}$ **mm** (blue, solid curve) and $\boldsymbol{L = 2}$ **mm** (red, dashed curve). (b) Two gratings with equal length $\boldsymbol{L = 2}$ **mm** but different AC index modulation $\boldsymbol{\delta n_{eff} = 4 \times 10^{-4}}$ (blue, solid curve) and $\boldsymbol{\delta n_{eff} = 8 \times 10^{-4}}$ (red, dashed curve). In both figures, the DC index modulation $\boldsymbol{\overline{\delta n_{eff}} = 0}$. The position of the band edges is marked with the black squares.

The reflection spectrum of two pBGs with the same total length of $L = 3$ mm but different AC index modulation of $\delta n_{eff} = 5 \times 10^{-4}$ and $\delta n_{eff} = 7 \times 10^{-4}$ are plotted in Figure 3.6. The present of the optical confinement capability is indicated by a resonant dip appearing at the center of the band gap. As can be easily predicted, the stronger grating results in a resonator with higher Q-factor and smaller FWHM of the resonant dip.

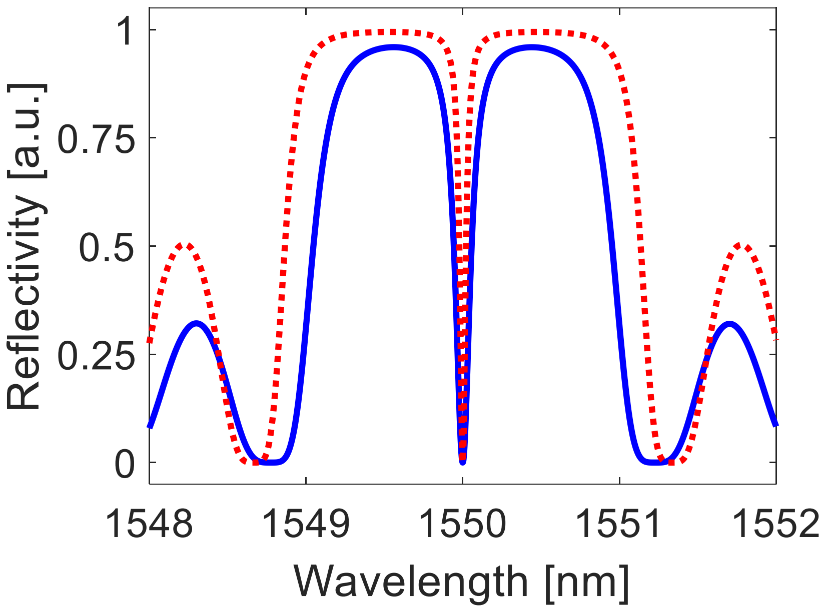

Figure 3.6 - Spectrum of two pBGs with different AC index modulations: $\boldsymbol{\delta n_{eff}} = \mathbf{5} \times \mathbf{10^{-4}}$ (blue, solid curve) and $\boldsymbol{\delta n_{eff}} = \mathbf{7} \times \mathbf{10^{-4}}$ (red, dashed curve).

Because of the distributive nature of the Bragg reflector, optical energy inside a pBG is not tightly confined inside the cavity but spreads into the two Bragg mirror with exponentially decaying properties. A more detail analysis of this structure will be given in Chapter 4.

Bragg grating is one of the most fundamental optical structures and has many applications ranging from optical filtering, multiplexing to sensing. In optical fiber, because fibers have fixed core/ cladding dimension, the index modulation must be induced by periodically changing the refractive index of the core to create Fiber Bragg Gratings (FBGs). The core of silica optical fibers is doped with additional elements to increase the refractive index. Fortunately, a wide range of such doping (for example: germanium [48], europium [49], cerium [50,51], erbium/ germanium [52], germanium/ boron [53]) makes the core itself photosensitive, which means UV exposure of the optical fiber results in a permanent change of the core refractive index. In the case where the intrinsic photosensitive of the core is too small, this effect can be enhanced by hydrogen loading [54], flame brushing [55] or boron co-doping [53]. The periodic pattern is carefully inscribed using special technique such as interferometric [48], phase mask [56,57] or point-by-point [49]. Ultrashort-pulse laser has increasingly used to inscribe fiber Bragg grating (FBG) lately as this technique can be applied for a wide range of optical fiber independently of the core doping [58].

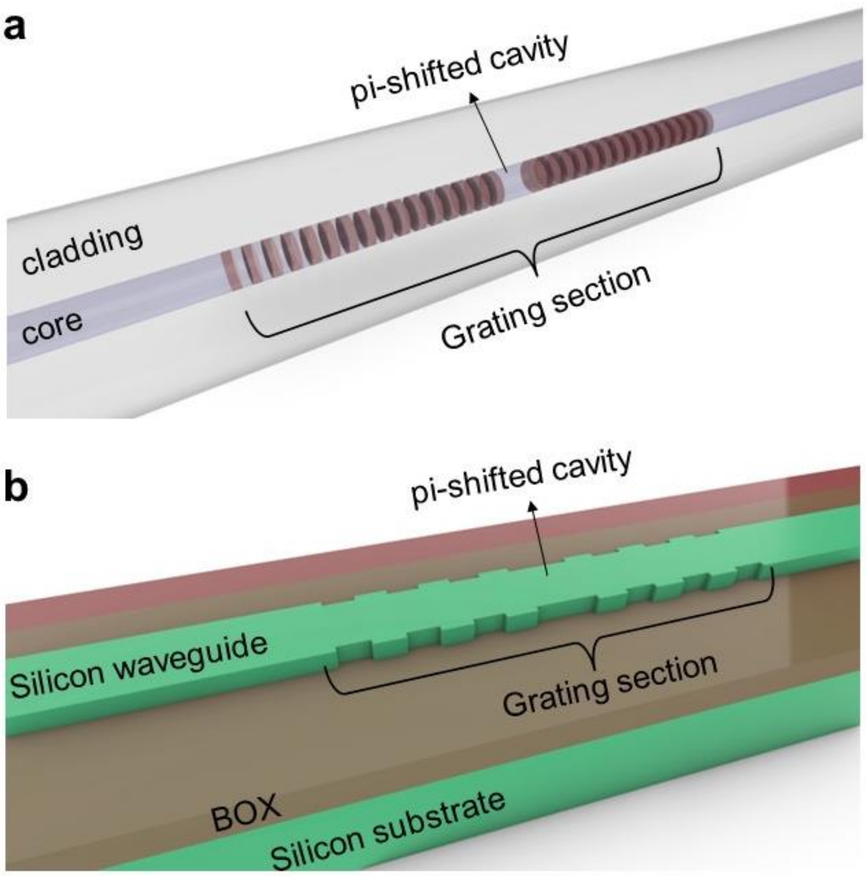

Figure 3.7 - pBG structures in different platforms. (a) pi-shifted Fiber Bragg Grating (pFBG) in optical fiber. (b) pi-shifted Waveguide Bragg Grating (pWBG) in Silicon-on-Insulator platform. BOX stands for "buried oxide".

In chip-based optical waveguides such as silicon waveguide [59,60], silicon nitride waveguide [61,62], polymer waveguides [63,64], the Waveguide Bragg Grating (WBG) is created by introducing additional corrugation to the side wall through lithographic or etching. As the effect of physical corrugation to the effective index is much stronger than photosensitive-based effect, the grating strength in chip-based waveguides in general could be several orders of magnitude stronger than in optical fiber [65,66].

3.2.3 Whispering gallery mode resonators

Whispering gallery mode (WGM) resonators are named after the acoustical whispering gallery effect that was first explained by Lord Rayleigh in St. Paul's Cathedral [67,68]. WGM resonators do not rely on special reflective coating to confine light. From the ray optics perspective, light is trapped inside a WGM resonator purely by total internal reflection at the circular-shaped outer cavity interface (Figure 3.8). WGMs are commonly imagined as closed-trajectory rays that experiences multiple total internal reflections and being reflected back to its original position.

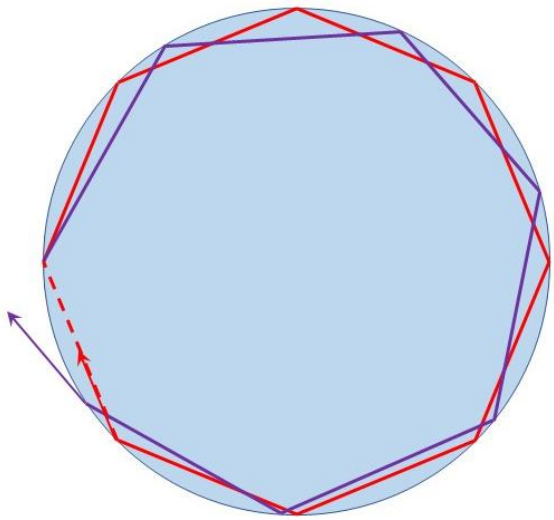

Figure 3.8 - Whispering gallery mode resonator from the perspective of ray optics. The red ray corresponds to a whispering gallery mode, while the purple ray is not and is scattered out of the resonator.

A more accurate inside into the optical distribution inside the WGM resonator can be provided by solving Maxwell's equation in the spherical and cylindrical coordinates. Such derivations can be found in detail from other literatures [69]. To quickly summarize the results, the electrical field in the θ direction (the direction of the propagation vector $\boldsymbol{k}$) can be separated into the contributions in each dimension:

$$\boldsymbol{E}_{\theta} = \psi_r(\boldsymbol{r})\psi_{\theta}(\boldsymbol{\theta})\psi_{\phi}(\boldsymbol{\phi}) \tag{3.2.27}$$

The radial component $\psi_r(\boldsymbol{r})$ varies with radius $\boldsymbol{r}$ according to:

$$\psi_r(\boldsymbol{r}) = \begin{cases} AJ_l(\boldsymbol{k}\cdot\boldsymbol{r}) & r < R \ (inside\ the\ resonator) \\ Be^{-\alpha(\boldsymbol{r}-\boldsymbol{R})} & r \geq R \ (outside\ the\ resonator) \end{cases} \tag{3.2.28}$$

where $J_l(\boldsymbol{k}\cdot\boldsymbol{r})$ is the Bessel function of the first kind with order l, α is the evanescent field decay rate, A and B are amplitude coefficient to satisfy the boundary conditions. WGMs are referred to the modes with very large order $l \gg 1$, so that the majority of the optical energy locates near the outer surface of the resonator (Figure 3.9).

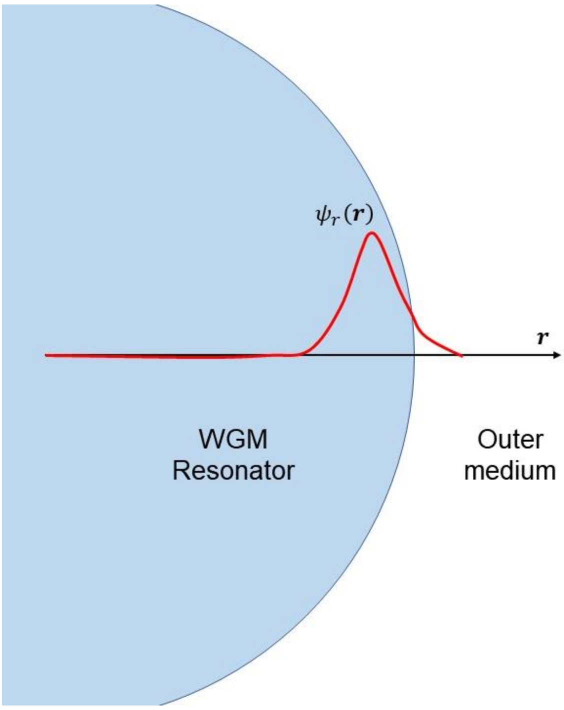

Figure 3.9 - Profile of the radial component of a high-order whispering gallery mode. The optical intensity is almost zero inside the resonator, except near the physical boundary of the resonator.

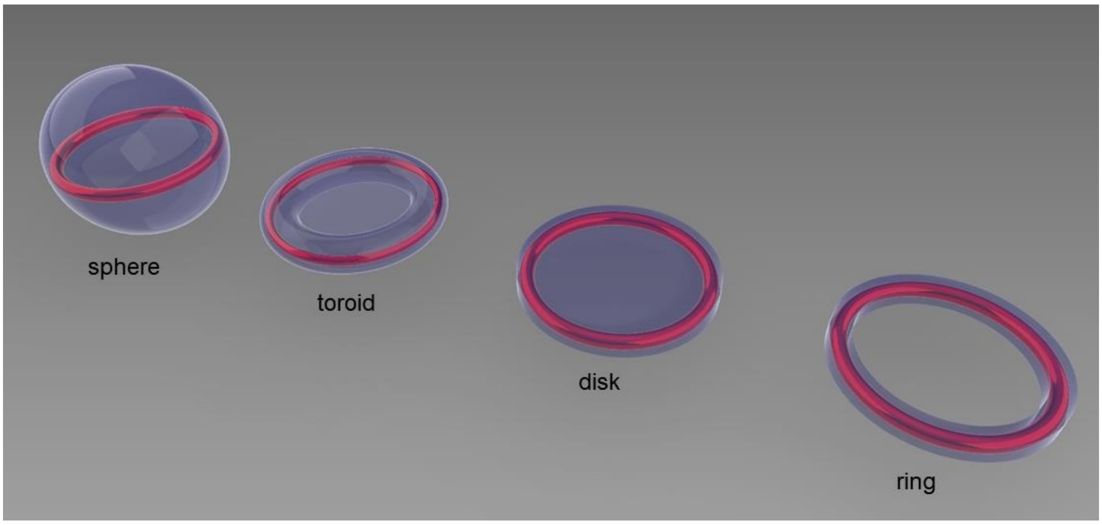

Figure 3.10 - Geometries of whispering gallery mode resonators. The transparent purple part represents the physical body of the resonator. The red ring inside the physical body of the resonator represents the optical intensity of the confined whispering gallery modes.

One important feature of WGM resonator that makes it different from other types of optical resonator is that optical coupling into WGM resonator must be conducted evanescently. WGM resonators could have various geometries including sphere [70-72], bottle [73-75], bubble [76,77], toroid [78,79], disk [80,81], ring [82,83]. These structures are made free-standing, in optical fiber or integrated into a photonics chip. The material for constructing WGM resonators also varies greatly, covering both organic (polymer) and inorganic (silica, silicon, etc.) materials.

Directly coupling with WGM resonator produces negligible efficiency as majority of the optical energy is scattered out according to Lorentz-Mie scattering theory [84]. Evanescent coupling to WGM resonator therefore introduces additional components onto the resonator structure itself and will be a matter of consideration in the context of sensor utility and performance. Typical components for WGM coupling are bus waveguide [85,86], tapered fiber [87,88], side-polished fiber [89], angle-polished fiber [90] and prism [72,91].

3.2.4 Photonic crystal resonators

Photonic crystals (PhCs) are periodical structures that utilize the photonic band-gap effect to manipulate the propagation of light and confine light into small volumes [92]. This optical confinement via the photonic bandgap effect can be performed in 1D or 2D. 3D PhC resonator is theoretically possible and has been demonstrated, but the technical challenge makes it generally unsuitable for optoacoustic imaging and will not be discussed. 1D PhC is created by periodically altering the refractive index of a waveguide. The Bragg grating discussed in Section 3.2.2 can be considered as sub-category of 1D PhC and the behavior of light in 1D PhC resonator is very similar to the pi-shifted Bragg grating. In this section, the most important PhC class to be discussed is the PhC slab – a 2D periodical index contrast introduced into a thin high-index guiding layer (Figure 3.11b, c).

Without any lattice defect (Figure 3.11b), the PhC slab supports a quasi-guided modes called “guided mode resonances”. When being under out-of-plane illumination, the grating-like property of the periodic modulation diffracts a portion of optical energy into guided modes of the slab waveguide. However, as they propagate, the energy continuously leaks out of the waveguide due to the periodic pattern. At a certain resonant wavelength, the de-coupled light interferes constructively with the illumination and the reflected light, resulting in a resonator effect [93]. The detail analysis of the guided mode resonant can be found elsewhere [94].

Additionally, light can be efficiently confined in a sub-micrometer space by introducing a point defect in the periodical pattern [95] (Figure 3.11c).

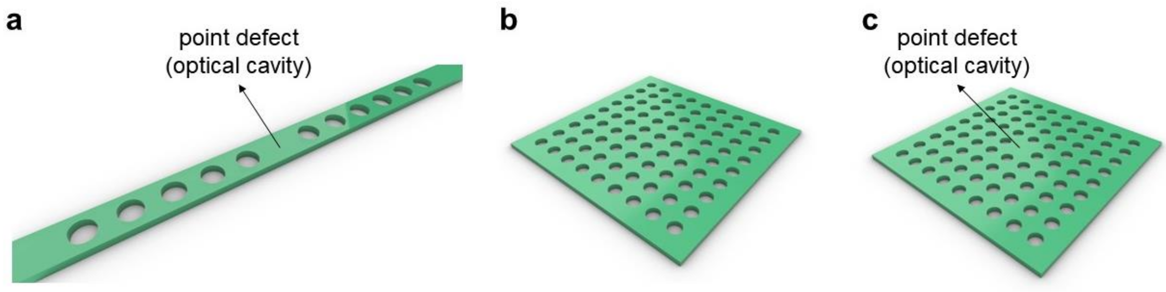

Figure 3.11 - Photonics crystal (PhC) resonators. (a) 1D resonator formed by having a point defect on a 1D PhC waveguide. (b) 2D PhC slab with no defect supports "guided mode resonance". (c) 2D PhC slab with point defect to confine light at the defect.

PhC slabs are usually fabricated by using electron beam lithography on a thin layer made from high index materials such as silicon [96] or silicon nitride [97].

3.3 Sensitivity of Optical Resonator-based Ultrasound Detectors

3.3.1 General theory

The resonant frequency of an optical resonator is strictly determined by the physical dimension and the effective index of the optical cavity. Any perturbation to those parameters results in a change of resonant frequency. This resonant shifting effect can simply be read-out using a tunable laser where the emission wavelength is locked at the position of maximum slope within the resonant dip. By measuring the intensity of either the reflected or transmitted signal from the resonator with a photodetector, the resonant shift could be quantified. This is the underlying physics that governs the sensing mechanism of optical resonators with various parameter of interest such as temperature [44], stress [98], chemical and biological substances [99], etc.

To quantify the sensitivity of an ultrasound sensor, it is convenient to define the detection sensitivity S

$$S = \frac{dI}{dP_0} \left[\frac{V}{Pa}\right] \tag{3.3.1}$$

where P_0 is the incident ultrasonic pressure in [Pa] and I is the read-out signal [V]. The read-out signal can be obtained by measuring either the reflected or transmitted optical intensities from the optical resonator via a photodetector with large trans-impedance gain, so it often has the unit of voltage.

Because sensitivity can be easily increased with electrical amplifier, it is therefore necessary to define a universal parameter named noise-equivalent pressure (NEP)

$$NEP = \frac{noise_{rms}}{S}\ [Pa] \tag{3.3.2}$$

where $noise_{rms}$ is the root-mean-square of the system noise in [V]. NEP has the physical meaning of the smallest possible ultrasonic pressure that can be detected, or equivalently the ultrasonic pressure that gives signal-to-noise ratio of 1. The smaller the noise-equivalent pressure, the better the detection system is. Amplification of the read out signal with electrical amplifiers cannot improve noise-equivalent pressure since the noise level will be amplified by at least an equal amount.

Because of the broad-band nature of the optoacoustic signals, the detector should be able to capture ultrasound signal over a large bandwidth. Therefore, it is important to define a bandwidth-normalized sensitivity parameter named noise-equivalent pressure density (NEPD):

$$NEPD = \frac{NEP}{\sqrt{BW}}\ [Pa/\sqrt{Hz}] \tag{3.3.3}$$

There are several methods to help decreasing the noise level of an optical detector, i.e., pulse interrogation [100], balanced-detection [101,102], phase read-out [103]. Within the scope of this thesis, we only focused in improving the intrinsic NEP of the optical detectors by increasing S.

For optical-resonator-based ultrasound sensor, the sensitivity S can be decomposed into two terms

$$S = \frac{dI}{dP_0} = \frac{dI}{d\lambda_r} \times \frac{d\lambda_r}{dn_{eff}} \times \frac{dn_{eff}}{dP_0} = O \times L \times A \tag{3.3.4}$$

where λ_r is the resonant frequency of the optical resonator, and P_0 is the incident ultrasonic pressure. The O term in the right side of Equation 3.3.4 is called "optical sensitivity" [V/nm], representing how a certain shift in resonant frequency induces a change in the optical readout signal. The A term has the unit of [Pa^{-1}], illustrates how strong a given ultrasonic pressure shifts the effective refractive index of the optical resonators. This term generally depends on the acoustical properties of the resonator, so it has the name "acoustical sensitivity". A more detailed consideration on how these two terms are used to create ultrasound sensor with high detection sensitivity will be given in the next sections.

The remaining term L illustrates how a small change in the cavity's effective index perturbing the resonant frequency. Using the resonant condition of the optical resonator, this term can be rewritten as:

$$L = \frac{d\lambda_r}{dn_{eff}} = \frac{L_{rt}}{m} = \frac{\lambda_r}{n_{eff}} \tag{3.3.5}$$

where L_{rt} is the optical round-trip length of the resonator. It can be seen from Equation 3.3.5 that with the same mode number m, a larger optical resonator gives higher sensitivity. Also, a larger resonant wavelength or lower cavity index also help improving the sensitivity.

3.3.2 Optical sensitivity

a) General considerations

The optical sensitivity represents how well a small shift in resonant frequency alters the optical read-out signal. Intuitively, the optical sensitivity depends directly on the slope of the resonant dip, which is subsequently dependent on the interrogation laser power, the trans-impedance gain of the photodetector and optical Q-factor of the resonator.

$$O = R \times G \times Q \tag{3.3.6}$$

R is the intensity of the read-out optical signals, proportional to interrogation power (in W), G is the photodetector gain (V/W) and Q is the Q-factor. The first two parameters R and G depend on the interrogation system and are not intrinsic properties of the optical detector, so only the optical Q-factor is under consideration in this thesis. However, both R and G set some physical limitations for proper consideration toward the choice of optical detectors. As mentioned above, R is proportional to the optical interrogation power, which normally depends on the output power of the tunable laser used to interrogate the optical detector. Conventional tunable lasers are capable of provide maximum output power of approximately 10 dBm (or 10 mW), which is sufficient to interrogate most optical detector due to the limitation called optical power handling capacity. Optical polymers generally have low optical power handling capacity because majority of the optical absorption will be converted to heat, which then significantly reduces the thermal stability of the polymer-based resonators due to the large thermos expansion coefficient of polymers [104]. Silicon also has low optical power handling capacity because of the low threshold for nonlinear effects [105]. Such effects distort the shape of the resonant dip and make the detector characteristics become unpredictable. The interrogation power for polymer or silicon resonators in OA imaging is often around 3-4 mW. On the other hand, silica or glass has extremely high optical power handling capacity. Silica resonators were demonstrated to operate stably with interrogation power on the order of tens of mW [106]. The photodetector gain G is determined by the transimpedance amplifier of the photodetector. State-of-the-art photodetector could have G as high as 2×10^6.

With the interrogation system is set aside, the Q-factor is the only intrinsic property of an optical resonator that governs its optical sensitivity.

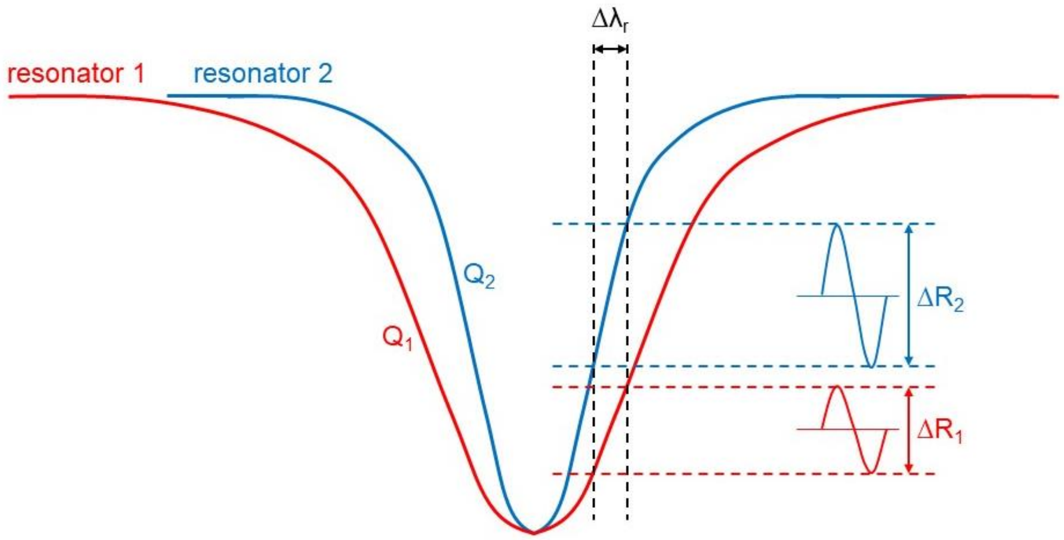

Figure 3.12 - Dependence of the optical sensitivity onto Q-factor of the resonator. Resonator 1 (red curve) has lower Q-factor compared to resonator 2 (blue curve): $\boldsymbol{Q_1 < Q_2}$, resulting in a less steep change in the resonant dip. The same shift in resonant frequency $\boldsymbol{\Delta\lambda_r}$ induces a smaller change in the reflected intensity from resonator 1 compared to resonator 2, thus resulting in a smaller read-out signal and lower sensitivity.

To achieve higher Q-factor, the round-trip loss should be minimized. There are many sources of optical loss in an optical resonator, but they can be categorized into three main types: scattering loss, absorption loss and coupling loss.

$$\frac{1}{Q_{total}} = \frac{1}{Q_{scat}} + \frac{1}{Q_{abso}} + \frac{1}{Q_{coup}} \tag{3.3.7}$$

The scattering depicts the optical loss due to light being scattered out of the resonator. It could be induced by a mirror with non-unity reflectivity in Fabry-Perot design, a Bragg grating with reflectivity of less than 1, or the bending loss in WGM resonator that cause the total-internal reflection mechanism to be non-perfect. The non-homogeneous of the cavity internal and surficial structures also plays an important role in the scattering loss.

Absorption loss represents the photon being absorbed by the cavity material. Therefore, it is important to choose the right material or platform to construct optical detectors. Silica – a common optical material – permits light over a large wavelength range with small absorption, but silica is the most transparent at telecommunication wavelengths (1300-1600nm). Materials that are used for device construction in photonics integrated circuits (PIC) are generally highly transparent at telecommunication wavelength but absorb light strongly at visible range. A lot of polymers, on the other hand, are transparent at visible wavelengths but absorb near-infrared radiation. Absorption loss usually sets the fundamental limits for Q-factor of an optical resonator as it cannot be surpassed.

Coupling loss arises from the action of sending light into the resonator and read-out the optical signal. Normally, in optical resonators that utilize evanescent coupling, not always one hundred percent of the interrogation power could be fed to the resonator, leading to a decrement of optical energy circulated inside the resonator.

From the practical point of view, ultrahigh Q-factor is also not desirable. In contrast to quantum measurement or cryogenic application, biomedical environments often have high temperature gradient and vibrations induced by biological processes. These environmental effects perturb the optical resonator, resulting in a typical resonant fluctuation up to a few picometers. A resonant linewidth that is smaller than this environmental shift causes the sensor to be completely off resonant, losing the detection capability during operation. For optoacoustic imaging in general, the maximum optical Q-factor should be on the order of 10^6 or less to not make the sensor impractical in clinical applications.

In additional, optical resonators can have large dimensions up to millimeter-scale to exploit advantages that cannot be achievable with miniaturized sensors (i.e.: negligible bending loss [80], use of coherent laser for interrogation [107]). Such resonators could achieve high sensitivity but are going to smear the lateral resolution to the scale of its physical dimensions as will be described in Section 3.4. Therefore, those large resonators are off interest of this thesis. The focus here is optical resonators which have sub-millimeter dimensions.

b) Fabry-Perot resonators

Scattering loss due to low mirror reflection is one of the main sources of optical loss in FPR. The two reflective mirrors were originally made of highly reflective metals such as gold [44] or silver [108] as these materials can easily be deposited on quartz plates or fiber tip using sputtering or chemical-based methods. However, dielectric mirrors are rapidly replacing metallic mirrors as they provide higher reflectivity and a transparent spectrum window for through-sensor illumination [109].

Except for mirror loss, there is a special source of scattering loss in FPR named lateral beam walk-off. Because of the lack of a wave-guiding mechanism inside the FPR, the optical beam exiting a waveguide or being focused onto the sensor is subsequently diverged and the energy is dispersed eventually with increasing number of round trips. Using a highly collimated laser for interrogation could help solving the beam walk-off but is not of interest as the structure cannot be miniaturized [107]. Additional waveguide can be fabricated inside the FPR using polymer with slightly higher refractive index [110], or the second mirror can be shaped into concaved shape to re-converge the diverging beam [111].

c) Phase-shifted Bragg grating

For phase-shifted Bragg Grating, a higher optical Q-factor generally requires higher reflectivity from the grating. This can be done by either increasing the grating length or the grating strength.

In both optical fiber and PIC, improving the grating strength is not always technically possible and some certain AC index modulation limits exist.

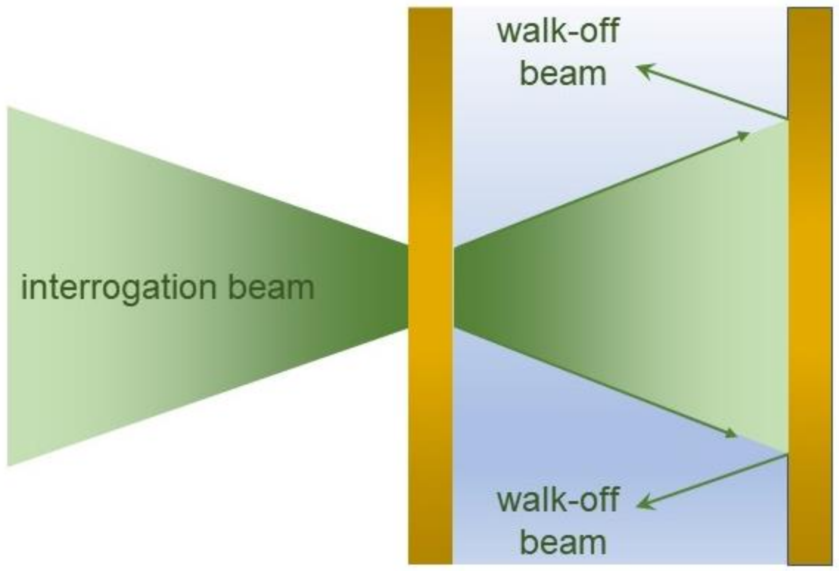

Figure 3.13 - Lateral beam walk-off in planar FPR. The interrogation beam in focused onto the surface of the fist mirror, leading to beam divergence once entering the cavity.

For optical fiber, the typical AC index modulation is on the order of 10^{-3}. Optical Q-factor of 10^6 were frequently reported for phase-shifted FBG [112] [101]as the total grating length reaches almost 1 centimeter. Higher Q-factor on the order of 10^7 is possible with longer grating length [66,113,114] but generally not desirable as being explained in section a.

In PIC, the propagation loss is several orders of magnitude higher than optical fiber, thus the maximum achievable Q is reduced. For silicon strip waveguides, the propagation loss is typically around 2 dB/cm [115] in comparison with approximately 0.5 dB/km of optical fiber. However, the AC index modulation in PIC is an order of magnitude stronger than in fiber due to physically altering the waveguide geometry, enabling the grating length to be shorter (sub millimeter). Very strong grating on low loss silicon strip waveguide was reported to have Q-factor that reach almost 2×10^5 [65].

d) Whispering gallery mode resonators

Microrings and microdisks are two special geometries of WGM resonators because their surface boundary is normally formed by lithography with little control in the sidewall roughness. Scattering loss due to this surface roughness then dominants all other loss mechanisms. Numerous works have been conducted to improve the Q-factor of microrings and microdisks by smoothening the side wall [11,116].

Other geometries such as microtoroids, microspheres and microbottles overcome the side wall roughness by introducing an additional thermal reflow process [78,117]. Therefore, these geometries could offer ultra-high Q-factor of > 10^7 and are often the class of optical resonators that supports the highest Q-factor.

In addition to the side wall scattering, bending loss always exists in WGM resonators due to the curvature shape, making WGM resonators inherently leaky. The larger the circumference of the mode distribution is, the smaller the bending loss. WGM resonators can be fabricated with diameter up to millimeter scale, achieving Q-factor as large as several billion [80]. However, as will be proven in the next section, such large dimension significantly degrades the imaging resolutions and makes the imaging system bulky. Typically, in optoacoustic imaging, WGM resonators with diameter on the order of tens of micron are the conventional choices because of the balance between Q-factor and miniaturization.

Due to special requirement of evanescently coupling light into the resonator, the coupling loss is a major concern in WGM resonators. Almost unity efficiency coupling was achieved with tapered fiber for silica-based resonator [87]. Prism coupling [91], side-polished fiber coupling [89] or angle-polished fiber coupling [90] have also been studied, but they give less coupling efficiency than tapered fiber. However, all of these solutions require high-precision alignment and significantly reduce the robustness of the detector that should operate in biomedical environments. These bulky coupling challenge eliminates almost totally the dissemination of ultrahigh-Q-geometries like microspheres and microbottles in biomedical imaging. In fact, only a couple of works characterized microsphere and microbottle resonators for ultrasound sensing but could not deliver real biomedical applications [117-119]. WGM resonators that could be integrated on chip such as microrings then become the most viable choice since monolithic coupling is possible using on-chip bus waveguide [120,121].

e) Photonic crystals resonators

PhC resonators using defected lattice point was demonstrated, but had generally low Q-factor [122]. A break-through in PhC resonators was published in 2003, wherein scientists realized that to confine light in a PhC crystal strongly, they have to confine light "gently" [95]. This idea was experimentally proved by slowly altering the PhC lattice constant toward the cavity defect. Later, this concept was further developed into more advance structure such as heterogeneous PhC lattice [123]. Q-factor that reaches 10^6 was reported frequently by carefully designing the PhC lattice [124]. However, up to the author's knowledge by the time of writing this thesis, PhC resonator based on lattice defect has not been demonstrated for ultrasound sensing applications.

PCR based on guided mode resonant has recently been explore for ultrasound detection applications. However, Q-factor of this type of resonator is generally not very high, on the order of 10^3 [125,126].

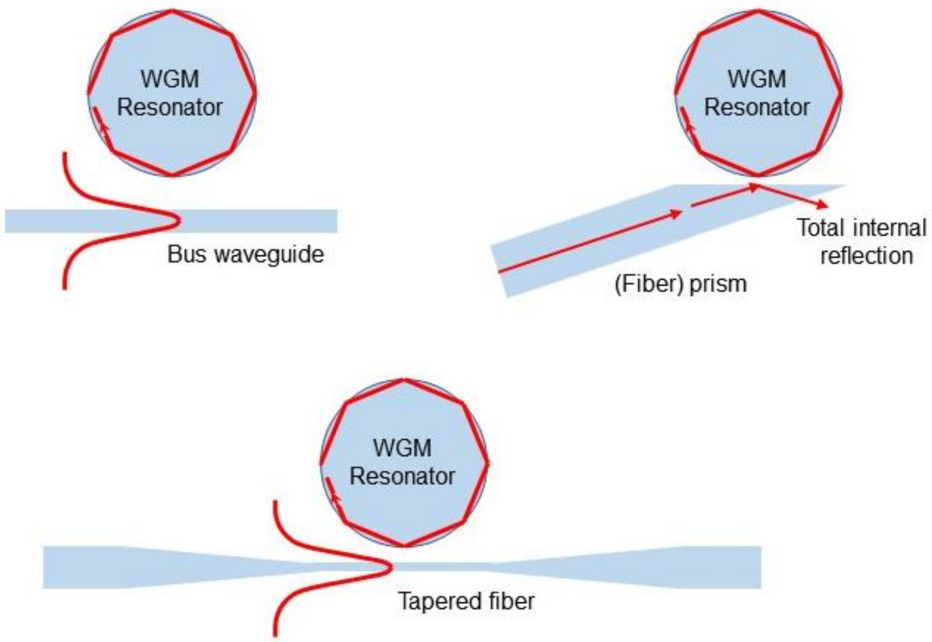

Figure 3.14 - Coupling strategies for whispering gallery mode (WGM) resonators: bus coupling (top-left), prism coupling (top-right), tapered fiber coupling (bottom). The red arrow represents the direction of light propagation. In case of bus coupling and tapered fiber coupling, the red bell-shapes represent the optical field distribution across the waveguide. The optical energy located outside of the physical waveguides was evanescently coupled into the resonator.

3.3.3 Acoustical sensitivity

The acoustical sensitivity A can be expressed as:

$$A = \frac{d\lambda_r}{dP_0} = \frac{d\lambda_r}{dP_{eff}} \times e \tag{3.3.8}$$

where $P_{eff} = e \times P_0$ is the effective ultrasound pressure that interacts with the optical field and e is a coefficient that represents the effectiveness of the detector structure that converts incident pressure into meaningful pressure that actually interacts and induces change with the confined optical energy.

Large acoustical sensitivity means the resonant frequency of the resonator is strongly perturbed by an applied pressure, either via physical deformation of the resonator's geometry or changing of the cavity refractive index due to photoelastic effect. The first term in Equation 3.3.8 is closely related to the acoustical properties of the optical cavity. The stiffer the cavity material is, the smaller this term is. It is the reason why polymers are preferred over rigid materials like glass or silicon for ultrasound sensing applications to gain the acoustical sensitivity. For example, several studies have demonstrated that Bragg grating in polymer optical fiber shows 13-folds acoustical sensitivity improvement compared to Bragg grating silica fiber [127].

The effectiveness coefficient e is often overshadowed by other parameters, i.e. Q-factor or Young's modulus, but plays an important role in the sensitivity of several structures such as membrane-based detectors. For example, a silicon microring has possessed similar sensitivity to a polymer microring despite of having similar optical Q-factor [128,129]. This is counter intuitive once knowing that the Young's modulus of silicon is several orders of magnitude larger than that of polymer. The underlying mechanism here is that the silicon microring was constructed on top of a silicon membrane, which significantly increases the effectiveness coefficient e. In the case of the polymer microring constructed on a rigid glass substrate [129], only the portion of ultrasound wave that hits the ring can be converted into detectable pressure. In case of the silicon microring constructed on the membrane, all the pressure wave that hit the whole membrane induce perturbation to the ring and is detected. Simply speaking, the membrane increases the effective area for collecting ultrasound and propagate all the ultrasound signal toward the ring to be read out optically. For the polymer microring, the ultrasound wave that does not hit the ring but hits the substrate is ignored by the microring – the sensitive element.

There exists an inherent trade-off between optical and acoustical sensitivity. Materials with high susceptibility to pressure such as soft polymer are difficult to process and have high intrinsic optical absorption, resulting in maximum Q-factor reported of around 1×10^5. On the other hand, low-absorbing materials such as silica or silicon nitride tend to be rigid crystalline. However, mature fabrication technology allows such materials to form resonators with Q-factors that are several orders of magnitude higher than polymer resonators. However, as maximum practical Q-factor for OA imaging is on the order of 10^6, polymer-based resonators still show clear sensitivity advantage over silicon or silica-based resonators – if the latter does not incorporate acoustic membrane. The major disadvantage of using acoustic membrane is that the membrane is only sensitive around its acoustic resonant frequency, which reducing the detection bandwidth and resolution as discussed in Section 3.4.

3.4 Resolutions of Optical Ultrasound Detector

3.4.1 Detection bandwidth

The detection bandwidth of an optical ultrasound detector in this thesis is defined as the ultrasonic frequency from the low-frequency cutoff till the high-frequency cutoff at -6dB (25% of the maximum response). The bandwidth depends both on the optical properties and acoustical properties of the detector.

The detection bandwidth of the detector is the primary factor that determines the axial resolution of the OA images in tomographic/mesoscopic schemes. As being shown in Equation 2.3.2, if water is used as the ultrasound coupling medium, a common biomedical piezoelectric transducer with detection bandwidth of 10 MHz produces an axial resolution of only 120 µm. Axial resolution of 10 µm requires the detection bandwidth to reach at least 120 MHz.

Regarding the optical limit, the high-frequency cutoff is limited by the time for the optical resonator to reach a steady state after perturbation. This time amount is estimated to be the effective photon lifetime in the resonator, which is defined as:

$$\tau = \frac{Q}{\omega_r} \tag{3.4.1}$$

The higher the Q-factor, the longer it takes for the resonator to be stabilized and the bandwidth is narrower. This creates a tradeoff between sensitivity and bandwidth in optical resonator, similarly to the case of piezoelectric material. However, this sensitivity-bandwidth tradeoff in optical detectors is much more relaxed than in piezoelectric detectors. For example, at resonant frequency of 1550 nm, an optical resonator with ultra-high $Q = 1 \times 10^7$ has $\tau = 8.2$ ns, thus gives the bandwidth cutoff at around 121 MHz, which is still considered as ultra-wide bandwidth in biomedical ultrasound. An optical resonator with typical $Q = 1 \times 10^5$ has the cutoff of 12.1 GHz, which is enough to collect all practical ultrasound signals.

Acoustical limit is often smaller than optical limit, and thus governs the final bandwidth of the optical detector. In the most popular case where the detector is constructed in a planar substrate that is much larger than the sensing element itself, this limit is often governed by the effective thickness of the sensitive region. For example: polymer resonator such as FPR or microring must be constructed on top of a rigid substrate such as a glass block or cover slip for stable operation. Ultrasound upon impeding on the optical detector hits two interfaces: the detector-coupling media interface and the detector-backing interface. At some frequency, the thickness of the detector (or the acoustical distance between these two interfaces) is equal to the ultrasonic quarter wavelength in the detector material. Hence, the reflected ultrasound from the detector-backing interface interferes destructively with the propagating ultrasound inside the detector, resulting in a dip in the frequency response.

An acoustical dip cutoff at high ultrasonic frequency asks for a small acoustical wavelength in the detector's material. This can be achieved by designing a detector with small thickness or constructing the detector by silica or silicon – materials with large speed of sound. For example, in polymer ($v_s \approx 2500\ \mathrm{m/s}$), ultrasonic frequency of 120 MHz has wavelength of $\sim 21\ \mu\mathrm{m}$. In order to have $10\ \mu\mathrm{m}$ axial resolution, polymer detector should have thickness of around $5\ \mu\mathrm{m}$. For microring structure, this thickness is possible since single mode polymer waveguide could have thickness of less than $2\ \mu\mathrm{m}$ and still produce sufficient sensitivity. However, for Fabry-Perot resonator of this thickness is difficult to fabricate and going to produce inadequate sensitivity.

When the substrate to host the optical resonator has comparable physical dimension compared to the sensitive region of the detector, the situation becomes not as straight forward due to the existence of the diffracted acoustic wave generated from the physical edge of the substrate.

These diffracted wave interference with the acoustic wave transmitted directly from the source into the resonator and create complex frequency response. In most cases, numerical simulations would be required to explicitly predict the frequency response and bandwidth of the detector [130,131].

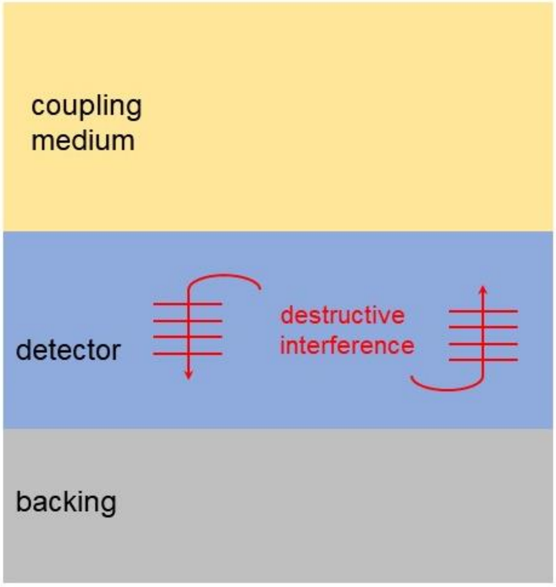

Figure 3.15 - Acoustic interference inside a planar detector. Acoustic wave being reflected at the detector-coupling medium interface and acoustic wave being reflected at the detector-backing interface interference destructively at specific frequencies, resulting in a dip in frequency response at these positions.

3.4.2 Sensing aperture

As being expressed in Equation 2.3.3, the lateral resolution of an optical detector depends on both its axial resolution and its detection aperture. Both large detection bandwidth and small aperture are necessary to have a fine lateral resolution. Since the bandwidth and axial resolution have been treated in the previous section, this section considers only the detection aperture. The sensing aperture of an optical detector can be approximated as the intersection area of the mode field with the sensing surface.

An ideal “point detector” has the sensing aperture equal to zero, thus the axial and lateral resolutions are the same (isometric spatial resolutions). Such point detector does not exist.

Every realistic detector has a finite sensing aperture, and this aperture size smears the lateral resolution from the axial resolution, giving non-isometric spatial resolutions.

a) Fabry-Perot resonators

To obtain small detection aperture, the interrogation beam of FPRs is commonly focused into a spot with micrometer-size. Due to lateral beam walk-off of such tightly focused beam, the projection of the interrogation beam is slightly larger than the focal spot size. For example, in free-space configuration, a 22 μm-diameter spot has been used to interrogate the sensor [109]. In the fiber configuration sensor [111,132,133], as the interrogation beam has diameter that is equal to the mode field diameter of the backing fiber (∼10.1 μm), the actual sensing aperture could be estimated to be 12∼15 μm. In combination with the sensing bandwidth of ∼30 MHz, the imaging resolution of this fiber sensor is theoretically expected to be 40 μm axially and 43 μm laterally. In fact, the characterized resolution was reported to be 65.9 μm axially and 94.2 μm laterally [111].

b) Phase-shifted Bragg gratings

Because each period of the Bragg grating is weakly reflective, the confined light in a phase-shifted Bragg grating penetrates deeply into the Bragg mirror. The "effective sensing aperture" of a phase-shifted Bragg grating therefore has line-shape, with the width being the mode field diameter in the respective waveguide and the length could spread over hundreds of micrometers in the fiber platform [134]. For silicon waveguides, the strong index modulation allows the structures to be miniaturized to hundreds of micrometers, compressing the effective sensing length of less than 50 μm [135].

c) Whispering gallery mode resonators

The aperture of WGM resonators detector are defined as the circumference of the optical mode, and can often be approximated as the outer diameter of the resonators. Polymer microrings often have diameter in the range of 50∼100 µm. Due to the average index contrast (on the orders of ∼0.2) between the polymer waveguides and the surrounded cladding, smaller ring diameter significantly increases the bending loss, resulting in low sensitivity. Therefore, even though the axial resolution of polymer microrings is less than 5 µm, theirs corresponding lateral resolution is approximately 60 µm. This lateral resolution is two to three folds larger than that of state-of-the-art focused piezoelectric transducer, confining applications of polymer microring to OR-OAM mostly. Silicon waveguides could achieve smaller diameter (down to ∼15 µm [128]) thanks to the refractive index contrast that it an order of magnitude stronger than polymer waveguides. Taking into account the characterized bandwidth of ∼70 MHz, the silicon ring detector gives the axial resolution of ∼17 µm and lateral resolution of ∼23 µm theoretically.

d) Photonic crystal resonators

PCRs based on crystal defect have not yet been utilized in ultrasound sensing. One can roughly estimates the optical field to penetrate into tens of period into the slab structure, giving an effective mode field diameter to be approximately the same as silicon microrings.

For guided mode resonators, a tightly focused beam has large beam divergence, yielding strong angular dispersion and thus a lower Q-factor. It was observed that a photonic crystal slab exhibits a resonant linewidth of 0.2 nm when the interrogation beam spot has diameter of 900 µm. As the interrogation beam is focused to 90 µm, the resonant linewidth is broadened to 0.45 nm [136]. This interrogation beam spot can be approximated as the sensing aperture of guided mode resonators. For such resonators to gain sufficient sensitivity, the aperture has to be enlarged to the orders of hundreds of micrometers.

3.5 Discussion

This chapter presents the basic foundations of optical resonators, as well as the theoretical analysis regarding the performances (i.e., sensitivity and resolution) of those resonators for optoacoustic mesoscopy.

Table 3.1 gives a summary of currents optical resonators those have been proposed or could be used to measure optoacoustic signal in mesoscopic imaging. Even though the sensitivity of optical resonators is approaching state of the art piezoelectric transducers, piezoelectric transducers are still showing significant sensitivity advantage due to the simplicity of the read-out circuit. Regarding the resolution aspect, optical resonators lack the aperture miniaturization required to compete with focused piezoelectric transducers using synthetic aperture approach. These are two major challenges that prevent the dissemination of optoacoustic detectors based on optical resonators and will be discussed and solved in the next chapters.

Table 3.1 - Performances of optical resonator-based detector

	Sensitivity				Resolution		
Resonator type	Sensitive element	Q-factor	NEP [Pa]	NEPD [mPa/√Hz]	Bandwidth [MHz]	Aperture [μm]	Resolution, lateral × axial [μm × μm]
FPR	Planar polymer cavity[109]	-	200	40	25	Φ 22	50 × 50
	Plano-concave polymer cavity[111]	1×10^5	4	-	17	-	-
	Plano-concave polymer cavity on fiber tip[111]	-	9.3	2.1	27	Φ 15	94 × 66
pBG	Silica cavity[112]	1.9×10^5	100	25	80	270 × 10	-
	Silicon cavity[135]	2.2×10^4	-	9.8	230	30 × 0.5	16 × 5
WGM resonators	Silica sphere[117]	9.5×10^7	0.5	-	5	Φ 192	
	Polymer microring[116]	4×10^5	10.5	2.1	170	Φ 60	-
	Silicon membrane[128]	2.5×10^4	-	1.3	36	Φ 20	-
	Chalcogenide microring[137]	6×10^5	-	2.2	220	Φ 40	50 × 44
	Silicon nitride microring[138]	6×10^3	-	7	120	Φ 30	47× 15
PhC resonators	2D slab[136]	8×10^3	170	1900	> 40	> Φ 90	-
	2D slab with defect[123]	6×10^5	-	-	-	-	-

Chapter 4 : Hybrid pi-shifted Bragg Gratings for High Resolution Optoacoustic Mesoscopy

4.1 Introduction

One of the major advantages of optoacoustic imaging is the capability to provide optical-contrast images with high resolution at the depth beyond that of purely optical modalities relying on ballistic photons such as light microscopy or optical coherence tomography (OCT). Since the optical focusing is highly inefficient at such imaging depth due to strong optical scattering of tissues [3], high resolution optoacoustic imaging at millimeter scale relies totally on the properties of the ultrasound detector. Fine spatial resolution of less than 20 µm have been proven to benefits a lot of clinical applications such as visualize vascular patterns in the dermis and sub-dermis of psoriasis patients [38], or resolving fine blood vessels in vascular-targeted therapy [34]. These spatial resolutions impose a detection bandwidth of at least 100 MHz and a detection aperture that is smaller than 20 µm.

Miniaturization of a piezoelectric detectors to a few tens of micrometers results in a detector with inadequate sensitivity to detect optoacoustic signal due to the strong dependence of piezoelectric transducers sensitivity on their sizes. The most viable approach with piezoelectric transducers detectors is employing spherically focused piezoelectric transducers, where the focal region of a focused piezoelectric transducers can be treated as a “virtual-detector” [41]. Acoustic focusing is achieved by either using an acoustic lens with a flat piezoelectric element or machining the piezoelectric element to have a spherical curvature [139]. Because the center frequency of a piezoelectric transducers is inversely proportional to the thickness of the piezoelectric active layer, high-frequency detection requires piezoelectric layer with thickness in the orders of few tens of micrometers [15]. Since such thin piezoelectric elements are difficult to shape into spherical geometry, focused piezoelectric transducers used for high resolution optoacoustic imaging mainly employs acoustic lens. The structure of an acoustic lens based focused piezoelectric transducers is depicted in Figure 4.1.

The detection aperture of a focused piezoelectric transducer is closely related to its focal spot size and the working bandwidth. While the axial resolution can be generally expressed by equation 2.3.1, the lateral resolution depends on the focusing capability of the acoustic lens and can be approximated as:

$$R_l \approx 1.07\lambda_c \frac{F}{D} \tag{4.1.1}$$

where λ_c is the center wavelength of the detection bandwidth. However, it should be noted that in practical, the lateral resolution is slightly larger than what calculated from equation 4.1.1 due to the compromising of the low frequency components, while the axial resolution is smaller than the calculated value from Equation 2.3.1 due to the mutually canceling of optoacoustic signals originated from nearby emitters [140]. A typical focused piezoelectric transducer employed in optoacoustic mesoscopy could have the bandwidth of 20-180 MHz, active diameter of 1.5 mm and f-number of approximately 1 [141]. This transducer produces the theoretical resolutions of 16×7 µm, but was characterized to produce the experimental resolutions of 18×4 µm.

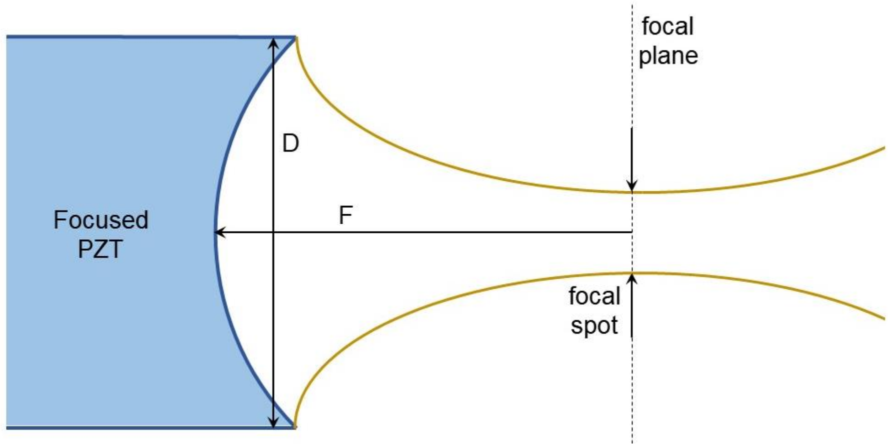

Figure 4.1 - Schematic of a focused piezoelectric transducer. D: diameter of the active element. F: focal length.

In addition to the common limitation of the piezoelectric technology, the implementation of focused piezoelectric transducers in high resolution optoacoustic imaging system induces a small depth of sensitivity. The -3 dB depth of the focal zone of a focused piezoelectric transducer can be estimated as [18]:

$$D_{focal} \approx 7.2\lambda_c \left(\frac{F}{D}\right)^2 \tag{4.1.2}$$

For a conventional focused piezoelectric transducer with $\lambda_c = 50$ MHz and $F = D$, the detector loses half of its sensitivity as the source is shifted 100 μm axially from its focal plane. This rapid deterioration of performance outside of the focal region necessitates accurate alignment of the detector with respect to the optoacoustic absorbers, which is impractical in various clinical applications.

Optical ultrasound detectors provide a more isotropic sensitivity field, and thus could lift the burden of distance alignment between the detector and the samples. However, as revised in Section 3.3.4, optical detectors have challenge approaching the bandwidth and aperture required for a sub-20 μm resolution.

This section proposes a novel optical ultrasound sensor that could theoretically achieve spatial resolution as fine as an ultra-broad band focused piezoelectric transducer. The sensor design is investigated theoretically and realized in two most common photonics platforms: silicon-on-insulator (SOI) and silica optical fibers (SOF). The performance of the sensors is carefully characterized and their capability in high-resolution optoacoustic imaging is demonstrated with tissue-mimicking phantom and biological samples ex vivo.

4.2 Sensor Design and Theoretical Assessment

The smallest dimension at which can be used as the aperture of an optical structure is generally the cross-section of the waveguide in the platform that the structure is built in. Taking this into consideration, a pBG-based detector is proposed, where the cross section of the waveguide is used as the detection aperture. Therefore, a full understanding of how light behaves in phase-shifted Bragg grating is important to optimize the sensor design.

4.2.1 Theoretical assessment tool – Transfer matrix method

In the transfer matrix method (TMM), the optical structure is treated as a series of layers, each layer is optical homogeneous and has infinite lateral dimension (see **Appendix A**). For the case of Bragg grating written in an optical waveguide, light in confined and propagates only in the axial direction of the waveguide, which further simplifies the TMM model to normal incident. TMM therefore becomes a perfect tool to study Bragg grating due to its simplicity.

For pBG, depending on what kind of information needed, the TMM was applied either in combination with the analytical solution or purely. In the former case, by picking up the analytical approach described in Section 3.2.2, a uniform Bragg grating can be treated as a single TMM layer with the characterization matrix [46]:

$$F_{Bragg} = \begin{bmatrix} \cosh(\gamma_B L_B) - i\frac{\hat{\sigma}}{\gamma_B}\sinh(\gamma_B L_B) & -i\frac{\kappa}{\gamma_B}\sinh(\gamma_B L_B) \\ i\frac{\kappa}{\gamma_B}\sinh(\gamma_B L_B) & \cosh(\gamma_B L_B) + i\frac{\hat{\sigma}}{\gamma_B}\sinh(\gamma_B L_B) \end{bmatrix} \quad (4.2.1)$$

where $\gamma_B = \sqrt{\kappa^2 - \hat{\sigma}^2}$ and L_B is the length of the grating section. A pBG is therefore modeled as a three-layer TMM, wherein a layer that represents the pi-shifted cavity being sandwiched between two uniform grating sections. The characteristic matrix of the pi-shifted cavity can be derived from Equation 7.1.1 with $P = 1$. The advantage of employing the TMM modeling in comparison with purely analytical approach using Equation 3.2.25 is the ease of incorporating additional optical layers into the grating structure. This first approach is called “combined TMM” in this thesis, and quickly provide the spectral response of the grating structure without computational burden.

In the “pure TMM” approach, the whole pBG is sectioned into thin layer with thickness of sub-grating period (Figure 4.2). This approach is computation-intensive while computing the spectral response but could provide additional information about how the optical field is distributed inside the grating structure for a single interrogation wavelength. By extracting the amplitude of the forward and backward-propagating component of the electromagnetic field at each layer, a map of optical energy distribution could be generated.

4.2.2 Optical distribution inside a Bragg grating

First, the optical distribution inside a uniform Bragg grating is assessed using the “pure TMM” approach. The grating parameter used in this section is taken from [65] for a grating based on silicon-strip waveguide. The waveguide has effective refractive index of 2.4622, grating length of 125 µm, Bragg wavelength of 1550 nm and a corrugation depth of 50 nm, which corresponds to an effective AC index modulation of 0.0177.

Unlike metallic mirrors, where light is reflected at the surface of the mirror, optical reflectors based on Bragg grating have large penetration depth as depicted in Figure 4.3a. The zoom-in picture in Figure 4.4b shows that light is partially reflected at each dielectric boundary, resulting in a gradual decrement of the maximums toward the end of the grating. The rate of

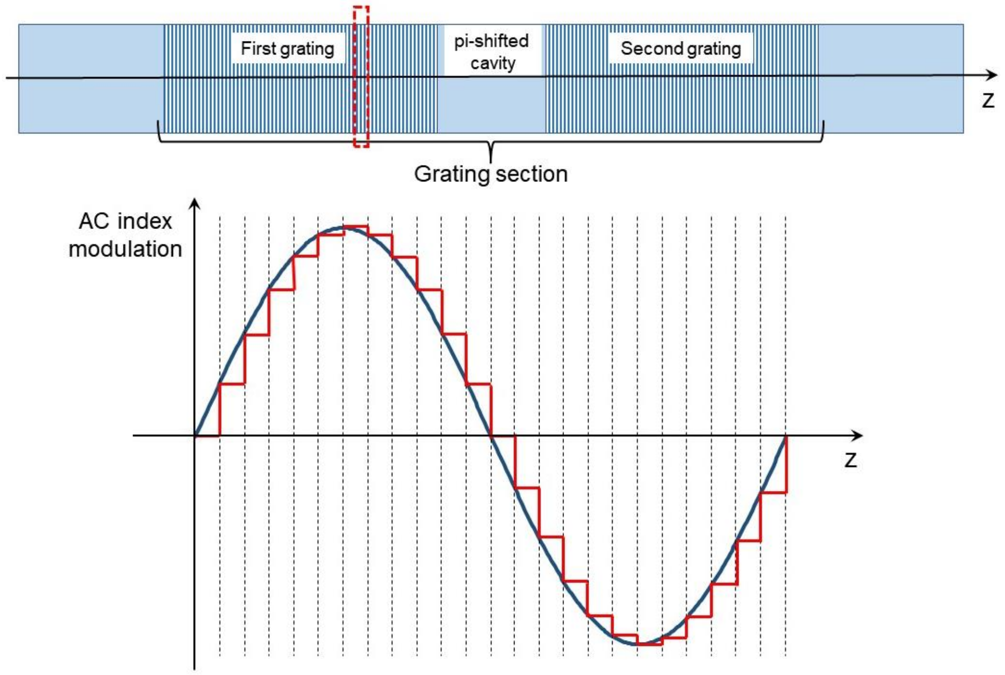

Figure 4.2 - Sectioning in the pure Transfer Matrix Method (TMM) approach. Each grating period (dashed red rectangular in the top image) is sectioned into equal subsections. The index is discretized to be uniform in each subsection.

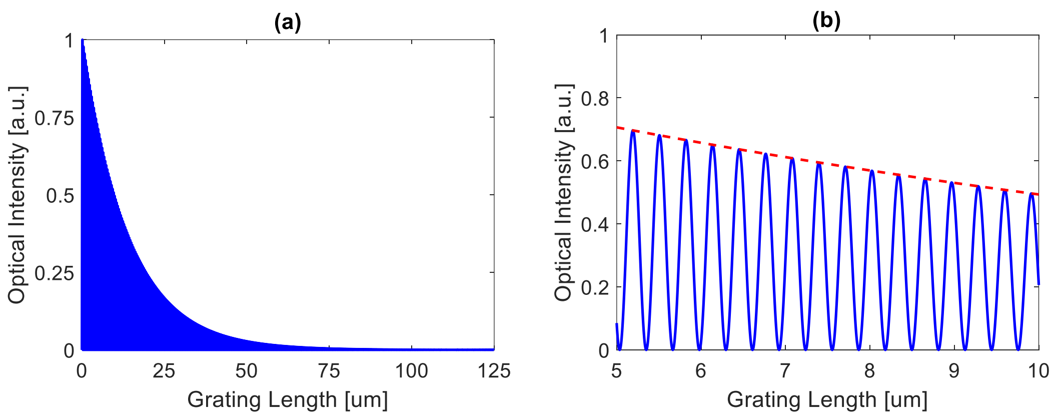

Figure 4.3 - Optical field intensity inside a Bragg grating. (a) Over the whole grating length of 125 µm. (b) Zooming into a 5-µm section from 5 to 10 µm of (a). The red dashed curve represents the envelope of the optical intensity distribution.

the intensity decay depends on the strength of the grating (the AC index modulation). The optical field inside a Bragg grating is modulated with the same period as the grating period, and the minimums reach zero. For the ease of illustration, the optical intensity will be plotted as the envelope of the real intensity (the red dashed curve in Figure 4.3b) in the rest of this thesis. Using equation 3.2.17, the AC coupling coefficient of the above Bragg grating is calculated to be $\kappa \approx 35.9$ mm^{-1}. The strong coupling regime ($\kappa L_B > 3$) starts at the grating length of 83 µm. Only less than 0.25% of the incident optical energy reaches beyond this grating length.

Next, a pi-shifted cavity is introduced between two identical Bragg grating (total grating length of 250 µm). At the resonant frequency, where the optical path length of the cavity corresponds to half the optical wavelength in the waveguide, optical intensity is built up strongly.

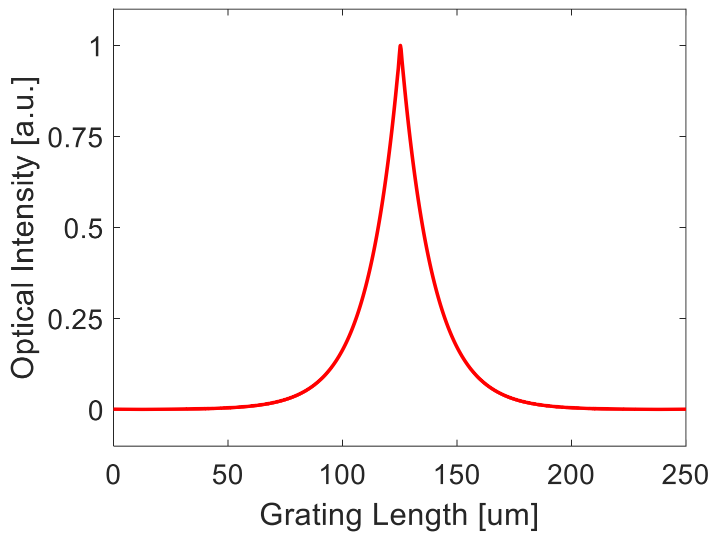

Figure 4.4 - Optical intensity inside a pi-shifted Bragg grating with total length of 250 µm. The pi-shifted cavity is located at the center of the grating.

4.2.3 The hybrid pi-shifted Bragg grating design

It is intuitive from Figure 4.4 that if the cross section of an optical waveguide with pBG is used for ultrasound sensing, the ultrasound wave interacts with very small optical intensity at the end of the grating. Since the sensitivity of an optical ultrasound detector is proportional to the amount of light interacting with the ultrasound wave, it is important for the surface of the sensor to be located in proximity of the optical cavity – where majority of the optical energy is located. However, as the first grating-based mirror gets reduced in length to bring the sensing facet closer to the cavity, its reflectivity decreases and the optical intensity stored inside the resonator drops simultaneously. Figure 4.5 illustrates the relative optical intensity inside a pBG with the length of the second grating being fixed at 125 µm and different lengths of the first grating. As the grating length reduced by 15 µm (12% of the original length), the maximum optical intensity located at the cavity decreased by five-fold. The significant drop of optical intensity is explained by the reflectivity loss. The reflectivity of a Bragg mirror at an arbitrary wavelength can be calculated by the ratio between the interrogation wave and the reflected wave from the grating at that specific wavelength using the TMM (See **Appendix B**).

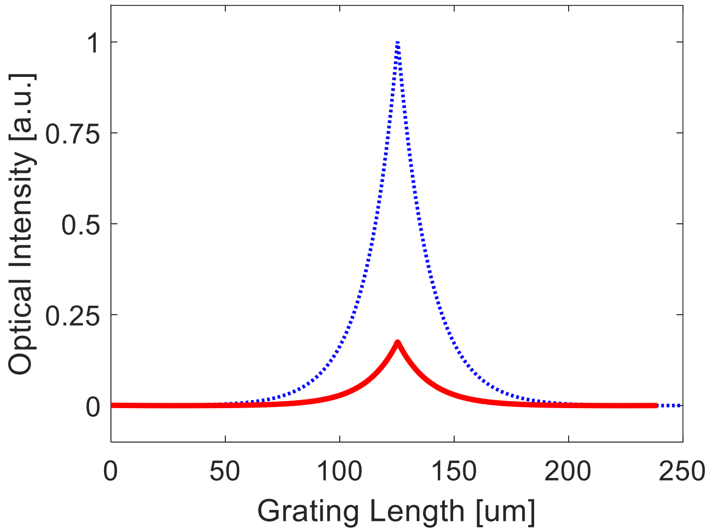

Figure 4.5 - Optical intensity distribution inside pi-shifted Bragg gratings when removing part of the grating. Blue dashed curve: both sides of the cavity have grating length of 125 µm. Red solid curve: reducing one side of the grating to 110 µm.

As the sensing facet moves closer to the pi-shifted cavity, a thin metallic mirror was proposed to compensate for the reflectivity loss of the Bragg mirror. The metallic mirror could provide high reflectivity of more than 95% while being less than 1-µm-thick, keeping the optical cavity close enough to the sensing surface. This sensor design is named "hybrid pi-shifted Bragg grating (hpBG)" within this thesis and having detail structure of the sensor is depicted in Figure 4.6.

When a thin layer of silver is coated at the facet, the overall reflectivity of the second mirror is recovered and the optical intensity increases. The silver coating can be easily embedded in the

TMM formalism. The refractive index of silver used in this thesis is $\widetilde{n_{Ag}} = 0.1444 + 11.366$. The reflectivity of the silver coating depends on its thickness, with the thicker layer giving higher reflectivity. The effect of the silver layer on the optical intensity inside the hpBG is illustrated in Figure 4.7.

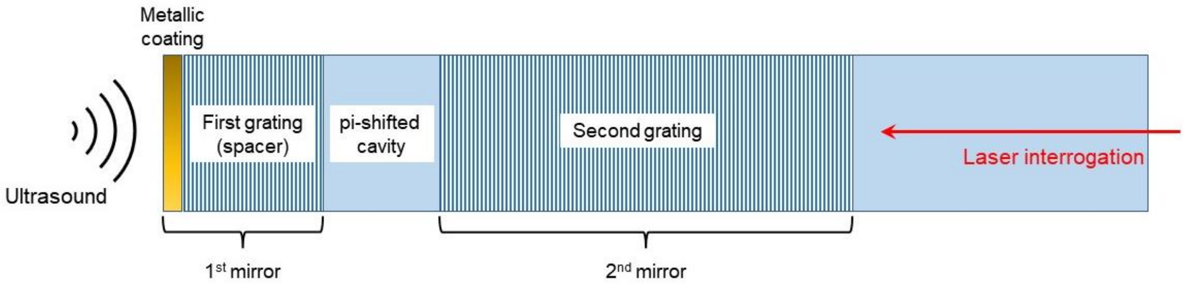

Figure 4.6 - Structure of a hybrid pBG. The grating section that is closer to the ultrasound detection surface is partially removed. The lost in reflectivity of this grating is compensated by a thin metallic coating.

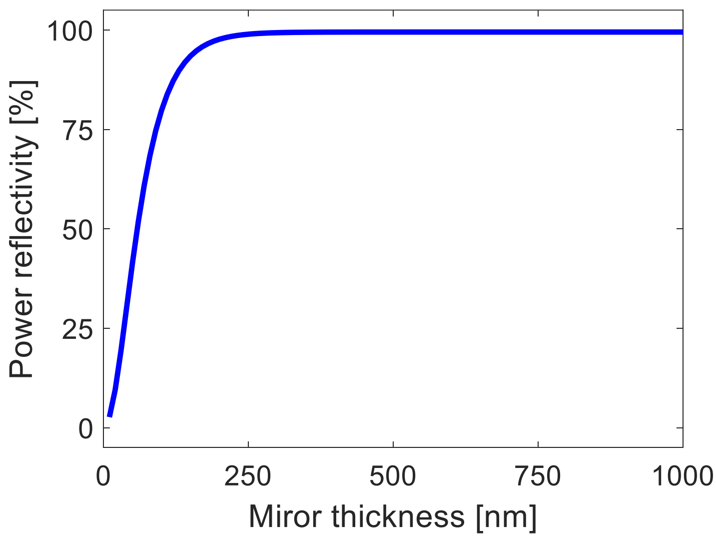

Figure 4.7 - Reflectivity versus thickness of the silver coating.

With proper removal of the first Bragg grating and compensating the reflectivity loss with a thin metallic mirror, the strong optical intensity at the pi-shifted cavity could be interacting with the ultrasound wave and giving rise to the ultrasound sensitivity.

4.3 Realization of the Hybrid pi-shifted Bragg Grating in Silicon-on-Insulator

4.3.1 Sensor fabrication and basic characteristics

The SOI platform has several fundamental advantages compared to other photonics platforms. First, SOI supports the highest refractive index contrast between the waveguide and the cladding ($\Delta n \approx 2.3$), thus miniaturizes the cross section of the single-mode optical waveguide to approximately 500 nm x 220 nm. Being utilized as the detection aperture, this cross section is at least an order of magnitude smaller than the acoustic wavelength at 200 MHz and negligible smears the lateral resolution. The theoretical spatial resolutions then would be isometric in lateral and spatial resolutions. Secondly, the Bragg grating in silicon waveguide is physical corrugation of the waveguide's width and can be optically visualized. The visualization of the pi-shifted Bragg grating allows precise control of the grating removal without damaging the pi-shifted cavity.

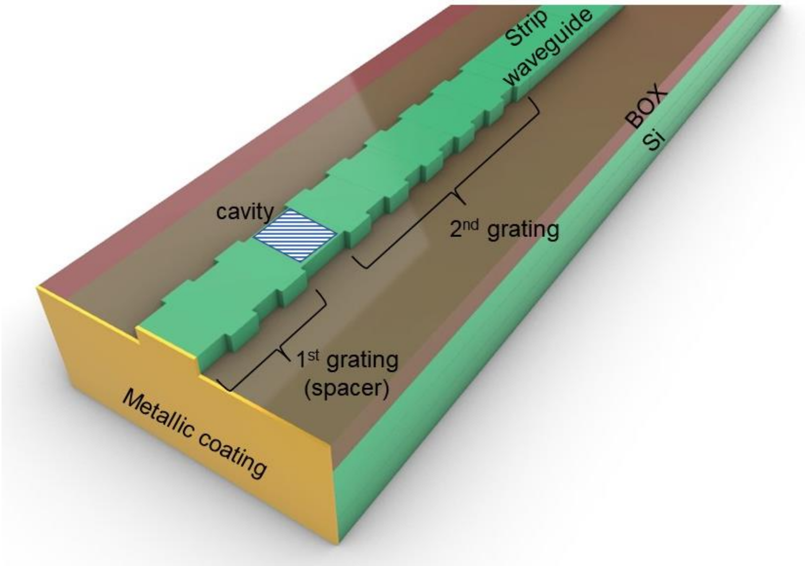

Figure 4.8 - The hybrid pBG in silicon-on-insulator. The pBG is created on a single-mode silicon strip waveguide.

The realization of the hpBG in SOI was first proposed in [142] and named SWED (Silicon Waveguide Etalon Detector). In short, a pBG was fabricated on a single-mode silicon strip waveguide. The two Bragg mirrors are 125-µm-length and have AC coupling coefficient $\kappa \approx 0.009$. The first Bragg grating mirror was partially removed by polishing the sensing facet of the SOI chip, leaving a small spacer length of a few micrometers. A silver coating was then applied on the sensing facet. The final optical Q-factor of the SWED varies from 1×10^4 to 2.2×10^4 depending on the spacer length [142].

The SWED was characterized to have sensitivity of 45 Pa over a characterization bandwidth of 25 MHz (NEPD = 9 mPa/√Hz) and a detection bandwidth up to 230 MHz [142]. Using a near-field approach, the aperture size of this sensor was confirmed to be 650 nm, which is in good agreement with the cross-section size of the mode field diameter in single-mode silicon strip waveguide. These characteristic enables a theoretical resolution of 5.2 µm in both lateral and axial directions.

4.3.2 Resolution characterization

The resolutions of the SWED were experimentally assessed by scanning it over an optoacoustic point source and calculate the point-spread function (PSF) of the reconstructed image of the point source [143]. The optoacoustic point source was created by focusing a nano-second laser beam onto a 200-nm-thick gold film deposited on a cover slip. The detailed structure of the optical system used for characterization and imaging purposes is presented in **Appendix C**. The lateral size of the optoacoustic source is determined by the focal spot diameter of the objective lens used in the setup and is approximately 2.2 µm [144]. The ultrasound sensor is aligned on top of the optoacoustic source and line-scanned (see **Appendix E**). Two important features should be notice during performing the line scan of the sensor. First, the Shannon-Nyquist sampling condition should be satisfied. This means the scanning step size should be at least two-times smaller than the lateral resolution and the product of sampling period and speed of sound in the coupling media (here water) should be at least two-times smaller than the axial resolution. Second, the scanning range should be adjusted to fully cover the acceptance angle of the detector. Insufficient covering of the acceptance angle could deteriorate the lateral resolutions. However, the SWED was characterized to have the acceptance angle as large as 148^0, resulting in the scanning length of seven-fold larger than the imaging distance. These scanning lengths at large imaging distances cannot be fulfilled by the traveling range of the motorized stages and the space of the characterization systems.

To fully investigate the SWED in optoacoustic mesoscopy, the resolutions of the SWED was characterized with imaging distance varying from 0.2 to 10 mm – the whole imaging distance range that is interested in mesoscopy. For example, Figure 4.9a depicts the line scan of the SWED over the optoacoustic point source at two different imaging distances of 0.2 mm (top) and 7 mm (bottom). The line scan signals on the left side comprise of various ultrasound waves, including surface acoustic waves (SAW), main longitudinal wave, reflected waves, etc. (see **Appendix F** for a detail explanation of each type of wave). All these signals are then back projected in the frequency domain [145] to obtain the PSF at the respected imaging distance, as exhibited in the right side. As can be observed, the point source does not reconstruct perfectly as the result of additional waves and the limited viewing angle [143,146].

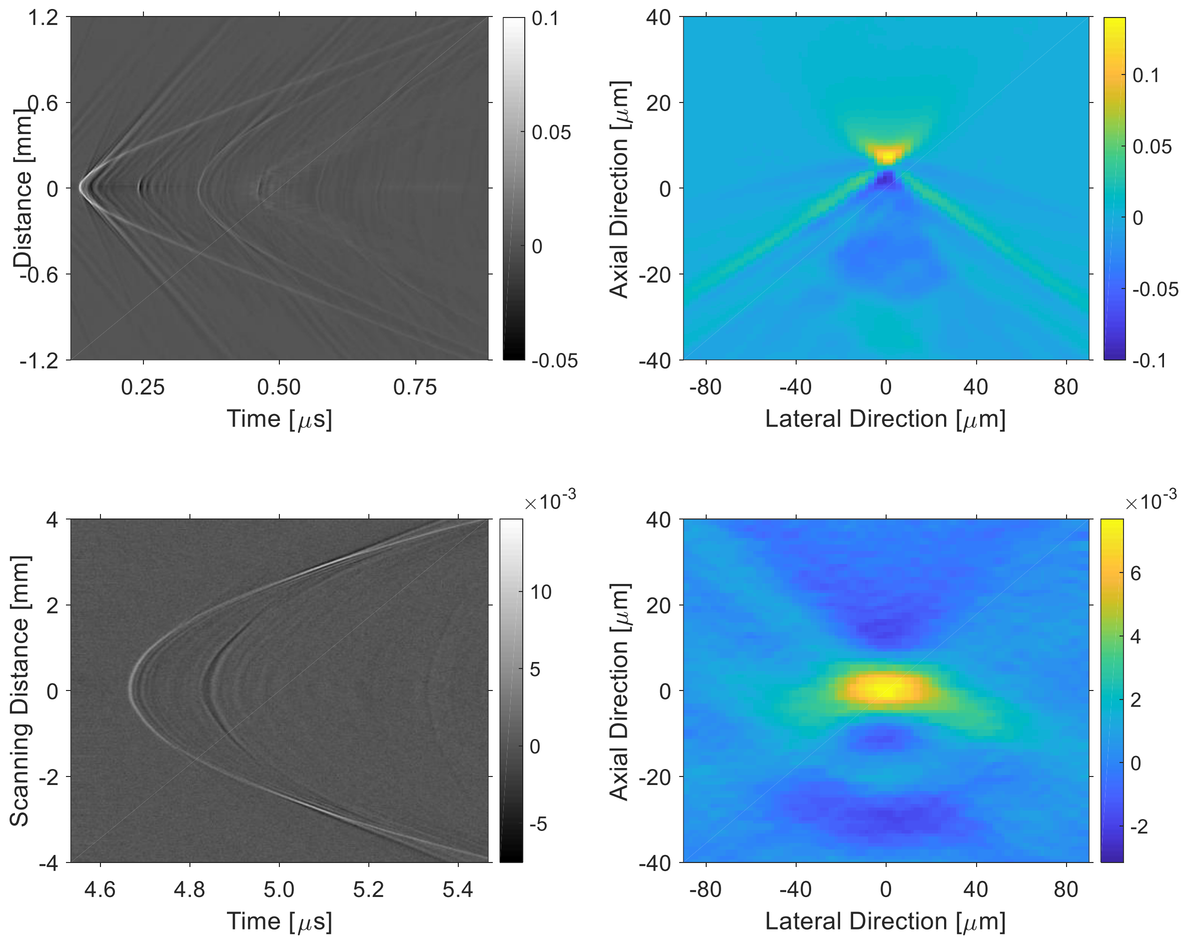

Figure 4.9 - Point spread function measurement of the SWED. The raw scan data are on the left and the reconstructed PSF are on the right. Top row: distance of 200 µm. Bottom row: distance of 700 µm.

For the silicon-water interface used in the case of the SWED, the critical angle for SAW excitation is 17.5^0. At imaging distance of 0.2 mm, the SAW is generated as the offset distance between the sensor and the OA source is larger than 65 µm. Therefore, a large amount of SAW is included in the reconstructed data, leading to the noticeable elongated diagonal artefacts toward the four corners of the figure. At imaging distance of 7 mm, SAW appears in the line scan data as the scanning distance reaches beyond 2.1 mm. The PSF at 7 mm then converges much better than at 0.2 mm with barely visible diagonal artefacts.

Figure 4.10 exhibits the lateral and axial resolutions of the SWED as a function of the imaging distance. The axial resolution deteriorates slowly from 4 µm at 0.2 mm distance to 10 µm at 10 mm, mainly attributed to the acoustic attenuation of high frequency ultrasound signal [143]. The lateral resolution degrades at a much faster rate, from 14 µm at 0.2 mm distance to 108 µm at 10 mm. In additional to the acoustic attenuation, several reasons are responsible for this rapid enlargement of the PSF. First, due to technical limitation of the system, the actual coverage angle decreased quickly with imaging distance, leaving the sensor's acceptance angle not sufficiently covered by the line scan [147]. Second, it was found that the optoacoustic point source produces insufficient ultrasonic pressure for the SWED to detect at large distance. However, if the power of the laser beam used to generate the optoacoustic point source increases to enhance the ultrasonic pressure, the laser fluence becomes so strong that the deposited gold layer is damaged, and the acoustic pressure is affected. Therefore, upon increasing laser power with respect to the imaging distance, the optoacoustic source was enlarged in size subsequently by slightly defocusing the objective lens.

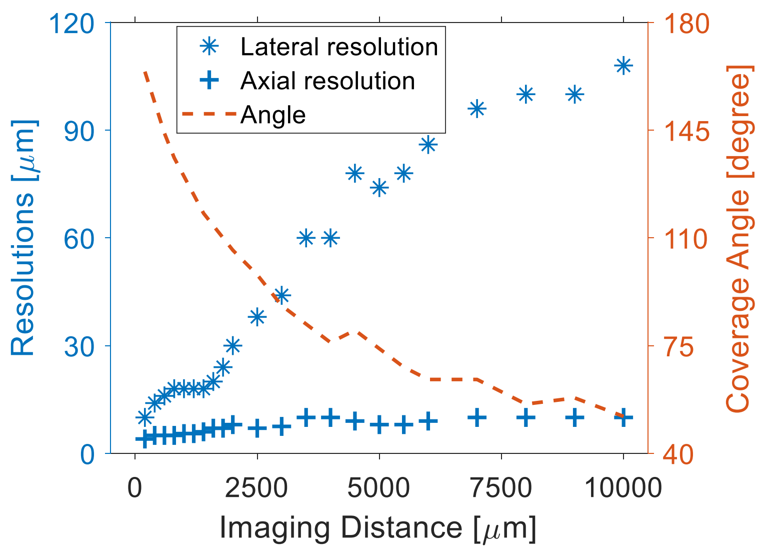

Figure 4.10 - Characterized spatial resolutions of the SWED with respect to distance.

The SWED is capable of providing spatial resolutions finer than 18 x 6 µm over 1.5 mm imaging distance, which is comparable with the resolutions of ultra-broad band focused piezoelectric transducers at their focal distance. At 0.5 mm distance, the resolutions were characterized to be 16 x 5 µm. While the axial resolution matches well with the prediction value of 5 µm, the lateral resolution is smeared from theoretical value of 5 µm to the experimental value of 16 µm. This deviation from theory can be explained by the contribution of the spherical wave emitted from the edge of the object, which excites SAW that propagate with different speed from the longitudinal wave and does not converge coherently [143]. Despite this lateral blurring effect, the SWED still exhibits one of the best OA acoustic resolutions to date, outperforming other optical ultrasound detectors in the resolution aspect.

4.4 Realization of the Hybrid pi-shifted Bragg Grating in Silica Optical Fibers

4.4.1 Motivation

The SWED developed on highly integrated SOI platform has remarkably improve the resolution of OA mesoscopy, but still possesses several disadvantages:

- To achieve such high resolution, ultrasound frequencies of above 100 MHz should be collected. Such high ultrasonic frequencies attenuate rapidly in both tissues and ultrasound coupling mediums, which necessitates the SWED to be located within several millimeters from the desired imaging volume. In many cases, the regions of interest locate deep inside the body, so the imaging head (including light deliver and ultrasound detector) must be inserted percutaneously or through a natural orifice by integrating into a probe such as needle or catheter [8,148,149]. Miniaturization of the ultrasound detector is the more critical here because a small imaging head reduce the size of the probes, allowing minimal invasive treatments and significantly reduce postoperative pain and discomfort [150]. However, miniaturization of SWED in particular and silicon photonics in general to few hundreds of micrometers is not straight-forward. Even though the sensor itself is very small, decreasing the physical dimension of a silicon chip requires additional mechanical works. More importantly, at such small scale, SOI chip lacks the stability required to operate in dynamic clinical environments due to the presence of the so called “optical packaging”- or “photonic packaging” [151]. Since being an indirect band gap semiconductor, silicon itself is not a proper material to build laser cavity. Operation of silicon photonic chips therefore ask for interrogation light to be coupled from an external laser into the chip, normally via an optical fiber. The strong index contrast in silicon photonics then becomes a double-edge sword because on one hand it enables device miniaturization, but on the other hand it creates a huge difference in mode field diameter between the silicon waveguide (typically 0.5 x 0.22 µm for a single-mode silicon strip waveguide) and the optical fiber (typically 10 µm in diameter for single mode fiber at 1550 nm) (Figure 4.11). Only a small fraction of optical energy will be coupled to the chip by direct gluing with the optical fiber, so special strategies were developed for fiber-to-chip coupling (Figure 4.12) [152,153]. The additional optical and mechanical components involved in the optical packaging significantly enlarge the space needed for operation of chip-based sensors.

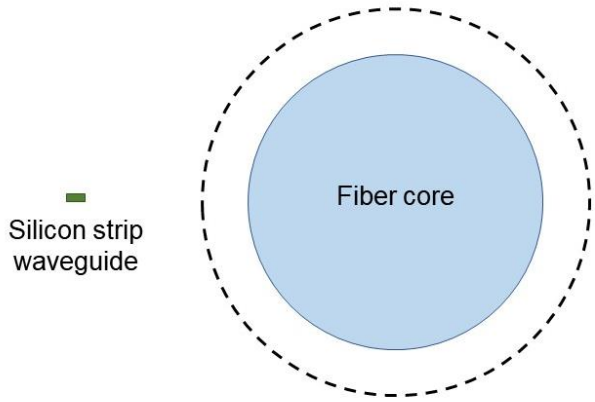

Figure 4.11 - Cross section of a single mode silicon strip waveguide and optical fiber. The dashed circle enclosing the fiber core represents the mode field diameter, which is slightly larger than the physical core.

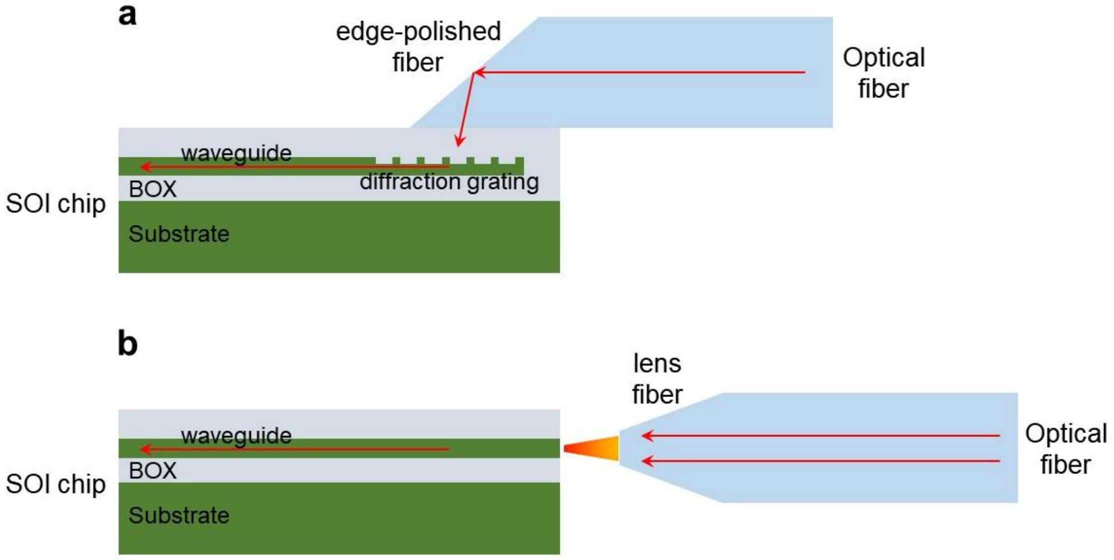

Figure 4.12 - Fiber-to-chip coupling strategies: (a) vertical coupling. (b) edge coupling.

- SWED is relatively not sensitive enough to capture small ultrasound perturbations, putting requirement on signal averaging over a large number of measurements and elongating the measurement time. As being analyzed in section 3.3, the sensitivity depends on the Q-factor and the mechanical properties of the sensors. SWED has Q-factor of around 10^4, partially being limited by waveguide loss. Silicon also has high resistance for acoustic perturbation with Young's modulus almost two orders of magnitude larger than that of water. The combination of these two gives a reported NEPD of 9 mPa.Hz$^{-1/2}$. Even though the sensitivity per sensing area of the SWED is extremely high [142], the absolute sensitivity without considering the sub-micrometer aperture is not among the best of optical ultrasound detectors.

- Silicon photonics is generally not accessible. Fabrication of silicon photonics chip relies on expensive machines from semiconductor foundries, which have cycle time of at least several months [115]. This becomes an obstacle in biomedical fields because the rapid variation in the working environments necessitates the sensors to be adjusted quickly in design to adapt with different requirements of the applications.

- Silicon detectors are susceptible to SAWs due to the huge acoustic impedance mismatch and large sound speed different between silicon and water. This has resulted in the lateral blurring effect as observed in previous section, making the sensor not fully exploit the ultra-small aperture.

By embedding the hpBG structure into SOF platform, we created the Embedded Etalon Resonator (EER) detector which solves all the above problems due to the following justifications:

- By constructing a hpBg sensor in the core of an optical fiber using FBGs, the sensor inherently has the outer diameter equal to that of the fiber, which is only 125 µm for single-mode fiber without any machining processes and the sensing aperture being the mode field diameter within the fibers. These parameters are strictly controlled by the industrial standard, ensuring a high batch-by-batch repeatability. Most commercial lasers provide fiber-coupled output or can be easily couple to optical fiber by simple lenses with high efficiency, so fiber-based sensors eliminate the packaging and miniaturization problem associated with SOI technology.

- Optical fiber is several orders of magnitude less lossy than silicon waveguide, allowing optical resonator based on Bragg grating with Q of around 10^6 to be constructed easily. The higher optical Q-factor enables improvement of the sensor's sensitivity.

- Fiber is a cheap and widely available technology. The fabrication of a batch of FBGs could take maximum a few weeks (including lead time and shipping time), enabling rapid prototyping of biomedical instruments.

- SOF has acoustic impedance that is 1.5 folds smaller and sound speed closer to water than silicon does. Furthermore, the overall area of the detection surface in fiber is only 125 µm, which is 200-folds smaller than the detection surface of the SWED. The small detection surface leaves less "room" for SAWs to be generated, decreasing the amplitude of SAWs and thus their effect in the final PSF.

4.4.2 Fabrication

The major challenge of realizing the hpBG structure in optical fibers is to have a Bragg grating at the tip of the fiber. Due to the requirement of stable immobilization of the fibers during grating inscription, Bragg grating can only be written in the middle of a fiber section with limited precision control. The fabrication of the EER then relies on commercialized pFBG as the precursor. The pFBG used in this thesis was purchased from TeraXion Inc, Canada with the grating being UV-inscribed on polarization maintaining fibers (PMF). The total length of the grating section is 4 mm, including two 2-mm-long Bragg mirrors separated by a sub-micrometer-length pi-shifted cavity. The designed resonant frequency locates around 1549 nm and the AC index modulation is approximately 7×10^{-4}, giving width of the stop band being around 1 nm.

The fabrication steps of the EER are illustrated in Figure 4.13. First, the original pFBG was cleaved close to the grating section. Then, the cleaved tip was slowly polished to remove partially the Bragg mirror closer to the tip (the first Bragg mirror). After reaching a desired remained length of the first mirror (called spacer length), the tip was coated with a thin metallic mirror to recover the reflectivity loss due to grating polishing. The major challenge in fabricating the EER arises from the invisibility of the grating in optical fiber, which challenges the precise determination of the Bragg grating and the spacer length at the sub-millimeter scale. The first and the second step were then conducted through indirect determination of the grating location without optical visualization.

In the first step, the location of the grating section was roughly determined by scanning a small ultrasound transducer along the optical fiber. The pFBG itself can be used as an ultrasound transducer [134,154], where ultrasound signal impeding on the fiber section surrounding the pi-shifted cavity induces an acoustic signal to be detected. The experiment setup is depicted in Figure 4.14. The pFBG was taped on the bottom of a shallow water bath (the height of the water level is less than 5 mm from the bottom). The interrogation laser was locked at the position of maximum slop in the resonant dip, and the reflected optical signal was AC coupled to the input of a digital oscilloscope. We used a small ultrasound transducer (Atlantis PV intravascular probe – Boston Scientific, USA with piezoelectric element area of 0.8 mm^2) to point toward the fiber and slowly scan along the pFBG. When the transducer is scanned over the grating section, an ultrasound signal appears in the oscilloscope. The signal reaches its maxima when the transducer pointing toward the pi-shifted cavity. Then this location on the optical fiber was marked by a black marker. The optical fiber was then cleaved by approximately 5 mm away from the marked position to avoid touching the grating section.

Next, the pFBG was slowly polished away part of the Bragg mirror. In order to reach a desired spacer length without removing the pi-shifted cavity, the spacer length has to be measured with precision on the orders of few tens of micrometers. This task was completed by spectrum matching method. The experiment setup of this step is illustrated in Figure 4.15. First, the polymer coating of the pFBG was stripped away using a single-mode fiber stripper. The length of the stripped section is around 3 cm. After being wiped several times with iso-propanol, the fiber is inserted onto a temporary fiber holder (BFT1, Thorlabs Inc., USA) with a ceramic ferrule (B30126C3, Thorlabs Inc., USA). The fiber holder was then placed in a fiber polishing disk (D50-FC, Thorlabs Inc., USA) and the fiber tip was polished with a diamond lapping sheet of 3 µm grid (LF3D, Thorlabs Inc., USA). During the polishing process, the spectrum of the pFBG was monitored using an IR swept tunable laser (ITUNX, Thorlabs Inc., USA). The tunable laser was set to continuously sweeping the output wavelength from 1547 to 1551 nm and backward. The reflected optical signal from the pFBG was directed to a balanced photodetector (PDB480C-AC, Thorlabs Inc., USA) by a fiber circulator. The monitor output of the photodetector was DC-coupled to a digital oscilloscope (DS1102E, Rigol, USA). This setup allows direct capturing of the spectrum of the pFBG during the polishing process.

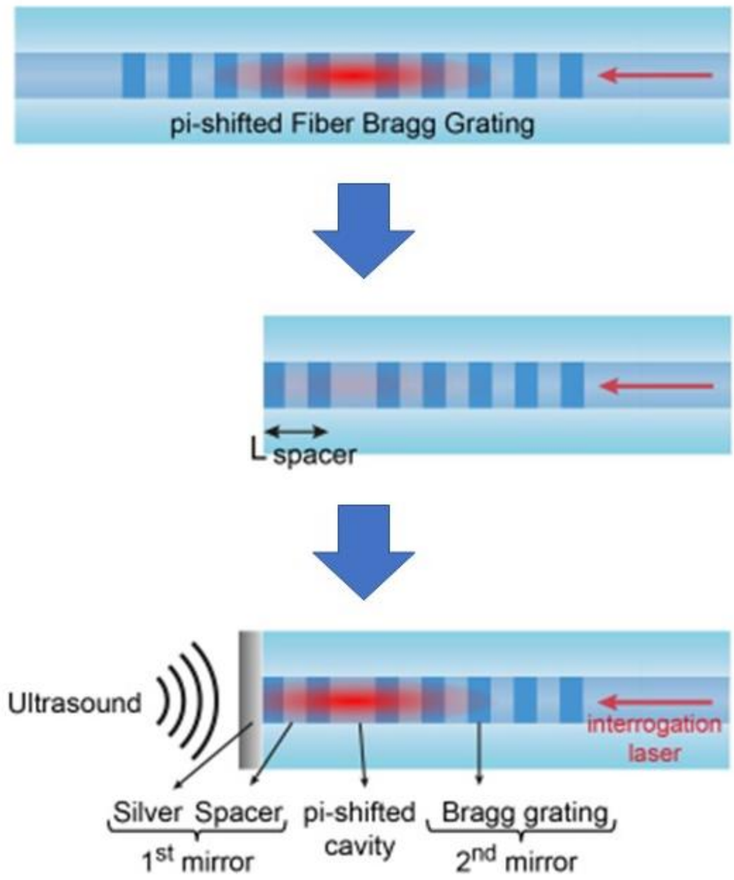

Figure 4.13 - Fabrication steps of the Embedded Etalon Detector (EER). A pFBG is partially polished to shorten the distance between the cavity and the fiber tip (detection surface). Then a silver coating is applied on the tip of the fiber.

We simultaneously ran a TMM-based simulation to identify the current spacer length of the pFBG based on the recorded spectrum from the oscilloscope. The polished pFBG can be modeled using the TMM, comprising four layers (four matrices): the outer air layer, the first Bragg mirror (the polished side of the grating), the pi-shifted cavity and the second Bragg mirror (Figure 4.16). Note that the outer air layer must be introduced to accurately reflect the behavior of the pFBG in air. This air layer has infinite thickness, thus does not induce any reflection after light escaping the fiber. The second Bragg mirror has its thickness fixed at 2 mm. The first Bragg mirror has thickness (spacer length) varies from 2 mm down to 0 mm to find the spacer length that makes the output spectrum of the simulation matches the best with the recorded spectrum from the oscilloscope.

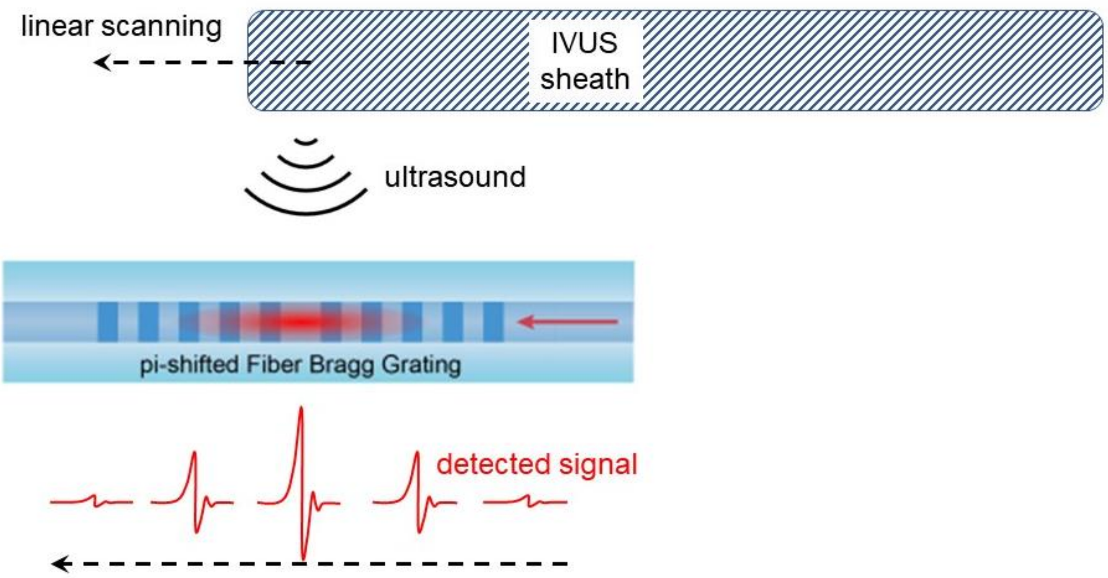

Figure 4.14 - Finding the location of the grating section. An ultrasound emitter (IVUS) is linearly scanned along the pFBG. The pFBG is interrogated to work as an ultrasound detector.

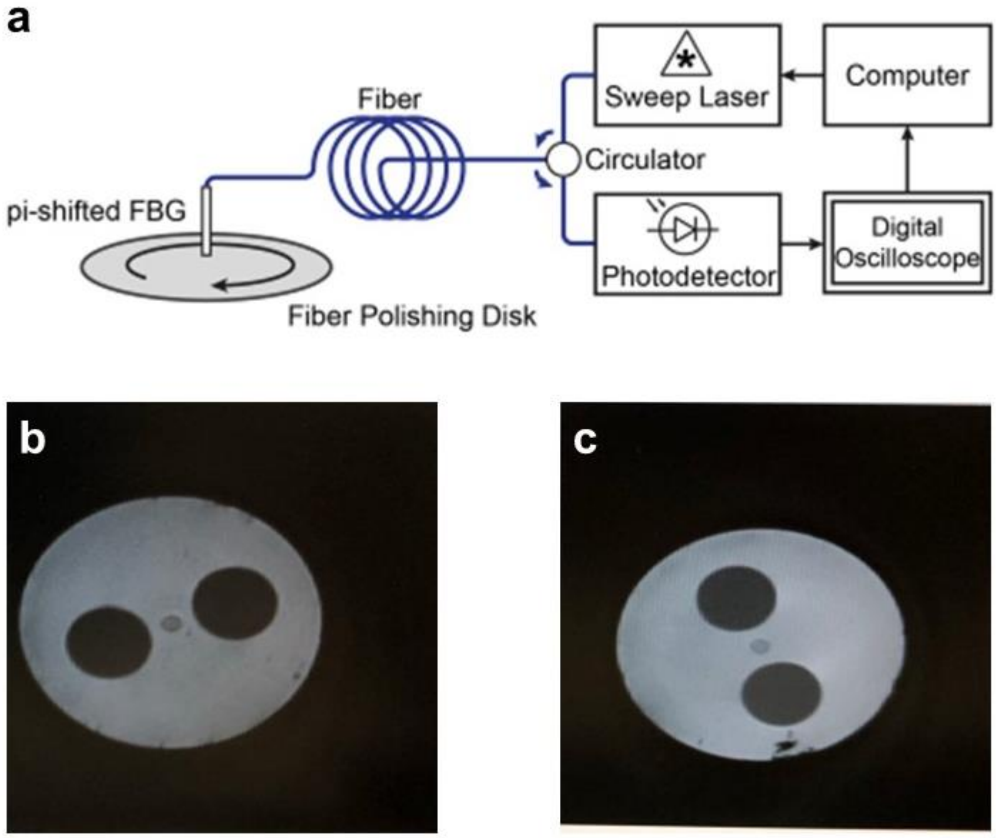

Figure 4.15 - Polishing setup for EER fabrication. (a) The pFBG is interrogated by a sweep tunable laser during polishing. The laser constantly sweeps the interrogation wavelength over the stop band of the pFBG. The reflected spectrum is measured by a photodetector and digitalized by an oscilloscope. (b, c) Microscopic image of the polished tip of two EERs showing the quality of the surface after fine polishing.

Some noticeable features can be noticed from matching the simulated spectrum with the real spectrum of the pFBG during the polishing process. First, a pi-shifted cavity always induces a resonant dip located at the center frequency of the stop band. However, as some fabrication tolerance exists in manufacturing of real pFBG, the cavity length does not correspond to a pi-shift in phase for the design wavelength of 1549 nm. Therefore, a small modification was added to either the cavity length or the effective index of the cavity (Fig. 4-17). This modification helps the resonant frequency of the simulation precisely matches the realistic value without inducing additional error to the simulation.

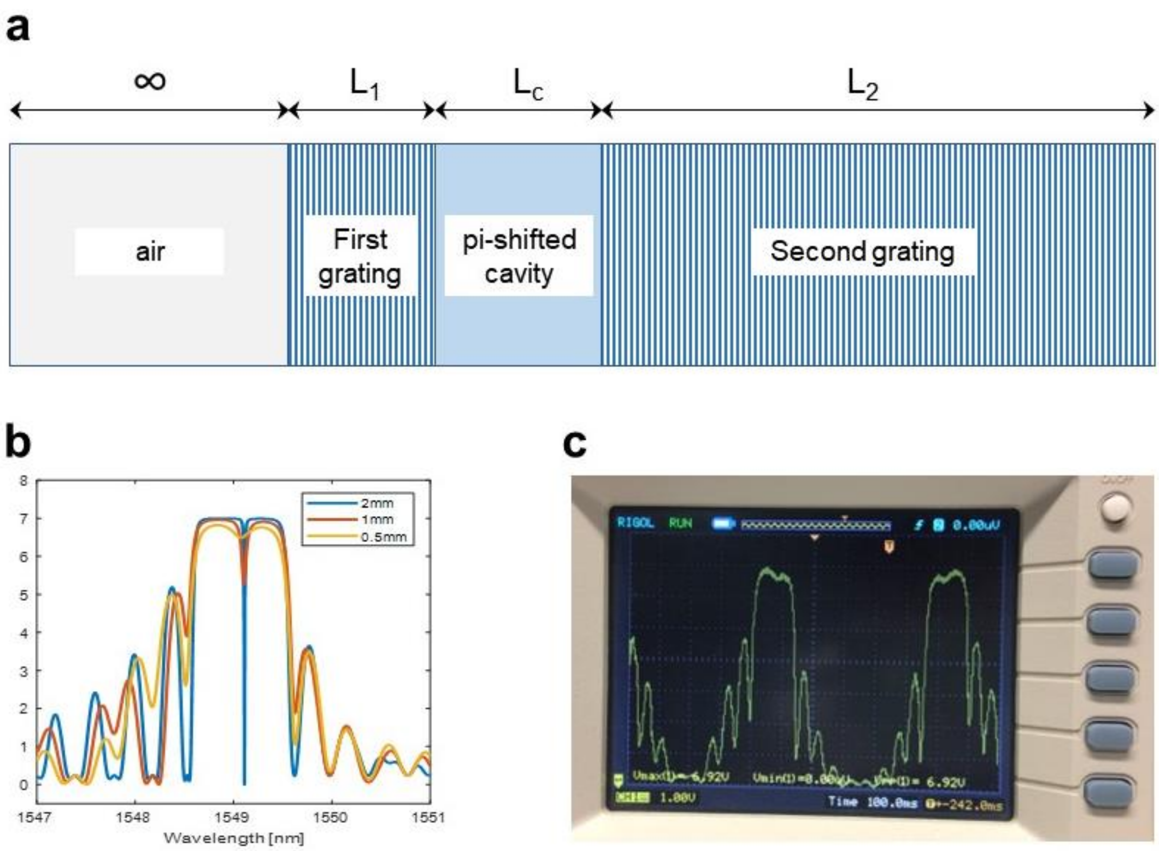

Figure 4.16 - Spectrum matching method. (a) The TMM model used for simulation of the spectrum of the pFBG during polishing. (b) Some simulated spectrum used to match the measured spectrum in (c). (c) Picture of the oscilloscope display showing a measured spectrum while the pFBG is under polished.

Secondly, the existence of the outer air layer breaks the symmetry of the spectrum. This effect becomes more visible as part of the first Bragg mirror is polished away (Figure 4.18). Third, as the first Bragg mirror is polished away, the visibility of the resonant dip reduces quickly and almost disappear when the spacer length is less than 500 µm (Figure 4.19). This can be easily understood by the deterioration of the mirror reflectivity, which degrades the light confinement capability as being described in Section 4.2.3.

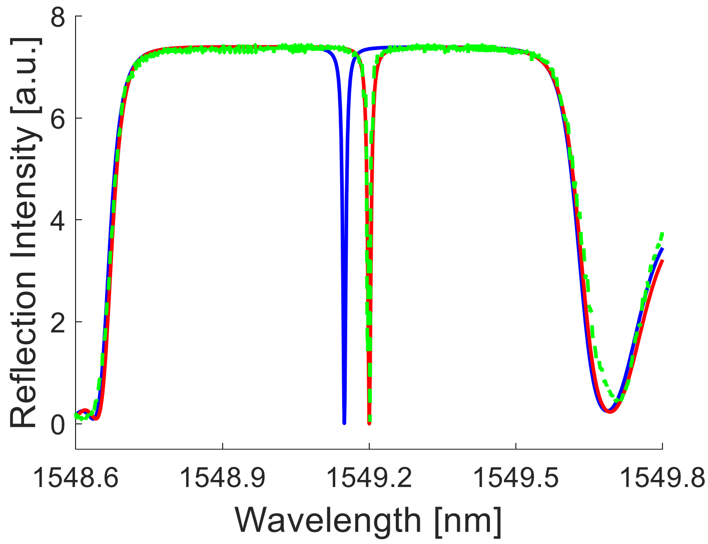

Figure 4.17 - Resonant notch position in simulation versus in reality. For an ideal pFBG (blue solid curve), the length of the cavity corresponds to exactly a phase shift of pi radian for the design wavelength of the Bragg grating, resulting in a resonant notch locating at the center of the stop band. However, due to manufacturing tolerance, real pFBG (green dashed curve) has its resonant frequency slightly shifted from the center of the stop band. A small modification in the length of the cavity was then added to the ideal pFBG to make the simulated pFBG (red solid line) match perfectly with the real pFBG.

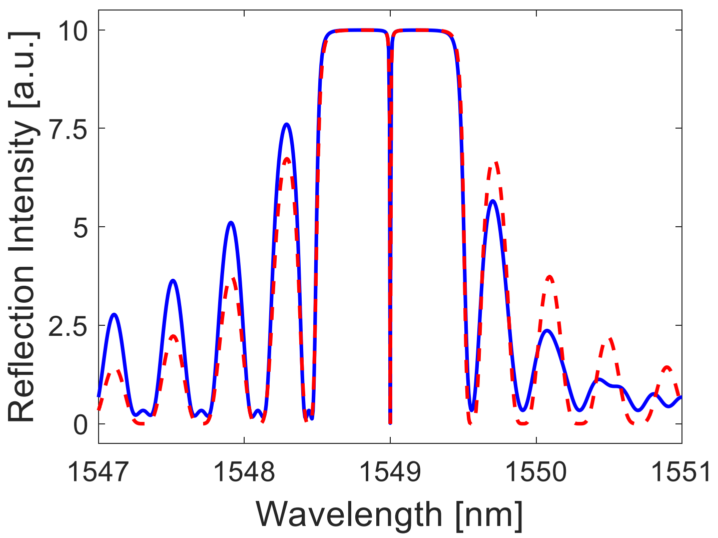

Figure 4.18 - Simulated spectrum with (blue solid curve) and without (red dashed curve) the outer air layer. Without adding the outer air layer into the TMM, the spectrum of the pFBG is perfectly symmetrical around its resonance frequency. The outer air layer breaks the symmetry of the simulated spectrum, which is necessary to match the experimental spectrum.

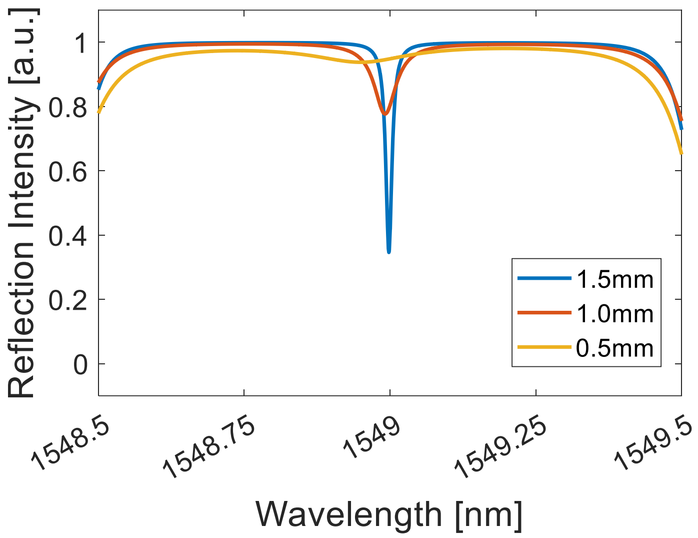

Figure 4.19 - Simulated resonant notch upon polishing to reduce the length L_1 of the first grating (or the spacer). The notch is almost disappeared as L_1 getting below 500 µm.

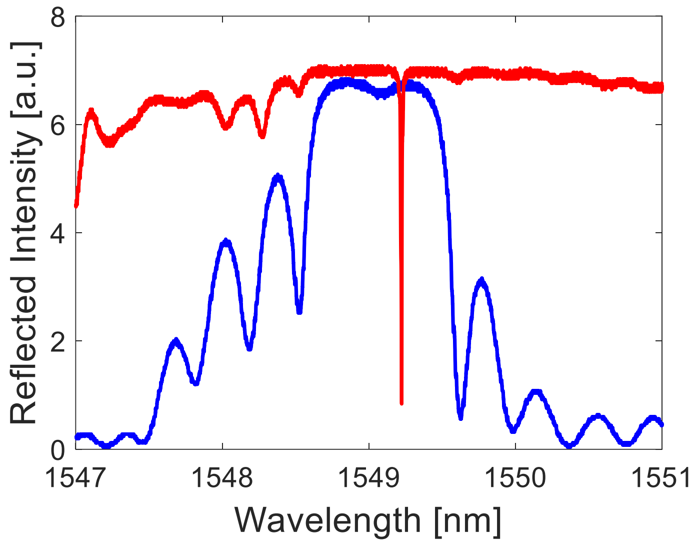

Figure 4.20 - The spectrum of an EER before (blue curve) and after (red curve) coating the polished tip with a silver mirror. The coating boosts the reflectivity of the first mirror and recovers the presence of the resonant notch at approximately 1549.2 nm.

After reaching a desired spacer length, the tip of the SOF is finely polished with diamond lapping sheet of 0.02 µm grid (LFCF, Thorlabs Inc., USA). The polished tip is then coated by a silver mirror using wet-chemical methods similarly to the SWED. The reflected spectrum of an EER is exhibited in Figure 4.20. Because the silver mirror is highly reflective over a broad-spectrum range, the characteristic stop band of the Bragg grating is not visible. However, a resonant notch appears at approximately the same location as that of the original pi-shifted cavity.

A very important task of fabricating the EER is to determine the precision of the spectrum matching method. Figure 4.21 illustrates the good agreement of the simulated and experimental spectrums of the EER prior to silver coating with different spacer length. The spectrum matching method allowed us to distinguish clearly polishing states with spacer length difference of > 200 µm. However, the major concern is what the smallest spacer length difference that can be determined, for example if the difference in the spectrum of the EER with spacer lengths of 100 and 120 µm can be observed. Up to our knowledge, there is no current method that is capable of measuring such spacer length of a FBG for using as reference, the precision of the spectrum matching method was then determined by intentionally over-polishing. Several pFBG were polished very slowly while recording spectrum and coated with silver just after a few seconds of polishing. If the resonant notch appears after silver coating, the pi-shifted cavity remains untouched. As soon as the resonant notch does not appear after silver coating, the pi-shifted cavity is polished and the process was stopped immediately. The silver coating was then removed by slightly rubbing the coated tip with the lapping film and the spectrum of the fiber was recorded. This spectrum was assigned as the reference spectrum with spacer length of 0. We removed completely the spacers of several pFBGs using this method and observed that the spectrum matching method cannot indicate the correct spacer length as it got smaller than 50 – 70 µm (depending on each fiber). So, it is reasonable to state that the resolution in spacer length of the spectrum matching method is below 70 µm for the chosen grating strength. We therefore do not attempt to produce EER detectors with spacer of less than 70 µm.

4.4.3 Sensor characterization

a) Optical characterization

After fabrication, we first measured the Q-factor of the EER detectors. The swept tunable laser was swept over the resonant frequency of approximately 1549 nm while interrogating into the EERs. For optical resonator with sufficiently high Q-factor, the Q can be estimated as expressed in Equation 3.2.11. The Q values of the EERs with different spacer length are given in Table 4.1.

The first mirror of the EER structure comprise of the spacer and the metallic mirror, so the total reflectivity of this first mirror is the combination of the reflectivity of its components. We used the TMM method to assert the change in reflectivity of the spacer and the first mirror versus spacer length, as mentioned in Section 4.2.3. Figure 4.22 illustrates the change in reflectivity of the spacer and the first mirror, assuming the reflectivity of the metallic mirror remains unchanged at 95%.

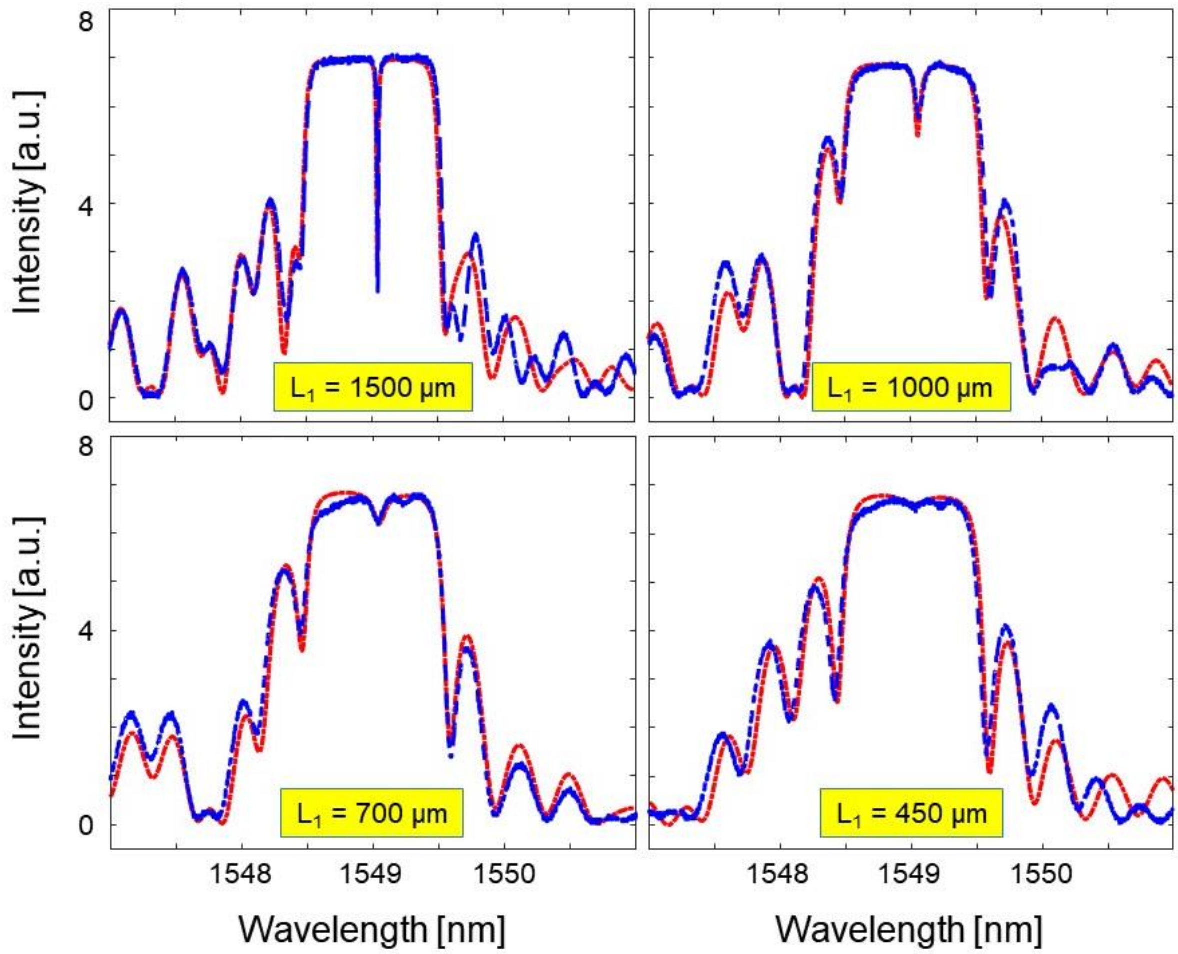

Figure 4.21 - Simulated and experimental spectrums of several EERs with different spacer lengths. The value of the spacer length L_1 is stated in the corresponding figure.

Table 4.1 - Q-factor and spacer reflectivity of the EER with different spacer lengths

L_1 [μm]	1500	1250	1000	700	450	150	70
Q-factor	4.84×10^5	4.84×10^5	3.69×10^5	1.72×10^5	1.11×10^5	7.38×10^4	6.45×10^4
R_{spacer} [%]	94.50	89.14	79.13	57.60	31.82	4.40	0.98

b) Optoacoustic characterization

A – Characterization of the interaction between optical and ultrasound fields in the EERs

Since one of our major hypotheses of using the hpBG design is the proximity of the cavity with respect to the sensing facet was predicted to improve the detection sensitivity. For the SWED, there are two main reasons that this hypothesis cannot be verified explicitly:

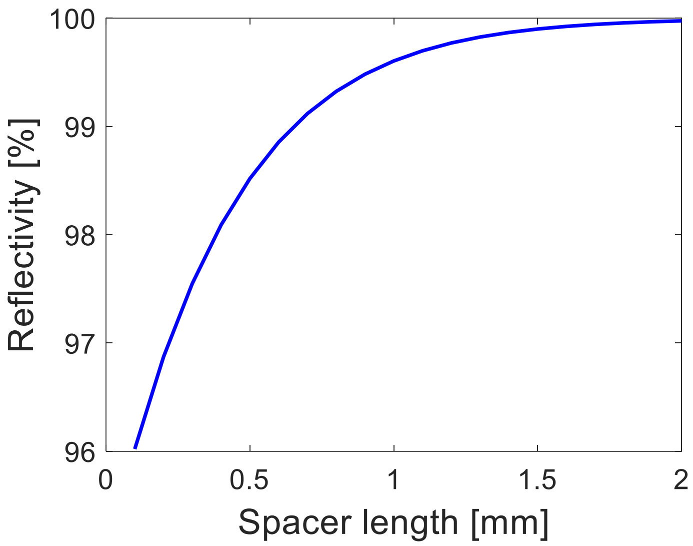

Figure 4.22 - Reflectivity of the fist mirror with 95%-reflectivity-silver-coating as a function of the spacer length.

- The strong grating strength of the Bragg gratings in silicon waveguides, while benefiting their miniaturization capability, making the total length of the grating section on the order of acoustic wavelength at hundreds of MHz in frequency. The different in spacer length between different SWEDs can only be on the order of 10 μm, which is much smaller than the acoustic wavelengths of the sensitive bandwidth. This scale different makes the interaction of light and ultrasound in the SWEDs become a sub-wavelength phenomenon and be difficult to analyse.

- The variation of spacer length in the SWED induces different spectral response as the frequency with strongest response is strongly related to the spacer with length on the order of sub-acoustic wavelengths. This behaviour accidentally makes the direct comparison of SWED with different spacer length difficult.

The EER has its structure spread over millimeter scale over the axis of the optical fiber. The spacer length difference between the EERs could be several hundreds of micrometers, which is much larger than acoustic wavelengths in silica. Furthermore, as will be shown later in this section, the bandwidth response of the EERs almost does not change with spacer length. This similarity allows direct comparison between behaviors of different EERs.

To validate the hypothesis, we first used simulation to calculate the change in optical intensity exposed at the sensing facet. Using the pure TMM approach, we simulated the optical intensity distribution inside the EERs while varying their spacer length. As can be seen from Figure 4.23, the shorter the spacer length, the brighter the tip of the EERs, which means the ratio between the optical energy located at the sensing facet and the amount of optical energy confined in the pi-shifted cavity is higher.

However, as the Q-factor of the EERs reduces with respect to spacer length, its maximum optical intensity at the cavity also reduces. We compensated this effect of Q-factor reduction by normalized the optical intensity at the tip of the EER with Q-factor. The result of the Q-normalized optical intensity at the tip of the EERs with respect to spacer length is depicted in Figure 4.24.

Next, we experimentally characterized the response of the EERs under constant optoacoustic excitation using the setup in **Appendix C**. The optoacoustic response of three EERs in time-domain with spacer lengths of 1.5 mm, 1mm and 0.45 mm are exhibited in Figure 4.25. It is observed that the response signals are composed of two distinct signals. The location of the first signal in the time axis corresponds to the time ultrasound takes to propagate from the source to the sensing facet of the EERs in the coupling media (water, speed of sound of approximately 1500 m/s). Therefore, it is reasonable to say that the first signal arises from the interaction between ultrasound and the optical field locating at the sensing facet. This first signal is then called “interface signal”. The second signal has distance $\Delta\tau$ between itself and the first signal decrease as the spacer length decreases. More importantly, $\Delta\tau$ corresponds to the time ultrasound takes to propagate from the sensing facet of the EERs to the pi-shifted cavity in optical fiber (made from silica, longitudinal speed of sound of approximately 6000 m/s [155]). This second signal is then corresponded to the interaction between longitudinal ultrasound propagating along the fiber and the strong optical field locating at the pi-shifted cavity, and called "bulk signal".

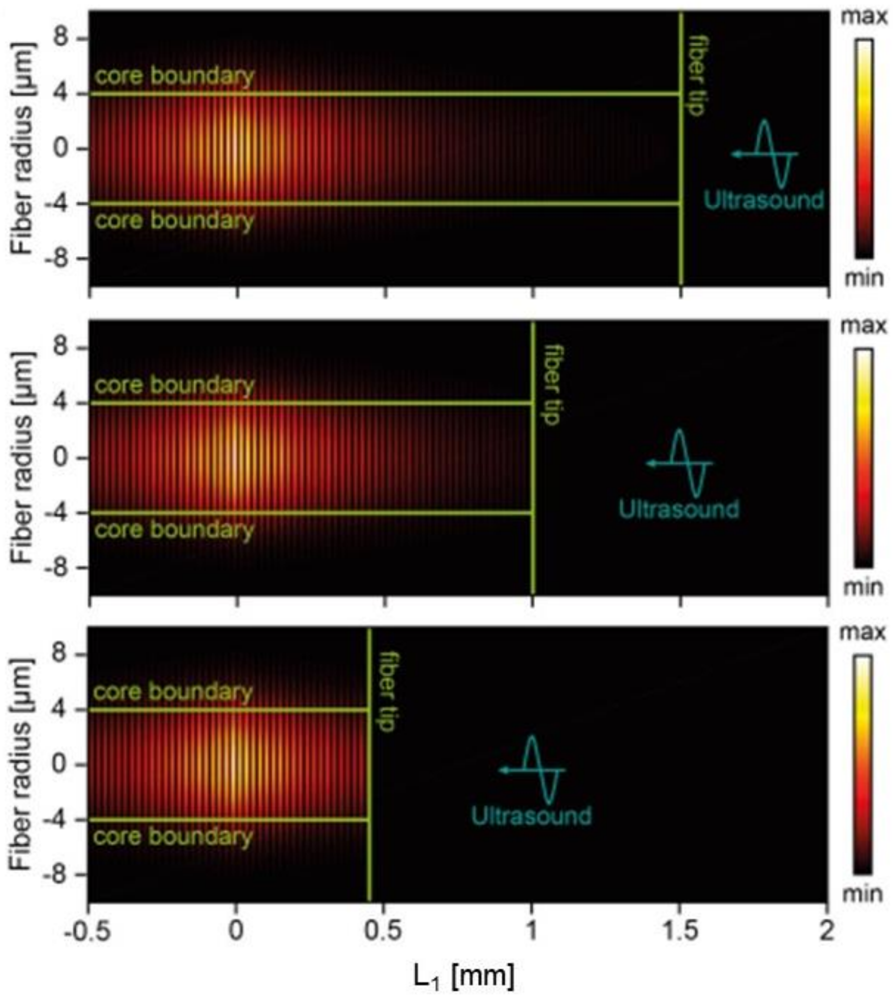

Figure 4.23 – Optical intensity distributions inside 3 EERs with different spacer lengths: (top) 1.5 mm, (middle) 1 mm, (bottom) 0.5 mm.

By looking at the frequency content of these two parts (Figure 4.26), we could further elaborate about their physical origins. The bulk signal has its peak response locating at around 8.4 MHz and its bandwidth extending until 19 MHz. This frequency content corresponds to a sensing length of approximately 600 µm around the pi-shifted cavity, in which > 50% of the optical energy is confined. This sensing length is called "effective sensing region" [154]. The interface signal has its -6dB bandwidth extending over 180 MHz with peak response at approximately

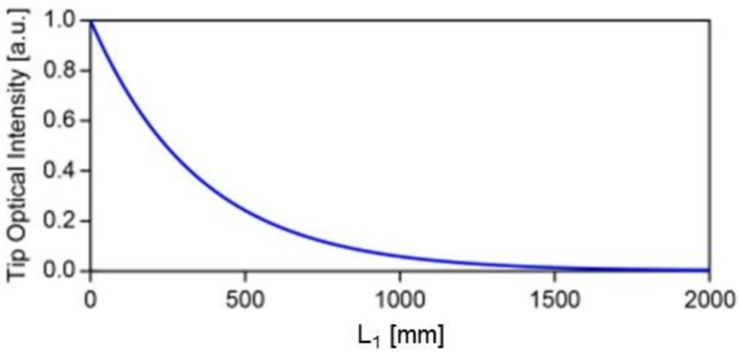

Figure 4.24 - Q-normalized optical intensity at the tip of the EERs with respect to spacer length.

11.5 MHz. This peak response suggests the primary contribution of the interface signal is from the fundamental shear wave that spreads from the core and is reflected back at the boundary between the cladding and the ultrasound coupling media (water). However, a detail study on how the interaction between ultrasound and the EERs at its tip governs the frequency response of the interface signal should further be investigated.

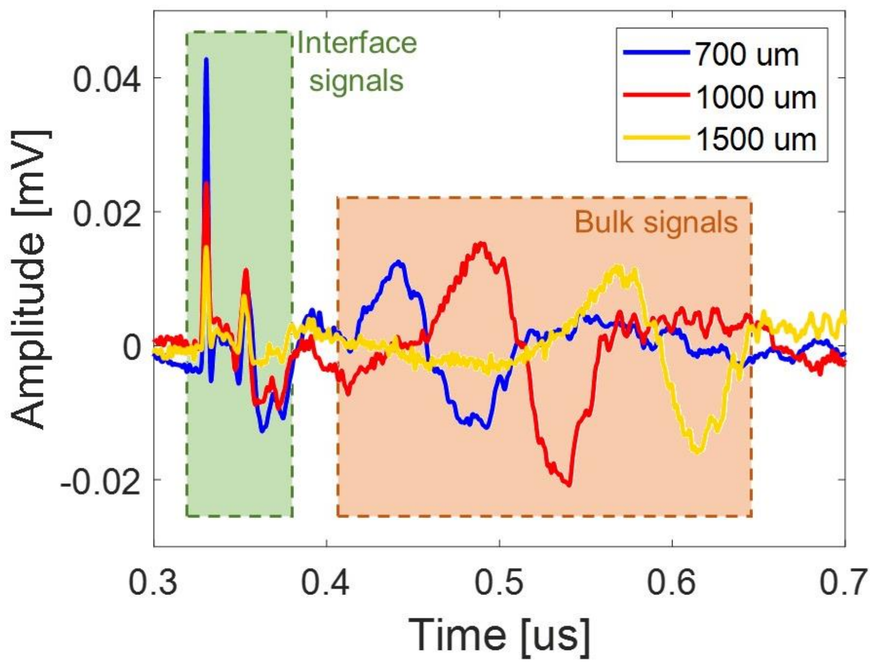

Figure 4.25 - Time domain response of EERs with different spacer lengths. The EERs were aligned so that the distance between the point source and its detection surface is fixed at 0.5 mm. The interface signals generated at the detection surface appear at the exact time position that corresponds to the propagation time of sound across the distance of 0.5 mm. The distance between the interface and bulk signal varies as the spacer length is changing.

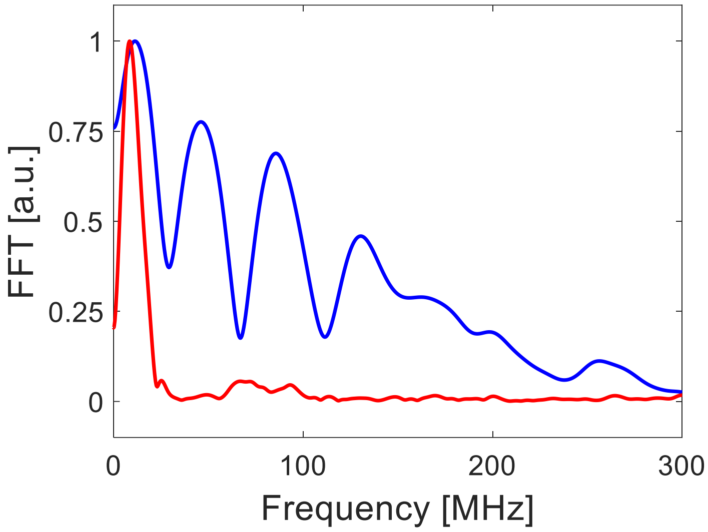

Figure 4.26 - Frequency response of the interface and bulk signals. Red curve: bulk signal. Blue curve: interface signal.

The separation Δτ between the interface and bulk signals decreases as the space length of the EER decreases. These two signals start to overlap when the spacer length getting smaller than 700 µm. However, while the amplitude of the bulk signal remains almost unchanged with varied spacer length, the amplitude of the interface signal increases significantly with reducing spacer length. At short spacer length, the interface signal dominates the overall response of the EERs. If our hypothesis is true, the experimental Q-normalized amplitude of the response of the interface signals of the EERs with respect to spacer length would closely follow the curve plotted in Figure 4.24. To experimentally validate the hypothesis, we measure the response of the EERs with different spacer lengths under the same optoacoustic excitation source. The relative sensitivity and the sensitivity after dividing to the detector's Q-factor (as listed in Table 4.1) are illustrated in Figure 4.27. The Q-normalized sensitivity of the EERs with respect to their spacer length closely follow the expected curve, which proves that the strong optical intensity at the detection facet benefits the overall sensitivity.

The spectral response of the EER with 70-µm-spacer length is plotted in Figure 4.28. Also, it was found that the bandwidth of the EER slightly decreases with reducing the spacer length. This is straight-forward from the analysis of the interface and bulk signal. At large spacer length, the low-frequency bulk signal can be truncated in time domain and does not interfere with the high-frequency interface signal. But as the spacer length decreases, the bulk signal overlaps more with the interface signal and thus its low frequency components contribute more to the overall response, thus reducing the bandwidth. Nevertheless, this bandwidth of > 136 MHz is still the largest bandwidth ever recorded for a fiber-based optical ultrasound sensor.

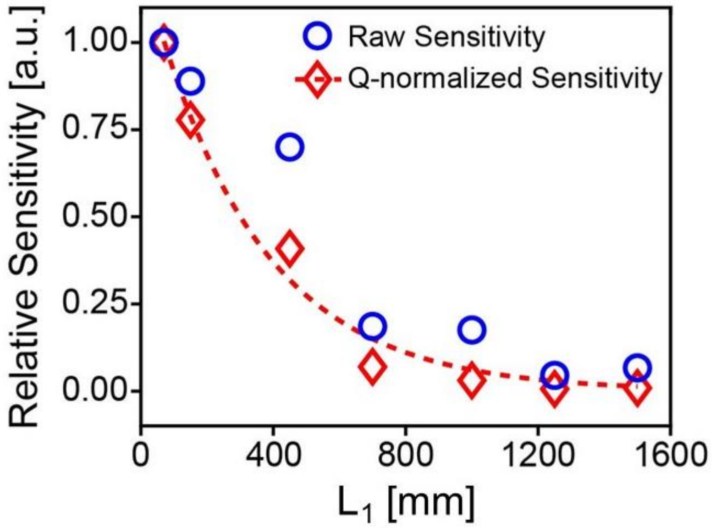

Figure 4.27 - Raw and Q-normalized optoacoustic sensitivity of the EER versus its spacer length.

B – Characterization of the ultrasonic sensitivity

As stated in Section 3.3, there is a strong correlation between the interrogation system, the sensor's power handling capability and its sensitivity. We first analysed systematically how these parameters could potentially affect the sensitivity of the EERs that we could achieve. We measured the optoacoustic responses of an EER while varying the laser interrogation power. We observed a linear relationship between the interrogation power, as expected from the literature [156] and Equation 3.3.6. It is worth mentioning that due to the relatively low threshold for nonlinear effect in silicon, nonlinear effects could be induced in silicon waveguide resonator at interrogation power on the order of 3-4 mW [105]. Such nonlinear effects are detrimental to the sensing characteristic because the shape of the resonant notch is distorted. Thanks to the extremely high-power handling capability and high threshold for nonlinear behaviour of silica, the EERs still operate in the linear regime until the maximum emission power of our laser. Indeed, it was demonstrated that SOF-based resonators could still stably operate in the linear regime with interrogation power of tens of mW [106,157]. The sensitivity that we were able to report here was practically limited by the emission power of our laser and could be further enhanced by using higher power lasers or optical power amplifiers.

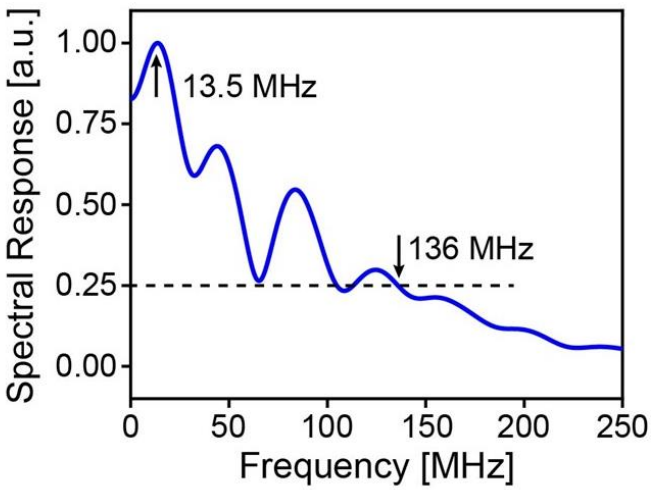

Figure 4.28 - Frequency response of the EER. The -6 dB bandwidth is 136 MHz. The peak frequency response locates at 13.5 MHz.

However, since NEP and NEPD are better options to evaluate the sensitivity, we also took into consideration the effect of the system's noise. The noise of the read-out optical signal composes of the noises from the laser, the photodetector and the data acquisition card, with the first one being the only one depending on the laser power [100]. As can be seen from Figure 4.29, the laser noise increases quickly with laser power and becomes the dominant noise source at high emission power. This noise behaviour of our interrogation system results in a saturation of the sensor's NEP at interrogation power above 5 mW despite of the linear increment of the sensitivity with respect to interrogation power. This NEP saturation highlights the importance of a good laser-noise behaviour, which could be achieved by a better laser or advanced read-out methods that help reducing the laser noise such as phase read-out [103], balance scheme [101] or pulse interrogation [100].

To characterize the absolute sensitivity of the EERs, we calibrated the response of the EERs with a needle hydrophone calibrated in the frequency range of 10 – 30 MHz (Precision Acoustics, UK) under the same ultrasound source with the calibration bandwidth. The experiment setup used to calibrate the sensitivity is similar to the system depicted in **Appendix D**. The only change in the setup is to replace the 200-nm-thick gold film by a 100-µm-thick black tape. The black tape has higher damaged threshold compared to the gold film, which allowing the increment of the focused laser power to generate a stronger optoacoustic signal.

In addition, the black tape generates optoacoustic signal that spans over the frequency range of 50-60 MHz, sufficiently covering the calibrated bandwidth of the needle hydrophone. We captured the optoacoustic responses from the EERs and the needle hydrophone from the same distance of 500 µm to the black tape without any averaging. The signals were then passed through a digital 10-30MHz band-pass filter. The response of the EERs with the highest sensitivity (spacer length of 70 µm) and the needle hydrophone are exhibited in Figure 4.30.

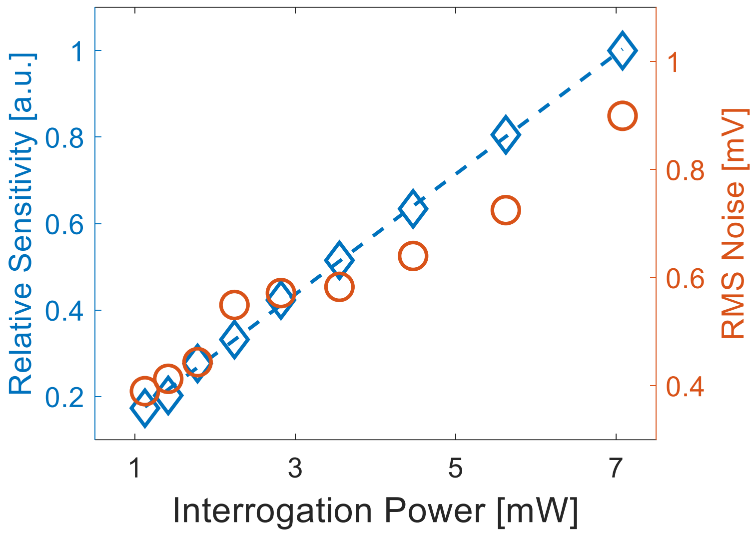

Figure 4.29 - Sensitivity and noise of the EER versus interrogation power. The sensitivity is linearly increasing with interrogation power, but the increment in noise saturates the maximum achievable NEP.

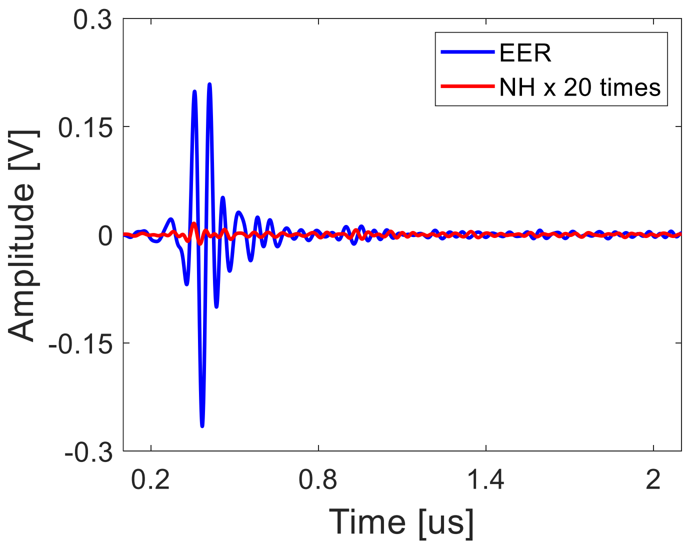

Figure 4.30 - Response of the EER and the needle hydrophone (NH) for calibration. The response of the hydrophone was enlarged by a factor of 20 for visualization.

For visualization purpose, the response of the needle hydrophone is enlarged by a factor of 20. The needle hydrophone was calibrated to have the sensitivity of approximately 440 mV/MPa in the frequency range of 10-30 MHz. With 9-dBm-interrogation power, the sensitivity of our EER was calculated to be 145 mV/kPa over the same 20-MHz-wide band, which is almost three orders of magnitude higher than the needle hydrophone. The root-mean-square value of the noise from the interrogation system was measured by recording the sensor's response under no optoacoustic excitation and had the value of approximately 1.78 mV. The NEP of the EER over the 10-30 MHz frequency range is 12.4 Pa, which corresponds to a NEPD value of 2.7 mPa/√Hz.

C – Characterization of the acceptance angle

Acceptance angle represents the ability of a sensor to collect signals from oblique incident angles. A wider acceptance angle means the sensor is able to capture oblique signals with less sensitivity deterioration. The acceptance angle of the EERs is characterized by line-scanning the detector over the optoacoustic point source, similar to the resolution characterization. We then determined the location of the -6 dB cut-off with respect to the maximum signal amplitude – which corresponds to the position where the detector is on top of the optoacoustic point source (Figure 4.31). The cut-off positions are located at the scanning position of ± 0.7 mm away from the optoacoustic point source, resulting in an acceptance angle of approximately 100^0. This acceptance angle corresponds to a numerical aperture (NA) of 0.77. In comparison to the SWED, the EERs possess a smaller acceptance angle, owing to the larger mode field diameter in optical fiber compared to silicon waveguides.

D – Characterization of the point-spread-function

The PSF of the EER is characterized in a similar way to the PSF characterization of the SWED over the same depth range (**Appendix E**). Because of a smaller acceptance angle compared to that of the SWED, the EER requires the scanning length of approximately 2.5 times the imaging distance to sufficiently cover its acceptance angle – which is affordable by our characterization system.

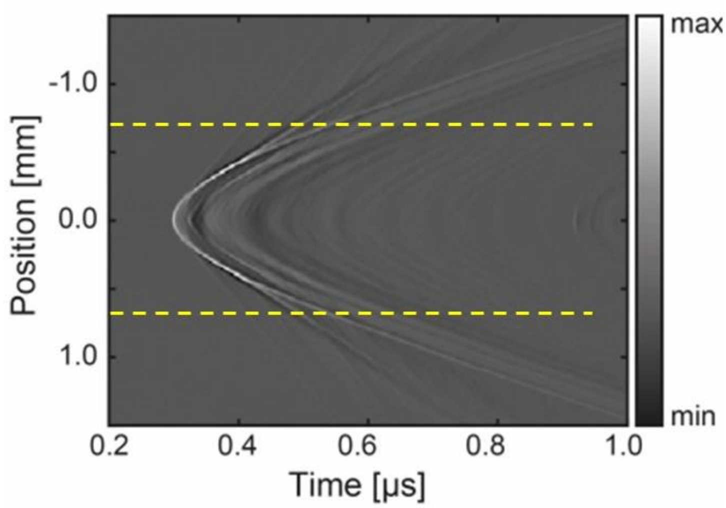

Figure 4.31 - Characterization of the acceptance angle. The dashed yellow lines correspond to the position where the response of the EER drops to 25% of its peak value at position 0.

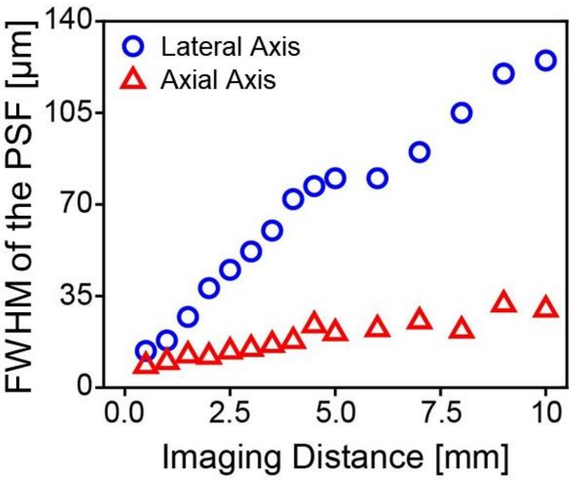

Figure 4.32 - Full-width-half-maximums of the point spread function with respect to imaging distance. The axial PSF deteriorates slowly from 7 µm to 30 µm as distance increase from 0.25 to 10 mm. The lateral PSF deteriorates at a much faster rate, from 12 µm to 120 µm over the same depth range.

Figure 4.32 shows the FWHM of the PSF of the EER in both lateral and axial direction with respect to the imaging distance. In comparison with the SWED, the EER has its PSF spreading more in the axial dimensions, which is partially due to the slightly narrower bandwidth. At imaging distance of 0.5 mm, the FWHM of the PSF in the axial direction is 8.5 µm – which is very close to the estimated value of 8 µm (calculated from Equation 2.3.3 using the characterized bandwidth). However, the axial FWHM of the PSF of the EER deteriorates at a much faster rate than that of the SWED, to approximately 30 µm at imaging distance of 10 mm. This can be explained by the difference in the bandwidth profiles of the two sensors. The

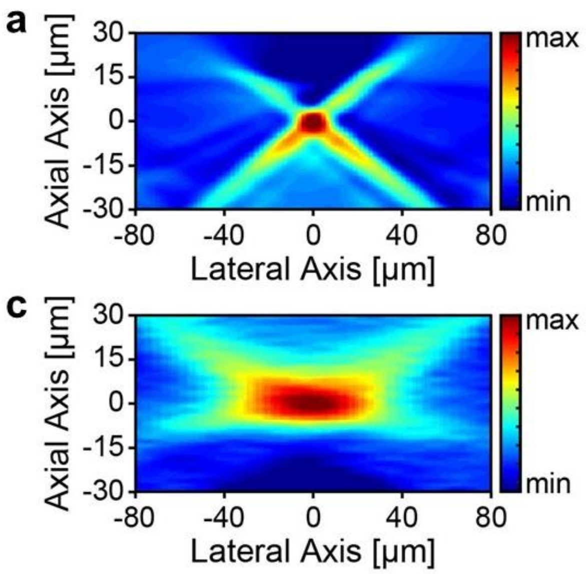

Figure 4.33 - Some reconstructed point spread function of the EER at different imaging distances. The PSF does not converge perfectly into a circle but has elongated diagonal artifact due to the existence of edge diffractive waves in the line scan data, which originates from the tip edge and propagating with different speed of sounds from the main longitudinal wave.

SWED characterized in Section 4.3.2 has peak frequency as high as 88 MHz and a relatively broad bandwidth response. The EER has its peak frequency at ~13 MHz, and is much more sensitive in the 0-50 MHz frequency range than it is in the > 50 MHz frequency range. With increasing the imaging distance, the acoustic attenuation starts to kick-in and reduce the content of the high-frequency components emitted from the optoacoustic point source. Therefore, the "effective bandwidth" – which combines the spectral response of the sensor upon an ideal point source and the spectrum of the actual optoacoustic signal that reaches the sensor – of the EER reduces at a faster rate with respect to imaging distance than that of the SWED.

On the other hand, the lateral FWHM of the PSF of the EER does not fall far behind that of the SWED. This observation is counter-intuitive for two reasons. First, the bandwidth and the lateral FWHM of the PSF of the EER is worse than those of the SWED. Second, the detection aperture of the EER is more than an order of magnitude larger than that of the SWED, which would be expected to further deteriorate the lateral PSF. However, as being analysed in Section 4.3.2, the lateral PSF of the SWED is deteriorated from its theoretically predicted value due to the existence of the SAWs – which propagating with different speed of sound and cannot be well converged into an ideal point source with longitudinal waves propagating in water. The EER seems to be negligibly affected by the SAWs, since the characterized PSF at imaging distance of 0.5 mm possesses a lateral FWHM of 14 µm – which is very close to the theoretically estimated value of 13 µm. This negligible lateral smearing effect imparts a more resilient behaviour toward SAWs of the EER compared to the SWED, which can be attributed to several factors. First, the SAWs generated at the detection surface of the EER is weaker than the SAWs generated at the detection surface of the SWED. As can be seen from Figure 4.34, at the position that the SAWs are started to be generated in the SWED, the overall optoacoustic signal experienced a boost in amplitude, indicating that the amplitude of the SAWs is much larger than the longitudinal wave. In contrast, the optoacoustic signal obtained from the EER does not show any remarkable difference as the SAWs are generated. This reduction in SAWs amplitude in the EER compared to the SWED is due to the smaller overall detection surface. The total detection surface of the EER is tip surface of the fiber, which is a circle with 125-µm-diameter. The SWED has the sensing aperture of approximately 500 x 220 nm, but the overall detection surface is a rectangular with size of 3 x 0.8 mm – which is equal to the cross section of the photonics chip. The 200-fold-larger detection surface of the SWED compared to that of the EER creates more "room" for SAWs to be generated and thus inducing a significantly stronger SAWs. Second, the SAWs in the EERs appear further away from the center of the line scan, thus reducing their contribution in the line scan data. This is explained by the SAW's speed of sound in silica (approximately 3700 m/s [158]) imparts the critical angle for SAWs generation of 28°, which is 1.6 times larger than this angle in silicon [143]. Finally, since the SAW's speed of sound in the EER is closer to speed of sound in water than SAW's speed of sound in the SWED, SAWs in the EER converge better when back projected using speed of sound in water, resulting in a weaker blurring effect.

A noticeable feature in the PSF of the EER is the faster deterioration rate in the lateral direction compared to that rate in the axial direction. It is suggested from Equation 2.3.3 that the deterioration of the lateral PSF must be attributed to some deterioration in the detection aperture other than just bandwidth deterioration. While this aperture deterioration seems counter-intuitive because the actual sensing aperture remains unchanged (which is equal to the mode field diameter of the fiber), it is physically possible once considering the "effective aperture" – the actual aperture which is limited by oversampling in spatial domain [159].

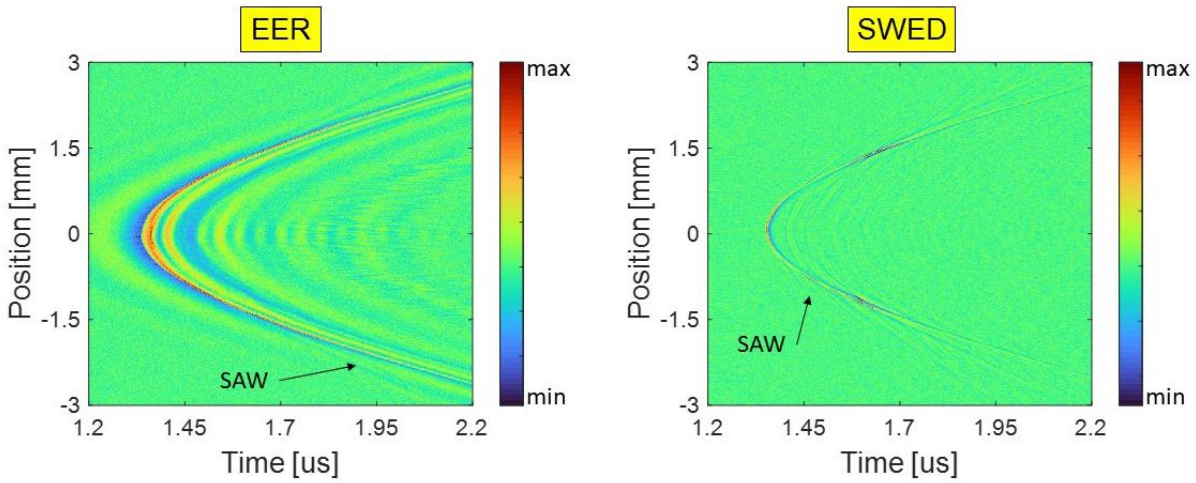

Figure 4.34 - Effect of surface acoustic wave (SAW) on the lateral smearing of the EER and the SWED. Both line scans are taken at distance of 2 mm. The line scan of the EER does not possess remarkable difference as the SAW is generated, while the line scan of the SWED shows a huge boost in signal amplitude.

4.4.4 Optoacoustic Imaging with the EER

To test the EER's capability of producing biomedical image, we conducted RSOM experiments using the configuration depicted in Figure 4.35. Herein, the nanosecond laser was coupled to a multimode fiber (MMF) with core diameter of 200 µm and cladding diameter of 225 µm (FP200ERT, Thorlabs Inc., USA). This excitation fiber was held parallel and next to the EER, forming a light-out/ sound-in probe with overall diameter of less than half a millimeter. The optical power exiting the excitation fiber measured by a laser power meter (S121C and PM100D, Thorlabs Inc., USA) was 3.9 mW. With an illumination spot of approximately 0.6 mm in diameter, the corresponding optical power exposure and optical energy exposure are 1.5 W/cm^2 and 1.2 mJ/cm^2, both of which are less than 10% of the ANSI limit [39]. Thus, no sample damage was observed after the imaging experiment. The sample was immobilized on top of a high-speed XY scanning stages (MLS203-1, Thorlabs Inc., USA) and raster-scanned during the imaging experiment. The top surface of the sample was kept at approximately 0.5 mm away from the detection surface of the EER. The emitted optoacoustic signals were collected by the EER, and 3D back projected in the frequency domain [145].

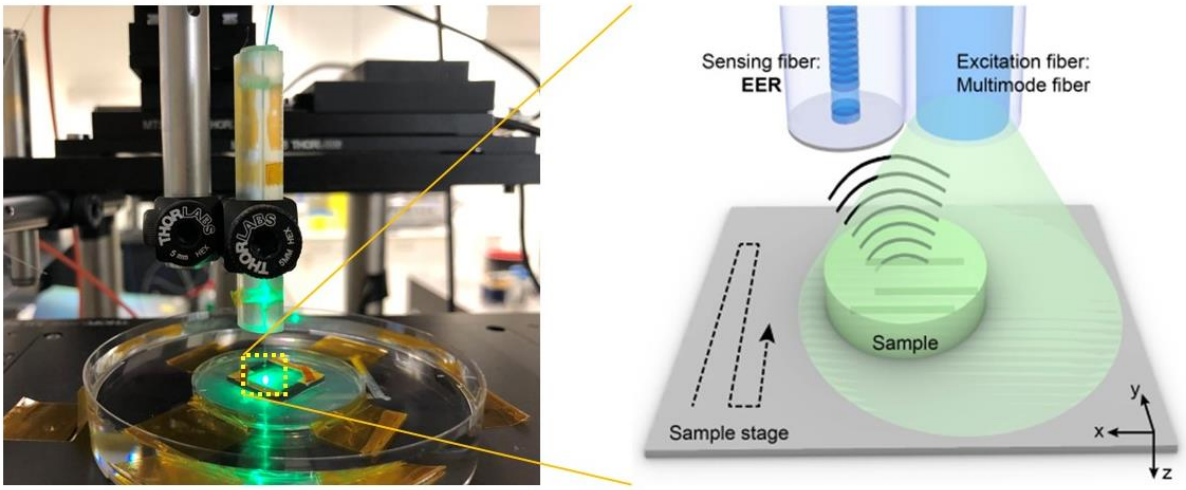

Figure 4.35 - Raster-scanning optoacoustic mesoscopy (RSOM) setup using optical fibers. One fiber was used for coupling of the excitation laser, the other (EER) was used for optoacoustic detection. The sample was raster scanned using a 2D microscope stage.

To test the capability of the EER in producing valuable information at large depth, we used the first sample, which is a controlled suture phantom comprising of 12 black sutures (Dafilon Polyamide, B. Braun Melsungen, Germany) embedded at various depth in a mixture of agal gel. The sutures had diameters ranging from 30 to 39 µm according to the specification from the manufacturer. The agal gel has the agar powder weight percent of approximately 2.5%, which created a mixture that resembles the acoustic properties of biological tissues. The black sutures were arranged into five different layers, each separated by approximately 1 mm. To prepare this controlled phantom, we first taped two sutures (layer 5^{th}) onto the bottom of a petri dish with Kapton tape. Then a plastic space with height of roughly 0.7 mm was taped on top of these two sutures with double-side tape. Three sutures were immobilized on this spacer with 90^{o} rotation in direction using Kapton tape. The process was repeated for upper layers with slight rotation of direction in each layer, until the 2^{nd} layer. Then, the liquid mixture of agar and water was poured into the petri dish so that the sutures on the 2^{nd} layer is dipped by approximately 0.5 mm under the liquid. The two sutures of the upper most layer is then dropped on the surface of the liquid solution. The petri dish was then stored in refrigerator for one hour to solidify the agar gel. A schematic explanation of the phantom preparation process and the top view optical microscopic image of the phantom is exhibited in Figure 4.36. Note that originally, all the suture was straightened before fixing using a tweezer, but once the agar liquid was poured into the petri dish, the high temperature of the liquid slightly relaxed the Kapton tape and bended the sutures in all XYZ directions, thus the spacing between layers was not fixed at 1 mm as designed. The two sutures on the 5th layer were also tangled together.

Figure 4.37 shows the maximum intensity projection (MIP) of the reconstructed 3D image of the controlled phantom using the EER probe. All the sutures of the five layers are visible, and the XZ and YZ views clearly shows the distribution of those sutures with depth. The quantitative analysis of the contrast and physical dimensions of several sutures are given in Figure 4.38a. Here, we observed a drop of approximately 12 dB in SNR across the five layers, which is attributed to the reduction in both the intensity of the optical illumination and the amplitude of the received optoacoustic signals with respected to imaging distance. About the suture dimensions, the axial diameter deteriorates from approximately 30 µm at imaging distance of 0.5 mm to approximately 160 µm at 4.5 mm, while the lateral diameter deteriorates from approximately 35 µm to approximately 250 µm over the same depth range. The deterioration rate of the suture dimensions is faster than the deterioration rate of the PSF with respect to imaging depth (Figure 4.32), which is attributed to several factors. First, because the scanning length of the sample remained fixed at 4 mm, the coverage angle reduces from 152^o for the first suture layer to 48^o for the fifth suture layer. This significant reduction of coverage angle strongly smears the spatial PSF, as being observed in the SWED. Next, the probe design had insufficient overlapping of the optical illumination and the ultrasound sensitive regions (Figure 4.38b), which inherently decreases the coverage angle. The NA of the illumination fiber is 0.5 while the NA of the EER is 0.77, making this effect more severe with increasing depth. Finally, within the detection bandwidth of the EER, the agar gel has larger acoustic absorption compared to water – the medium that we used to characterize the PSF, which leads to a reduction in the effective bandwidth and thus the PSF of the sensor.

To illustrate the suture imaging capability of the EER with sufficiently small step sizes and proper illumination, we imaged the cross sections of sutures of different sizes at imaging depth of around 500 µm with imaging step size of 1 µm and large illumination beam (approximately 2 mm in diameter) using the trans-illumination setup as depicted in Figure 4.39. The dimensions measured from the image are listed in Table 4.2. The cross section of the suture with diameter of approximately 40 µm is exhibited in Figure 4.39b. Because of the high optical absorption of black suture, light attenuates drastically as it penetrates into the suture, so the inner region emits weak optoacoustic signals and the edge is more visible than the center. This is the typical characteristic of optoacoustic imaging when the spatial resolution is several times smaller than the suture's diameter, i.e., in optoacoustic microscopy. When the suture's diameter is on the order of the spatial resolution, the cross section of the suture appears as a solid shape, which can be observed when imaging suture of 10 µm diameter with the EER (Figure 4.39c) or suture of 30 µm diameter with the optomechanics silicon detector [128] – which has theoretical resolution of approximately 30 µm.

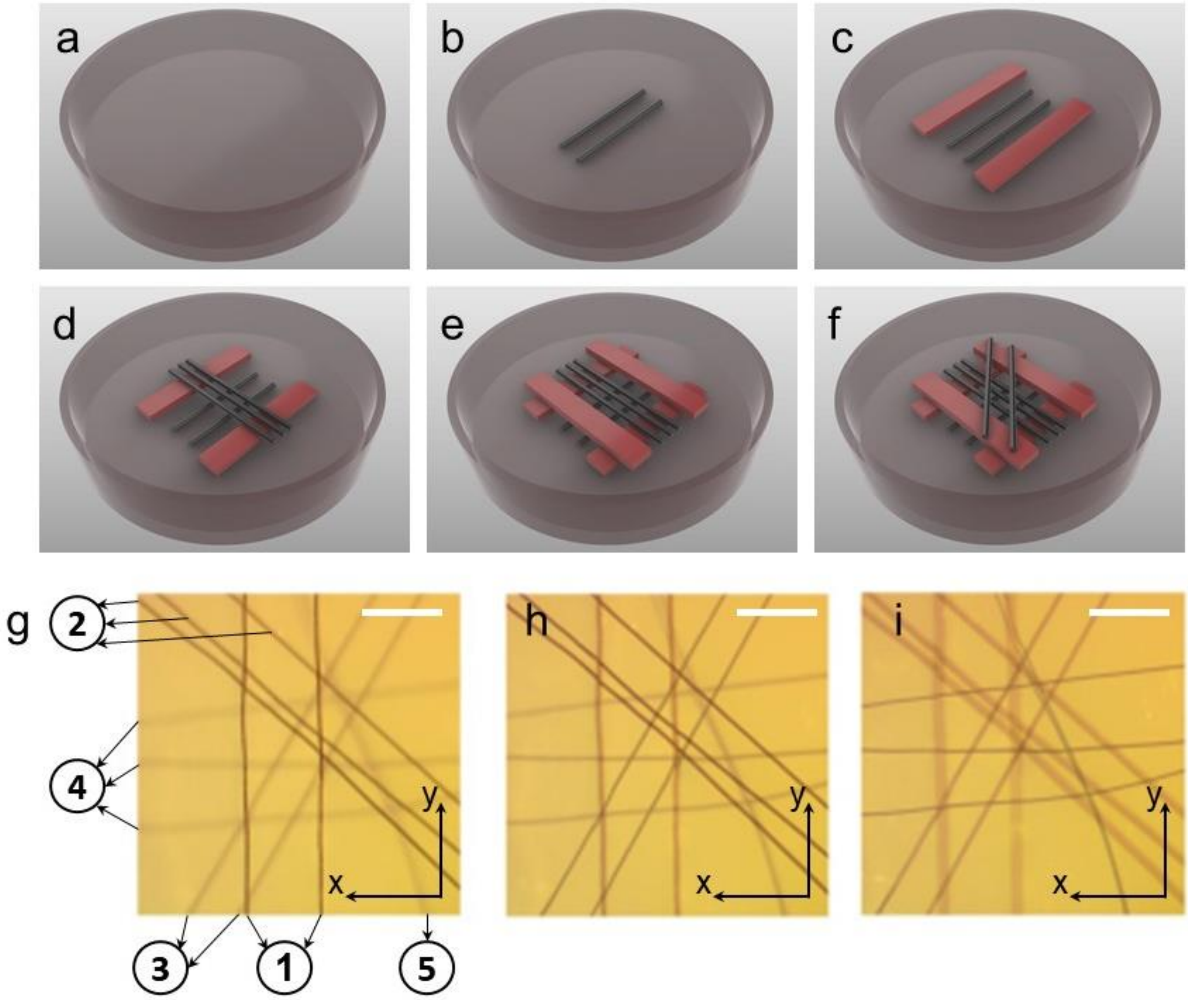

Figure 4.36 - Preparation of the controlled suture phantom. (a-f) Schematic of the preparation process. A petri dish was cleaned (a), the two sutures was immobilized onto the dish with tape (b). Next, two plastic spacers were glue onto the dish (c), and the next layer of suture was taped onto these two spacers (d). The process was repeated (e, f) for the next layer until 4 layers were obtained. The liquid agar was poured into the dish to submerge the top layer of approximately 0.5 mm. Then two sutures were dropped on the surface of the agar poured dish. The phantom is then cooled in 1 hour to solidify the agar. (g-i) Microscopic pictures of the phantom with optical focus on the first layer (g), third layer (h) and forth layer (i).

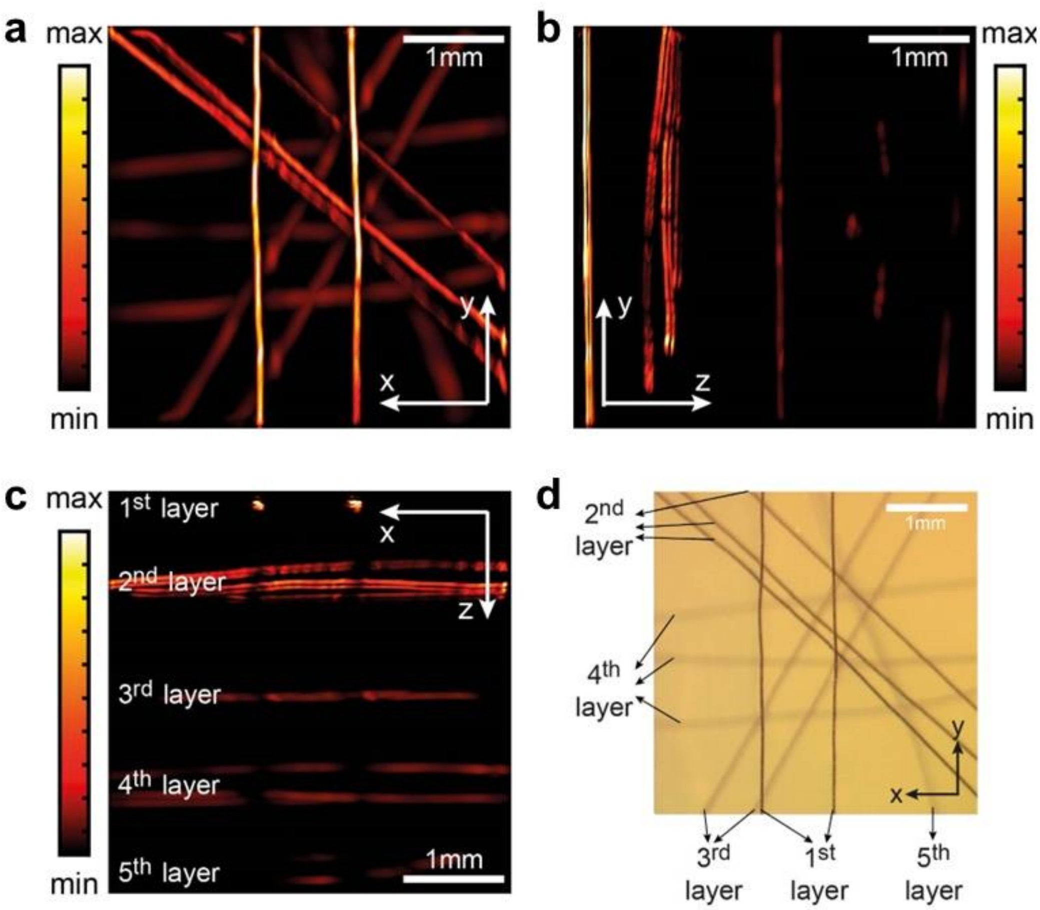

Figure 4.37 - RSOM images of the controlled suture phantom. (a-c) Maximum intensity projections (MIP) onto the XY plane (a), YZ plane (b) and XZ plane (c). (d) Microscope picture of the XY view for comparison. All the sutures from five layers are visible in the RSOM images.

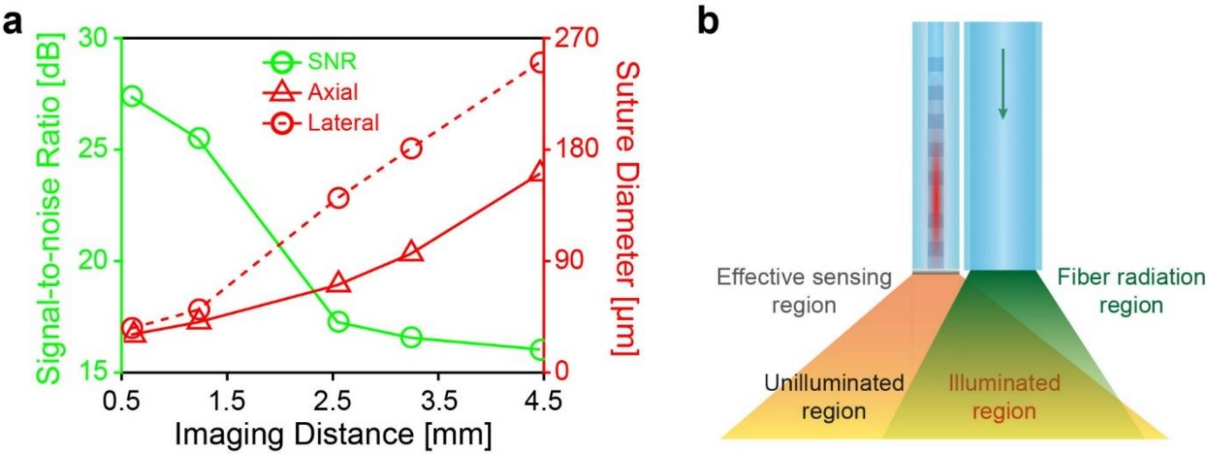

Figure 4.38 - Analysis of the RSOM image for the controlled suture phantom. (a) Size and visibility of sutures at different imaging depths. (b) Illustration of the insufficient coverage of the excitation fiber with the sensitivity field of the EER.

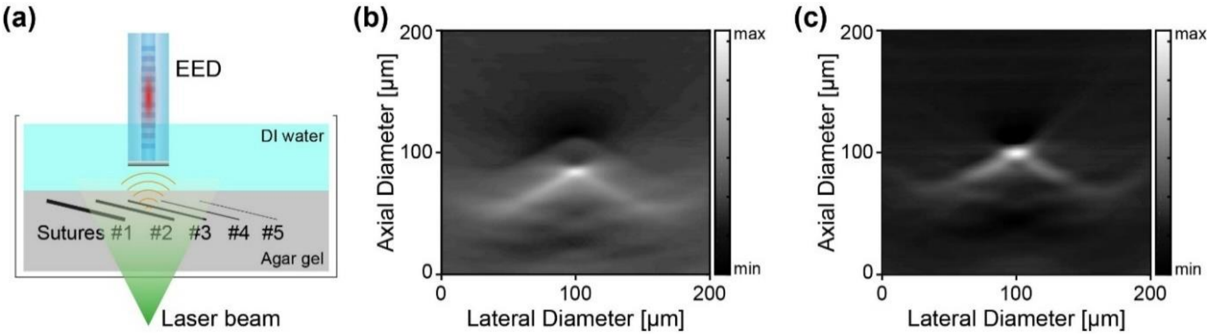

Figure 4.39 - 2D imaging of sutures with different sizes under proper illumination and sufficient spatial sampling. (a) Imaging setup, where the illumination laser is diffused to sufficiently cover the sensitivity field of the EER detector (EED). (b-c) Cross sections of the suture with diameter of approximately 40 µm (b) and 10 µm (c).

Table 4.2 - Imaging objects and their respective measured dimensions

Objects	Actual Diameter* [µm]	Measured Axial diameters [µm]	Measured Lateral diameters [µm]
Suture #1	100-150	112.5	117
Suture #2	40-49	41.5	46
Suture #3	30-39	30.5	33
Suture #4	20-29	28	30
Suture #5	10-19	11.5	19

* According to manufacturer's specifications

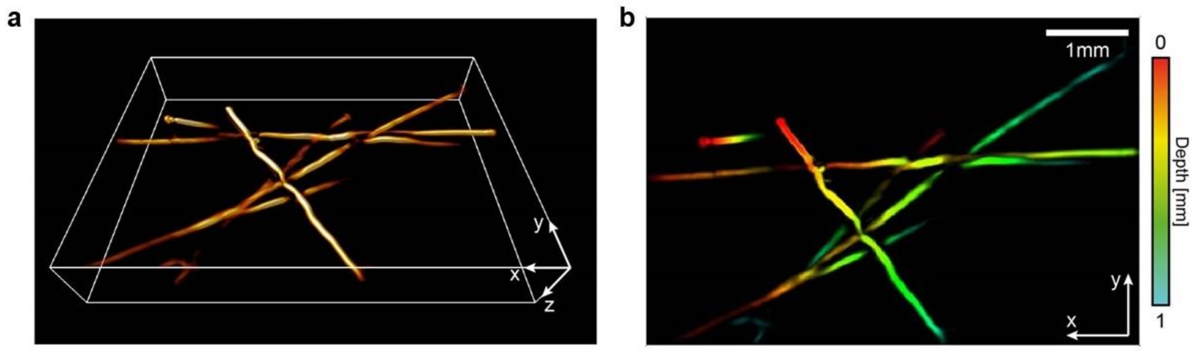

Figure 4.40 - RSOM image of the randomly-distributed suture phantom. (a) 3D rendering image. (b) Depth encoded image.

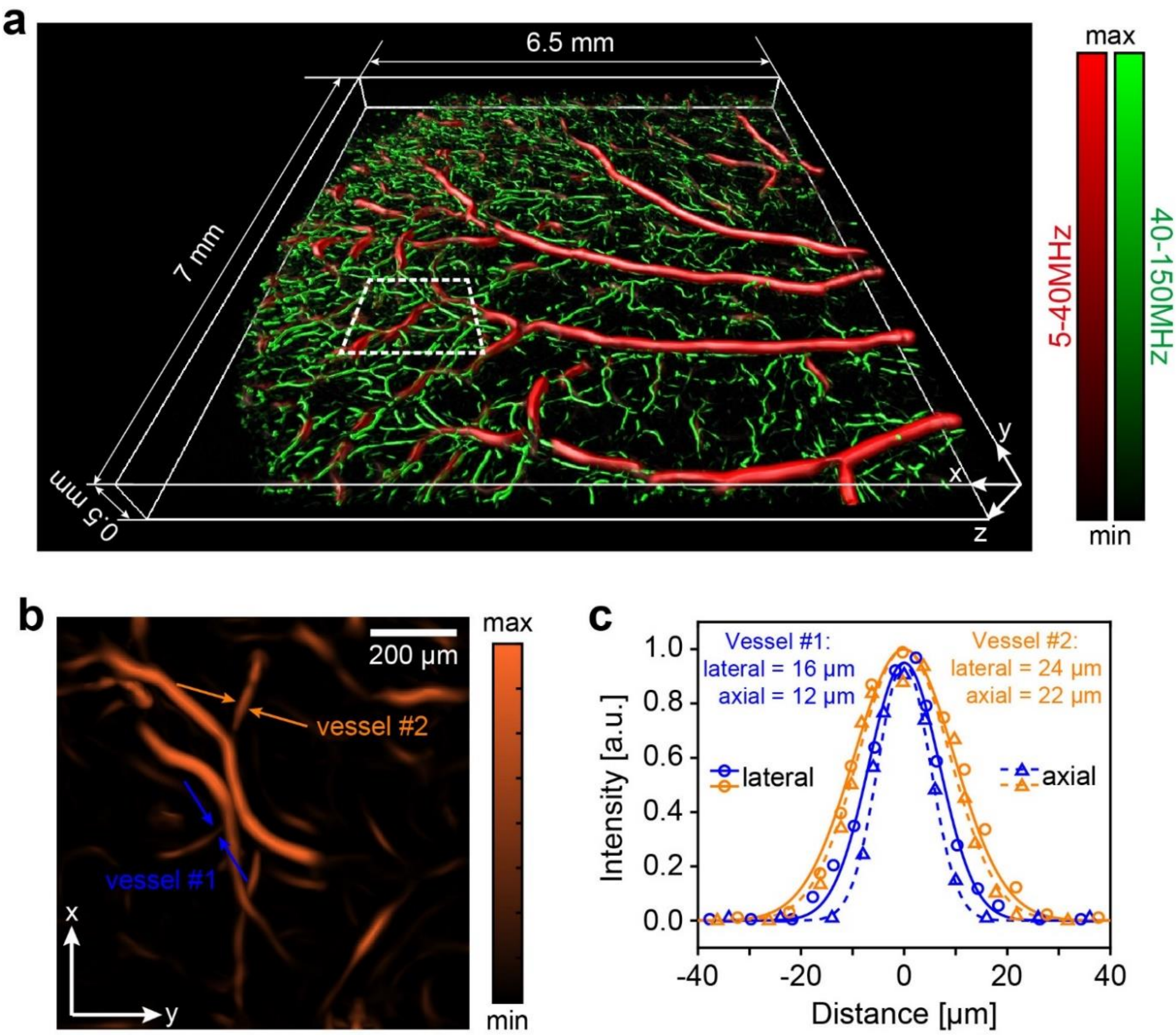

Figure 4.41 - RSOM image of the ex vivo mouse ear. (a) 3D rendering image with bandwidth-encoded colouring. (b) MIP of the section marked with dashed white square in (a) without bandwidth-encoded colouring. (c) Profiles of two vessels marked in (b).

The third sample is a randomly distributed suture phantom, used to test the imaging performance of the system with absorber of random orientation in 3D space. All the sutures had the same size as those used in the first phantom. The 3D rendered image of the reconstructed signal is displayed in Figure 4.40. Sutures of various length and orientation can be observed throughout the imaging volume.

To assert the imaging performance with a real biological sample, we continued to image the vascular structure of several ex vivo mouse ears, which are conventional samples for optoacoustic imaging due to the presence of absorbers (blood vessels) with various sizes and orientations. Figure 4.41 exhibits the reconstructed 3D image of several mouse ears. Thanks to the ultra-broad bandwidth, the EER was able to resolve micro-vessels with diameter ranging from hundreds of micrometers down to less than 20 micrometers.

4.5 Discussion

In this chapter, challenges with the state-of-the-art optical ultrasound sensors in reaching the resolution achieved by preclinical focused piezoelectric transducers was discussed and a new sensor design that could surpass this challenge was proposed. Theoretical tool based on TMM was used to predict the performance and help guiding the realization process. The design called hpBG was realized in the two most common photonics platforms: optical fiber and silicon photonics (which can be found in detail in other references [47,142,143]).

The successful realization of the hpBG sensor in optical fiber (the EER) marked for the first time an optical ultrasound sensor could provide both sensitivity and resolutions comparable to a focused piezoelectric transducer conventionally employed in optoacoustic mesoscopy. Moreover, the EER is small enough to fit in a clinical 3 French-sized endoscope, which has the outer diameter of 1 mm. This compact detector opens numerous opportunities that cannot be possible with millimeter-size piezoelectric transducers in guidance and diagnosis during minimal invasive procedures such as intravascular imaging, laparoscopy, or surgery endoscope.

The analysis provided in the chapter also paves the way for future developments, which could further improve clinical relevance of the EER in the following aspects:

Sensitivity

The sensitivity of the EER depends strongly on the Q-factor of the hybrid resonator, which could be enhanced by improving the reflectivity of the two mirrors. Both mirrors can have their reflectivity increased by increasing the grating strength, as the AC coupling coefficient is an arbitrary choice and can be surpassed. For the second mirror, increasing its grating length is also a possible solution to increase its sensitivity. For the first mirror, a better reflective coating assures a higher reflectivity. The silver coating used in this study was prepared by wet chemical precipitation with estimated reflectivity of around 95%. Professional metallic coating using sputtering method could provide metallic mirror with reflectivity of over 97%.

Spectral response

The EER revealed an important insight on how the spectral response depends mainly on the interaction of ultrasound wave and optical field at the tip of the fiber. This phenomenon suggests a method to alter the spectral response of the EER: to engineer the physical dimensions of the fiber at the tip region. Such modifications are possible by edge polishing the fiber while axially rotating as illustrated in Figure 4.42. By reducing the diameter of the fiber tip, the fundamental shear wave that is expected to govern the interface signal of the response is going to experience an increment in frequency, allowing us to tune the shape of the EER's frequency response. Because absorbers of different sizes emit optoacoustic signals of different frequencies, the frequency tunablity of the sensor enables size selectivity, in which the proper sensor with frequency response matches that of the desired absorber will be chosen to fit specific applications.

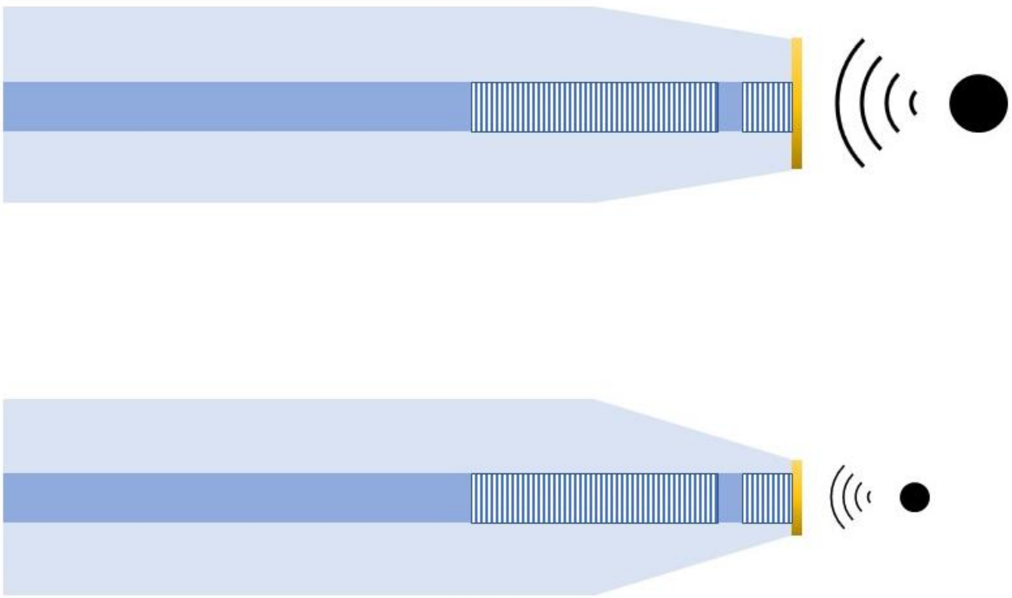

Figure 4.42 - Tip-engineered EER. By reducing the diameter of the tip of the EER, the frequency response can be tuned to maximize its sensitivity with different absorbers.

Resolution

By shifting the spectral response of the EER toward higher frequency using the mentioned conical tip method, both the axial and lateral resolutions of the EER will be improved.

Otherwise, it is possible to reduce the detection aperture of the sensor, which reduces the lateral smearing and produces a more isotropic spatial response of the sensor. The aperture reduction could be done by employing optical fibers with smaller mode field diameters. For example, the GF4A fiber has mode field diameter of only approximately 4 µm at 1550 nm. Assuming all the grating parameter remains the same, EER based on GF4A fiber would produce a near-isotropic spatial resolution of 8 x 9 µm in the axial and lateral directions, respectively. Another approach is to change the interrogation wavelength to the visible regime. Here, single mode fiber with mode field diameter down to less than 3 µm are available (for example, the SM400 optical fiber has mode field diameter of only 2.5 µm at 480 nm).

Through-sensor illumination

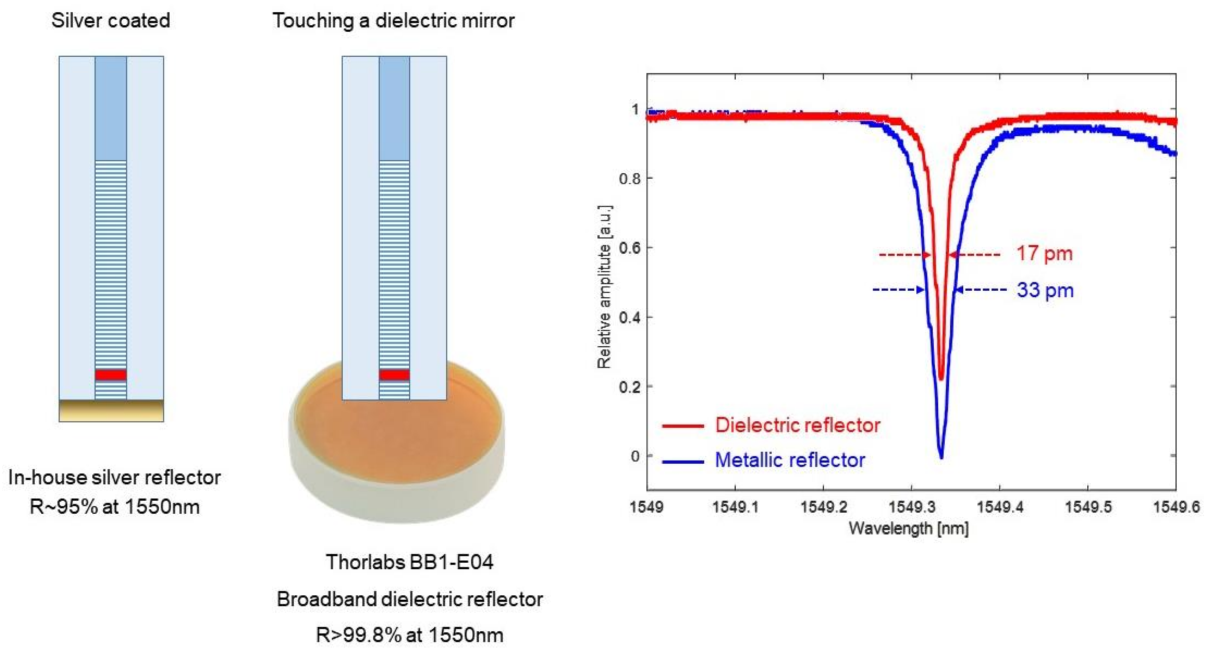

Figure 4.43 - Demonstration of the effect of the dielectric coating on the Q-factor of the EER. By applying a dichroic coating on the tip of the EER instead of a metallic coating, we observed a two-folds increment in Q-factor, suggesting a two-fold improvement in sensitivity.

A major advantage of the optical fiber compared to silicon photonics is the transparency over a wide spectral range, allowing the co-illumination via the same fiber used for sensor construction. For the current EER design, the metallic reflector prevents the through-sensor illumination, so we used a second fiber for demonstration of the imaging experiment. For future implementation, the metallic mirror could be replaced by a dichroic (dielectric) mirror, benefiting the sensor in two aspects. First, by the distinction of the sensor interrogation wavelengths and optical illumination wavelengths (for example, 1550 nm for interrogation and

532 nm for excitation), the dichroic mirror could be reflective for the interrogation wavelengths and transparent for excitation wavelengths [43]. By using the same fiber for both detection and excitation, the dimension of the probe reduces to only 125 µm, which enables investigation of never-before micro-vessels. In addition, the dichroic mirror could be applied to the tip of the fiber with very high reflectivity. By simulation, a 3.3-µm-thick dichroic mirror has reflectivity of > 98%, which is higher than the theoretical limit for a perfect metallic coating. This reflectivity enhancement also benefits the sensor's sensitivity. Indeed, we conducted a simple demonstration to show the effect of dielectric coating (Figure 4.43). Herein, we recorded the resonant dip of an EER with spacer length of approximately 200 µm. Next, we removed the metallic coating of this EER by gently polishing its tip on the finest lapping film. The, we placed this non-coated EER on top of a broad band dichroic reflector (BB1-E04, Thorlabs Inc, USA) so that the tip of the EER was perpendicular to the surface of the reflector, creating a pseudo-dichroic coating at the tip of the EER. The recorded resonant dip shows a two-fold reduction in linewidth (33 pm for the metallic-coated EER and 17 pm for the pseudo-dichroic-coated EER), which can be roughly translated to a two-fold improvement in sensitivity.

Chapter 5 : D-shape Fiber Bragg Grating for High Sensitivity Optoacoustic Sensing

5.1 Introduction

Ultrasound sensors using optical methods, especially optical resonators, offers a major advantage over piezoelectric transducers at size-constrained applications. The typical indicator for evaluating sensitivity with respect to size is the sensitivity per detection area, which has the unit of [mPa .$Hz^{-1/2}$ .mm^2]. Piezoelectric transducers have sensitivity per detection area ranging from several to several hundreds of mPa .$Hz^{-1/2}$ .mm^2, while optical resonator-based ultrasound sensors have sensitivity per detection area of at least two order of magnitude higher than that of piezoelectric transducers. A more comprehensive review of sensitivity per detection area of different types of ultrasound sensors can be found in other references [160].

However, the usage of the sensitivity per detection area often misleads to the interpretation of the true physical dimensions of the sensor – which are realistically important for applications that do not necessitate a dense array implementation. Therefore, it is worth mentioning that for milimeter-sized piezoelectric transducers, their co-packaged electronics for signal amplification are of the same size, so the overall packaging dimensions of piezoelectric transducers is not enlarged significantly from the size of the sensing elements (the piezoelectric crystals). The size-retaining property does not hold true for optical ultrasound sensors, whose associated packing components are often much larger than the sensing elements itself. For example, silicon photonics-based sensors or polymer microring-based sensors were fabricated in substrates with sizes on the order of milimeters, not even taken in to account the interconnect required to interrogate and read out the sensing elements [129,142]. Perhaps, the smallest size one can expected for optical ultrasound sensors is the size of a single mode fiber with diameter of 125 µm (could be smaller, depending on types of fiber used or mechanical work to reduce cladding dimension), as in the case of fiber-based Fabry-Perot [161], pFBG [112] or EER in the previous section.

Moreover, the absolute sensitivity is directly related to sensing threshold or image contrast, and is one of the most important parameters of an ultrasound sensor. Unfortunately, the sensitivity per detection area fails to indicate the absolute sensitivity of an optical ultrasound sensor, as its absolute sensitivity is generally independent of its size. Existing approaches to improve the absolute sensitivity of optical ultrasound sensors rely on either improving the Q-factor (see Section 3.3.2) or increasing the susceptibility with acoustical perturbation (see Section 3.3.3), and do not scale with increasing the size of the resonators. The only approach that scales reasonably well with size is membrane-based design [128,162] because a larger membrane collects more ultrasound, resulting in a stronger perturbation and higher sensitivity. However, this approach trades bandwidth for sensitivity, so a milimeter-sized membrane-based optical ultrasound sensor has frequency response similar to a capacitive micromachined ultrasound transducer (CMUS), which is unattractive for optoacoutics imaging and sensing due to the broad band nature of the optoacoustic signals. More importantly, membrane-based sensors can operate well only in water because their sensitivity collapses quickly in highly viscous coupling medium such as ultrasound gel, greatly confines their range of potential applications.

In this manner, it is trivial for piezoelectric transducer to achieve absolute sensitivity as small as < 1 mPa/√Hz, there is no current optical ultrasound sensors that could feature such sensitivity over an ultra-broad bandwidth of > 100 MHz stably regardless of coupling media and operation environments. In this chapter, a new optical ultrasound sensor is proposed to address these challenges. The principle of the new sensor exploits the phenomenon revealed in the previous chapter, wherein a better exposure of the confined optical field inside a resonator leads to sensitivity enhancement. However, in the EER design, the optical exposure and Q-factor are coupled, which means we could not increase one without reducing the other. The absolute sensitivity was not maximized because the EER with the shortest spacer length (highest sensitivity) has lowest Q-factor. The new sensor presented here allows decoupling the Q-factor and the optical exposure, thus achieving a boost in sensitivity. The sensitivity characterization is presented, showing the comparable sensitivity of the sensor with focused piezoelectric transducers of sub mPa/√Hz NEPD. In this attempt to boost the sensitivity of the optical ultrasound sensor, the criteria for resolution and detection aperture were relaxed, leading to a different applications pool – which is also discussed in the chapter.

5.2 D-shape Sensor Design and General Consideration

5.2.1 Exposure of light using D-shape fiber sensor

In a standard single-mode, step-index optical fiber, the behaviour of the guided mode can be exactly derived by solving Maxwell equations in cylindrical coordinates [42]. The optical field distribution of the guided mode along the radial axis is represented by Bessel function of the first kind, which has a maximal at the center of the fiber and decays toward increasing the radial distance. The optical energy of the guided mode is usually confined in the core region of the fiber, leaving most of the cladding with no energy flow.

For many sensing applications, the direct interaction of the guided optical mode with the measured object to accurately quantify its quantity. Examples of such applications would include biosensing, chemical sensing, etc. For optical fiber to be used in those applications, there exists a common approach called “side-polished fiber” (SPF) [163]. In this approach, part of the cladding and potentially part of the core of the optical fiber is removed from the side (normally by polishing), leaving the optical energy exposed to the reactants. Thus, any change in the surroundings induces change in the guided mode, i.e., its intensity, scattering, interference, etc [164-167]. The cross section of the SPF has the shape of the letter “D” instead of a perfect circle as in the case of normal fiber, so SPFs are also called D-shape optical fibers.

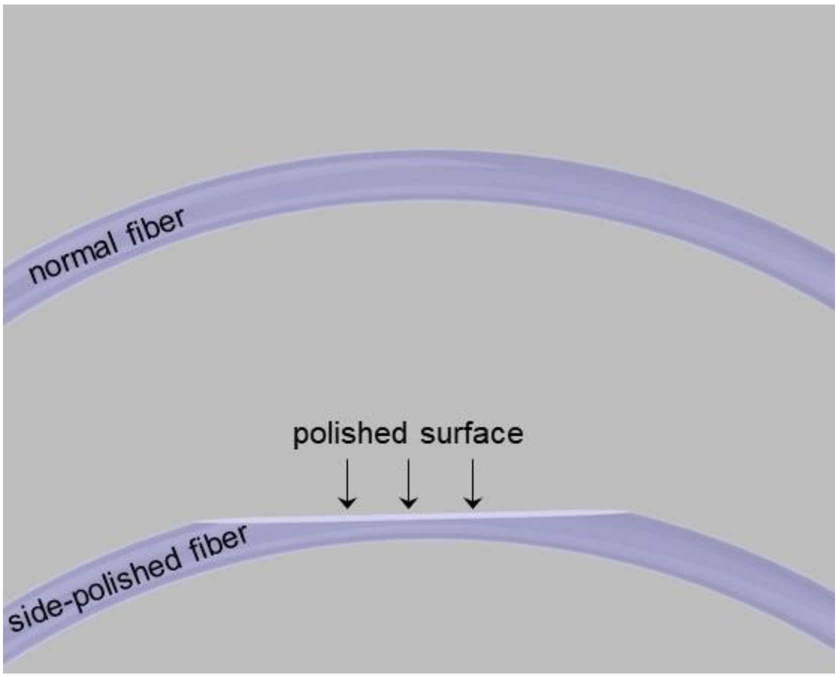

Figure 5.1 - Normal optical fiber (top) and side-polished fiber (bottom).

As being discussed in the previous chapter, the exposure of optical energy to the detection surface of an optical ultrasound sensor. Applying the D-shape structure to a fiber could theoretically significantly enhance the exposure of the optical energy to the detection surface, as being illustrated in Figure 5.2. In fact, couple of works have demonstrated D-shape fibers as ultrasound/ acoustic sensors with improved sensitivity compared to ordinary circular fiber [168]. However, none of the existing works showed a D-shape fiber on an optical resonator – which has the effect of sensitivity amplification.

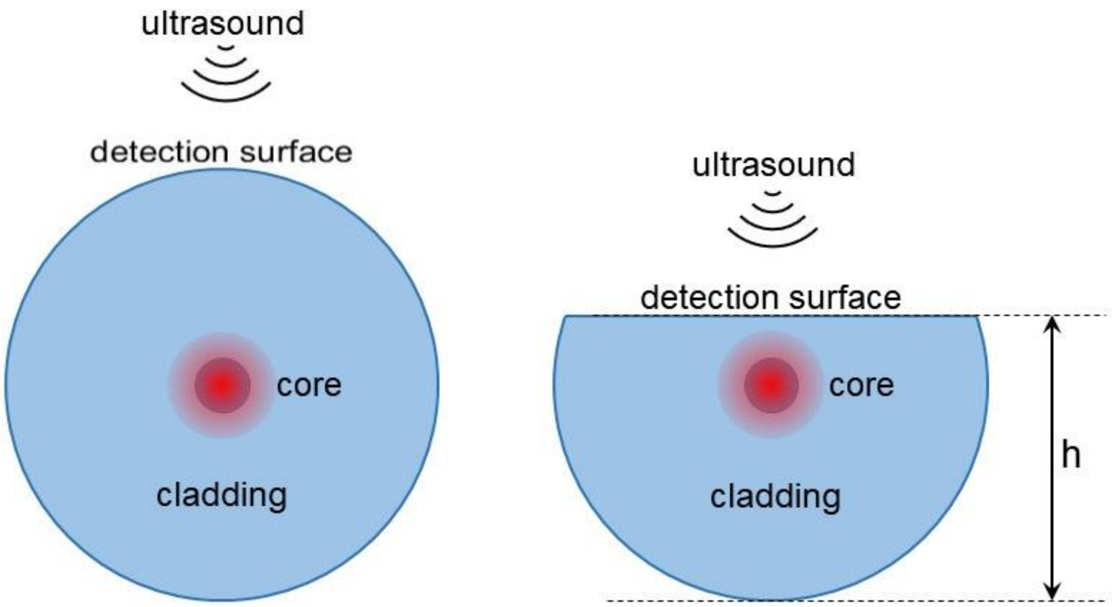

Figure 5.2 - Exposure of the optical field in ordinary fiber (left) and D-shape fiber (right) to the ultrasound detection surfaces. The red region indicates the guided optical mode propagating in the core region of the fiber. The parameter h is called "remained thickness" of the D-shape fiber.

5.2.2 D-shape Fiber Bragg Grating

In this chapter, a special D-shape fiber was fabricated based on a pi-shifted FBG, named DFBG. The pi-shifted FBG confines optical energy around the sub-micrometer-length pi-shifted cavity. Therefore, to maximize the optical exposure, the cladding surrounding the pi-shifted cavity must be most exposed to the detection surface. Due to the axial symmetry of the pFBG, the controlling of the polishing process reduced to a 2-dimension controlling problem. These two dimensions are the axial dimension along the fiber axis – which determines where should the polishing be performed along the fiber and the radial axis – which determines to what extent should we polish toward the core of the fiber. For the axial axis, we should be able to precisely locate the position of the pi-shifted cavity. For the radial axis, we must determine the optical polishing depth to achieve maximal exposure of optical field to ultrasound field, thus obtaining highest possible sensitivity.

5.3 Realization and Characterization of the D-shape Fiber Bragg Grating

5.3.1 Fabrication

a) Optoacoustic Mapping of Optical Distribution

As being identified in Section 5.2.2, realization of the DFBG requires the determination of the location of the pi-shifted cavity in the axial axis. The spectrum matching method, while providing the distance from the pi-shifted cavity to the tip of the fiber, requires removing part of the grating – which is undesirable since we want to keep the grating untouched. The method to roughly determine the location of the grating using the IVUS (Section 4.4.2) is promising but does not provide sufficient resolution to resolve the position of the sub-µm cavity.

In this section, we introduce an innovative method to visualize the optical distribution inside a pFBG resonator and determine the location of the pi-shifted cavity. The basic idea is to use the pFBG as an ultrasound resonator and visualize the sensitivity distribution across the axial direction because this sensitivity is directly proportional to the optical intensity inside the resonator [156,169]. The key challenge here is to design a system that produces sufficient resolution, and we addressed this challenge with a solution based on optical-resolution optoacoustic microscopy. We called this method "Optoacoustic Mapping of Optical Distribution". The experiment setup is depicted in Figure 5.4a. Herein, a point-like acoustic source was generated by focusing the ns-laser onto the 200-nm-thick gold film coated on the surface of a standard microscope cover slip. A pFBG was aligned parallel to the surface of the gold-coated cover slip and almost touched the gold surface. The purpose of the minimal distance between the source (the gold film) and the detector (the pFBG) was to avoid the optoacoustic waves those reach the detector becoming paraxial waves and the sensing effect is averaged over the axial dimension of the fiber, thus enlarging the resolution of the method. We used the pFBG as an ultrasound detector and scanned the pFBG over this point-like acoustic source along the axial dimension of the fiber to obtain a map of sensitivity distribution. At each scanning position, the ultrasonic sensitivity is proportional to the local optical intensity of the fiber. Because the optical intensity inside a pFBG is strongest at the pi-shifted cavity and decays exponentially toward the two ends of the grating, the position of maximum sensitivity indicates the position of the pi-shifted cavity.

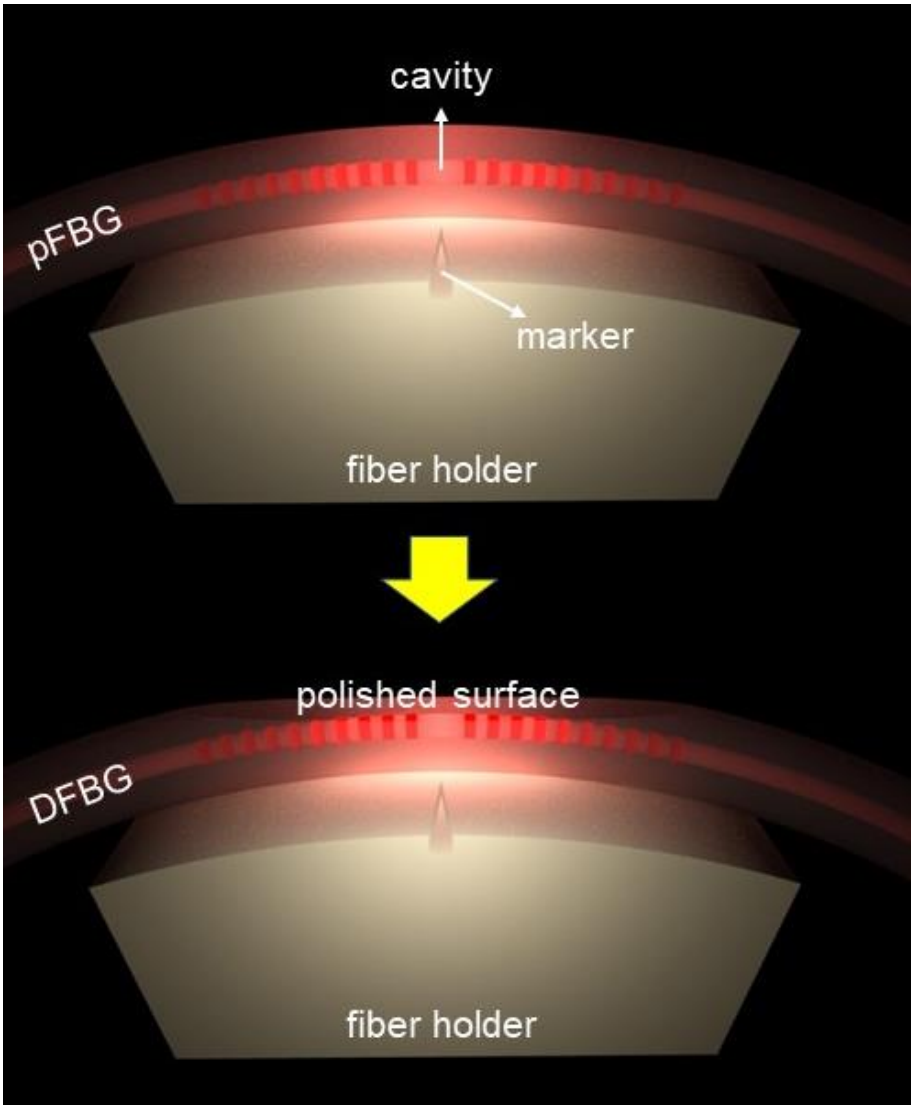

Figure 5.3 - The D-shape Fiber Bragg Grating (DFBG) fabricated by polishing away part of the cladding region around the pi-shifted cavity to expose the confined light inside the cavity to the detection (polished) surface.

Figure 5.4b shows the excellent agreement in optical intensity distribution inside the pFBG between TMM-based simulation and the OMOD measurements, proving that the OMOD method accurately represents the optical intensity distribution inside the pFBG.

The resolution of the OMOD method is generally determined by the size of the point-source, which is < 5 μm in our system. It is also worth mentioning that the OMOD method proposed here can be perform in 2D and 3D scanning, thus is capable of visualizing the optical intensity distribution in other types of optical resonators and structures, for example: normal grating, microring resonator, etc. Up to our knowledge, this is the first method to directly visualize the optical intensity distribution inside optical structures, and OMOD could found potential applications in optical device physics.

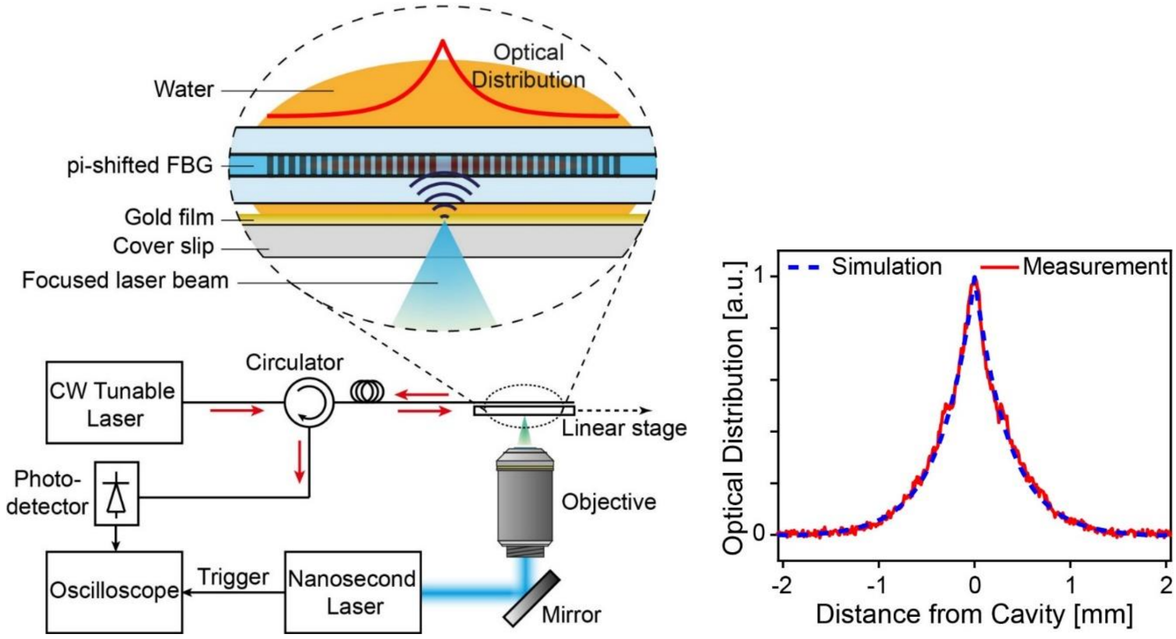

Figure 5.4 - Optical Mapping of Optical Distribution (OMOD) inside a pFBG. (a) Experiment setup. (b) OMOD measurement of the optical distribution (red solid curve) versus the theoretical distribution computed by the transfer matrix method (blue dashed curve).

b) Fabrication of the D-shape Fiber Bragg Grating

Fabrication of the DFBG requires side-polishing a pFBG around the grating region, which was done by immobilization of the pFBG on top of a curved fiber holder and polishing away part of the outer cladding using flat lapping films. The fiber holder was made by stainless steel and had a curved top surface with radius of curvature of 5 cm. The pFBG was fixed onto this curved surface and bended accordingly to the curved direction. The most noticeable feature of the fiber holder is the existence of the marker at the top position of the curve surface to visually indicate this position under a microscope. This marker was formed by cutting the stainless-steel surface with CNC machine. Because the fiber region locating at this top position is polished the most, the critical requirements in fabrication of the DFBG is to align the pi-shifted cavity with this top marker of the holder. We successfully accomplished this task with the help of the OMOD method.

After conducting the OMOD measurement to obtain the optical intensity distribution, the pFBG was moved to the position of maximum sensitivity. In this position, the pi-shifted cavity was on top of the optoacoustic point source, as illustrated by the inset in Figure 5.3. Next, the water drop used as ultrasound coupling media was drained out with tissue paper. Then the gold film used to generate the optoacoustic signal was carefully removed from the setup without touching the pFBG. We slightly lifted up the microscope objective so that the focal spot moved to the surface of the pFBG. The ns-laser power was increased and after sufficient amount of time (10-15 seconds), the focused laser beam burned the outer surface of the fiber cladding and left a black spot with diameter of approximately the focal spot size (few µm in diameter). This black spot is obviously visible under the microscope and indicating the position of the pFBG. The pFBG was then placed on the fiber holder so that the black spot on the fiber surface was aligned with the marker on the fiber holder. The alignment was performed in the system depicted in Figure 5.5, wherein the pFBG was clamped by two fiber clamps mounted on a XYZ microstages and observed with a microscope. After the pFBG had been properly aligned onto the V-groove, we used a small injection needle to take a small amount of ultraviolet (UV) curable epoxy (NOA 81, Norland, USA) and carefully applied it onto the V-groove region. An UV diode was then used to solidify the epoxy and firmly fixed the pFBG onto the holder. Then, the two fiber clamps were released and the pFBG was transferred to the polishing process.

To polish the pFBG, the fiber holder was inserted into a custom-made polishing disk in a reverse orientation, where the polishing surface intersects with the pFBG at the position of the pi-shifted cavity (Fig. 5.6). We used the diamond lapping film with grid size of 1 µm to slowly polish away part of the cladding to create the DFBG.

A major fabrication challenge of the DFBG is to obtain the smallest possible value of the remained thickness h without inducing optical loss and thus reducing the Q-factor of the resonator. To do this, we first performed a numerical simulation based on a mode solver [170] to study the optical guidance property of optical fiber once the remained thickness h is decreased. Fig. 5.6 exhibits the simulation results when h decreases from 125 µm (un-polished) to 63 µm. It can be observed that as h decreases to 75 µm, there is negligible effect of the side-

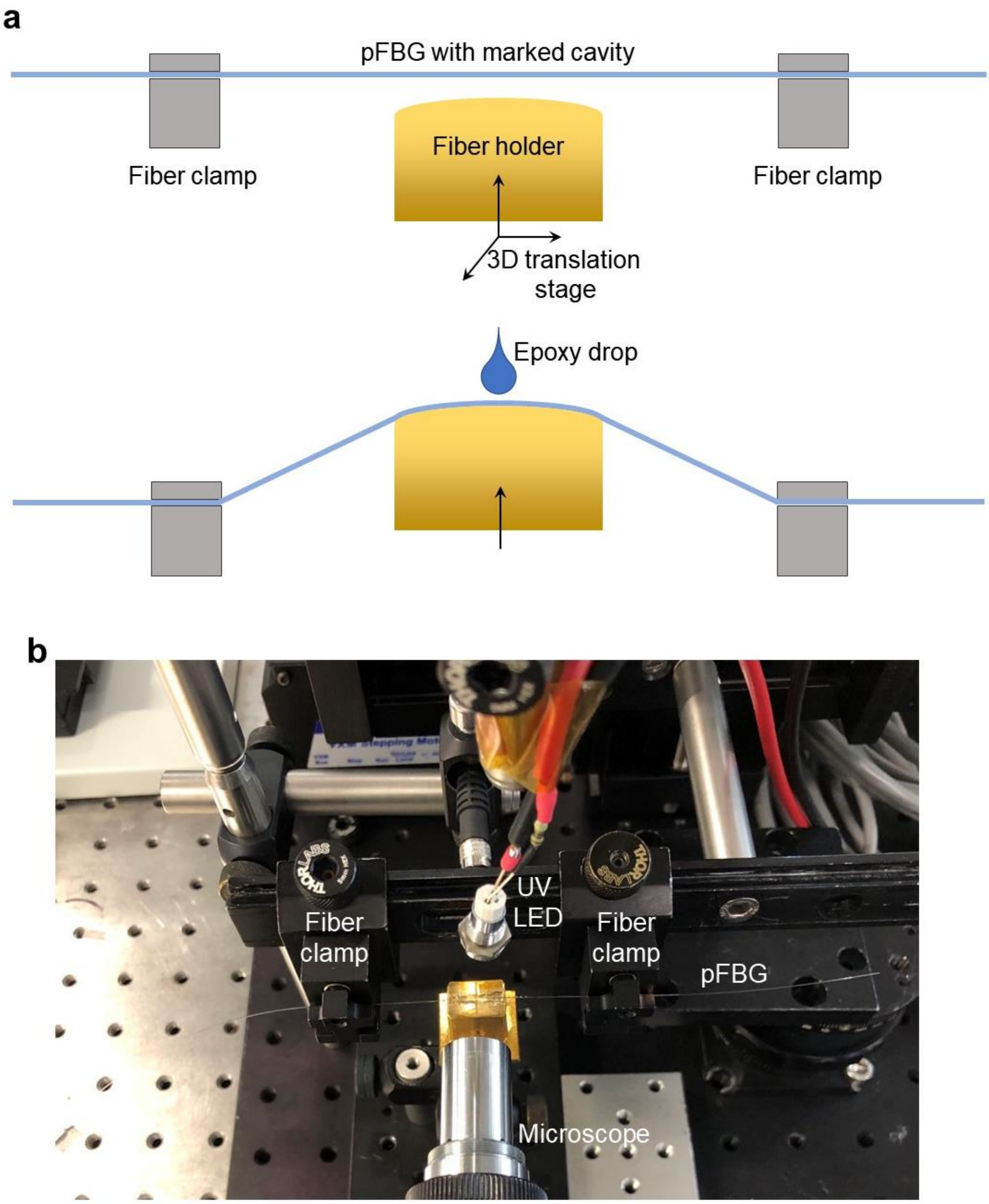

Figure 5.5 - System for alignment of the marked pFBG onto the fiber holder. (a) Schematic of the system. (b) Picture of the system after the epoxy has been dropped onto the holder. The marker on the pFBG and on the fiber holder a visualize under a digital microscope for precise alignment.

polishing process onto the optical loss and the confinement of the guided mode within the core region. As h approaches 70 µm, the guided mode starts to feel the polished surface and is compressed to the non-polished side of the fiber, resulting in increased optical loss of the guided mode. This "compressing effect" is stronger as h continues to decrease to below 70 µm and the guided mode is eventually pushed out of the core. As h continues to decrease beyond 63 µm, optical field no longer feel the core and the whole fiber (including the cladding) becomes the waveguide (Fig. 5.7).

As shown by the simulation, the smallest possible value of h without introducing optical loss to the resonator is approximately 75 µm. Therefore, it is critical for side polishing the DFBG to achieve h = 75 µm. Unfortunately, the remained thickness of the DFBG is not observable once it was fixed into the fiber holder due to the obstruction of the epoxy glue. We then have to indirectly control the value of h by a method called "mean polishing time". With the first DFBG, we continuously monitored the spectrum of the DFBG during the side polishing process and measured the Q-factor of the resonant notch. As soon as an obvious drop in Q-factor is observed (Fig. 5.8), we stopped the polishing process and assigned the current state of the DFBG to have h = 70 µm. Indeed, this estimation gave really good prediction of the remained thickness. Fig. 5.9a shows the cross section of this over-polished DFBG observed under a microscope. The estimated h of this DFBG from the microscopic image was 70 µm – which agrees well with our estimation based on loss in Q-factor. Under constant polishing pressure, it was measured to take approximately 11 minutes to reduce h from 125 µm to 70 µm – which means h reduces by 10 µm every two minutes of polishing. We then stop the polishing process after 10 minutes to achieve optimal h of 75 µm.

After the side-polishing process was finished, the DFBG should be removed from the bulky metallic holder. To do this, we used a hot air blower to blow into the bottom surface (the flat surface) of the metallic holder, heating it to approximately 200^{o}C. The temperature is conducted to the curved surface and soften the epoxy glue. The DFBG then was detached from the holder by carefully pulling the fiber out of the softened epoxy (Fig. 5.9b). The residual epoxy on the surface of the DFBG was removed by soaking the fiber in methylene chloride (C2H2Cl2, Sigma Aldrich, USA).

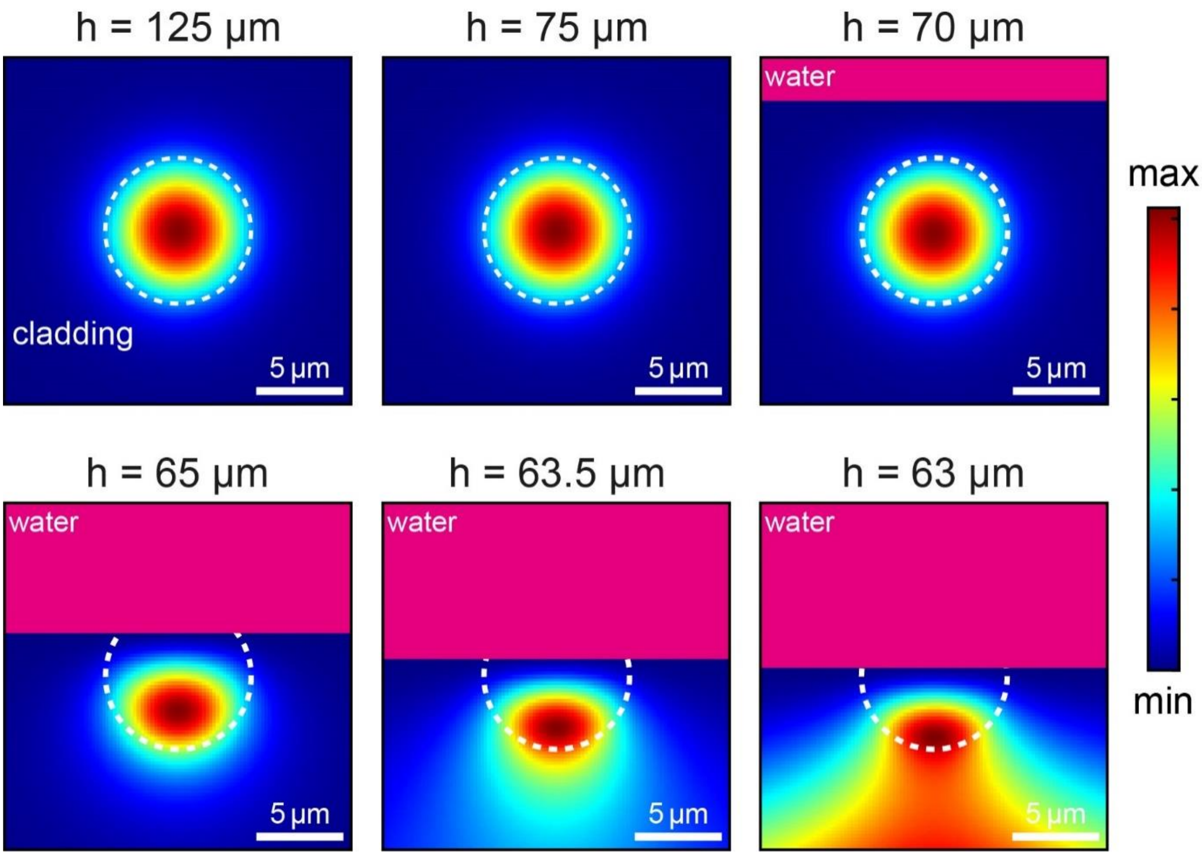

Figure 5.6 - Simulation of optical distribution inside the DFBG when h decreases from 125 um to 63 um. The white dashed circle represents the boundary between the core and the cladding of the fiber. The simulation area is 20 µm × 20 µm around the center of the fiber.

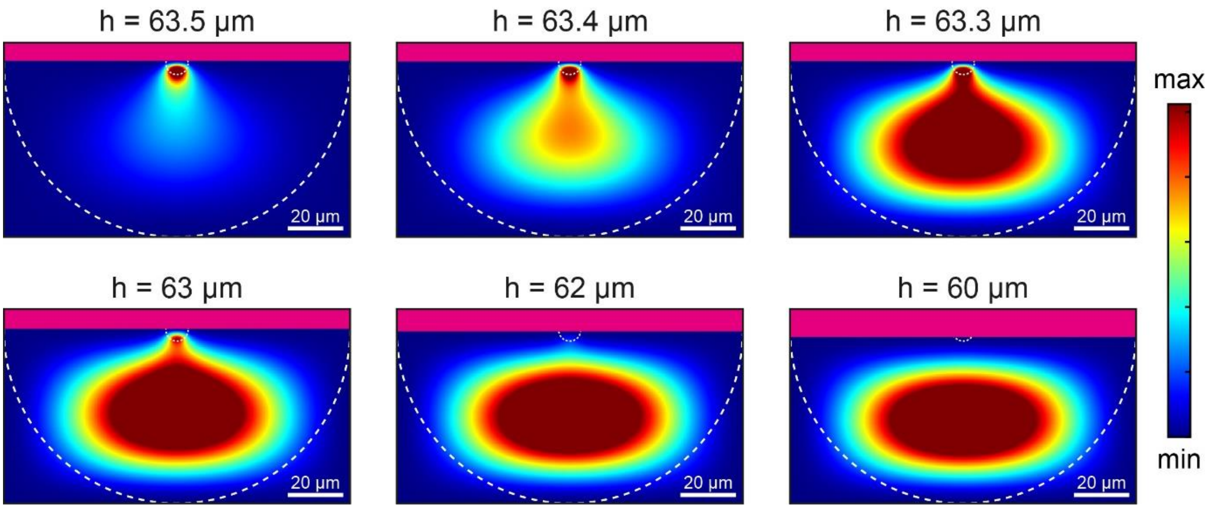

Figure 5.7 - Simulation of optical distribution inside the DFBG when h decreases from 63.5 um to 60 um. The small, dashed circle represents the boundary between the core and the cladding of the fiber. The large, dashed circle represents the boundary of the outer cladding of the fiber The simulation area is 70 µm × 125 µm.

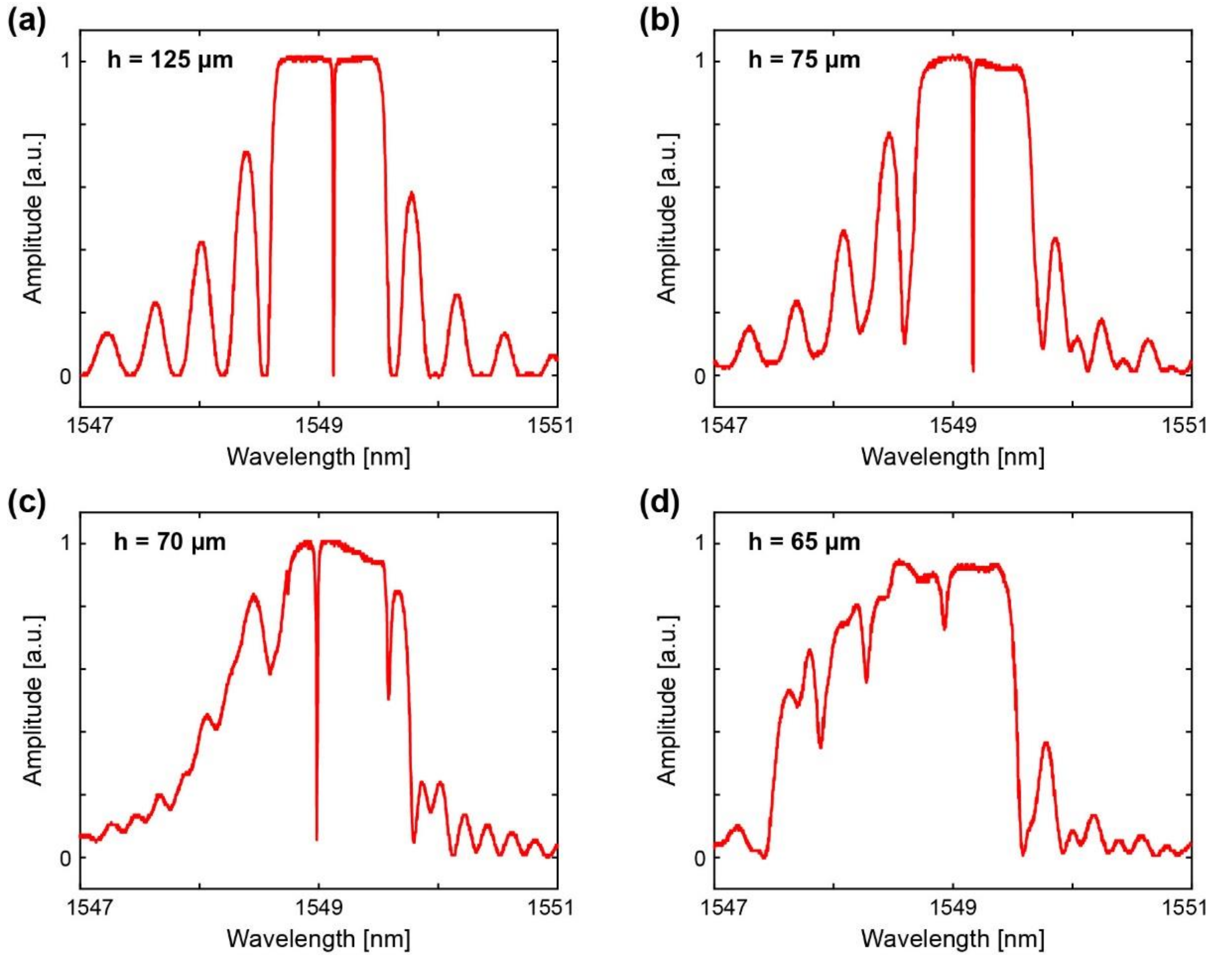

Figure 5.8 - Spectrums of the DFBG during the side-polishing process to reduce the value of h.

5.3.2 Characterization

a) Sensitivity

We first monitored the effect of the side polishing process onto the sensitivity of the DFBG. It was estimated that the remained thickness h decreases by 5 μm after every minute of polishing. We then characterized the sensitivity of the DFBG after every 5-μm-decrement of h by measured the response of the DFBG under the same ultrasound excitation source. The relative sensitivity of the DFBG during the side polishing process is plotted in Fig. 5.10.

It is observed that as h decreases from 125 μm to 75 μm, the sensitivity of the DFBG experiences a five-fold improvement. It is worth mentioning that the measured optical Q-factor of the DFBG remains unchanged during this process, which indicates the same amount of light circulating inside the resonator. This means that under the same incident pressure wave, the DFBG is more "perturbed" as h decreases – which is attributed to the enhanced interaction between acoustic and optical fields inside the DFBG. As h continues to decrease beyond 75 µm, the increased optical loss induces a drastic decrement in optical Q-factor, and the sensitivity collapses. So, it was confirmed experimentally that the value of h for optimal sensitivity is 75 µm – where the guided mode is unaffected by the disturbance of the fiber geometry due to the existence of the polishing surface.

Next, we calibrate the absolute sensitivity of the most sensitive DFBG with h = 75 µm (called DFBG from here) by measuring its NEPD. We also characterized the sensitivity of two state-of-the-art focused piezoelectric transducers currently used for commercial optoacoustic systems to compare their sensitivity with the DFBG. The information of these two focused piezoelectric transducers is listed in Table 5.1.

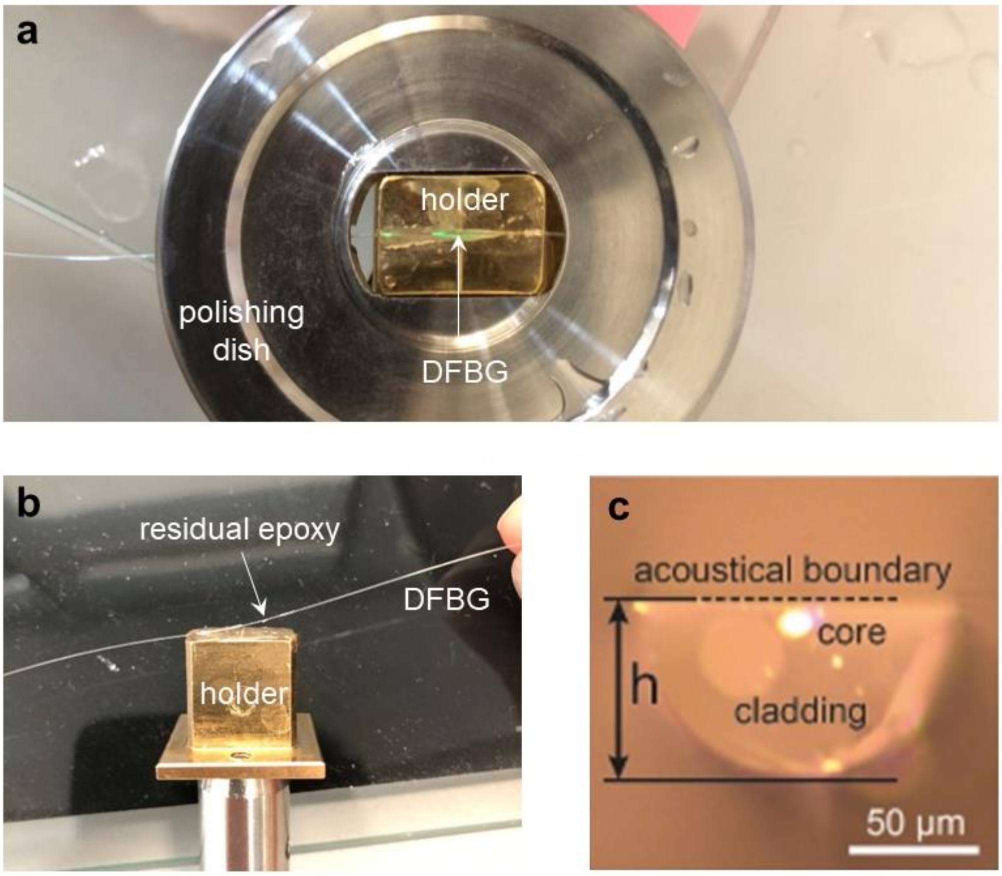

Figure 5.9 - Pictures of the DFBG. (a) The DFBG after polishing. A green laser is interrogated into the DFBG, and light is leak out of the polished region. (b) The DFBG is easily removed from the metallic fiber holder after the epoxy has been softened by heat. (c) Cross section of an over-polished DFBG with h = 70 um. The core is interrogated with white light for visualization.

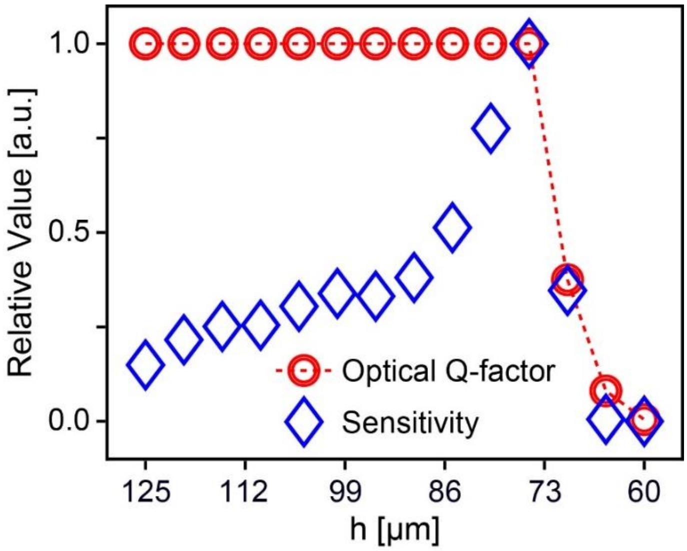

Figure 5.10 - Sensitivity and Q-factor of the DFBG with respect to h.

Because the three detectors have different spectral properties, it is necessary to characterize their bandwidths prior to characterize their sensitivity, so the NEP extrapolation method can be used for accurate estimations of their sensitivity. The bandwidths of the three detectors are exhibited in Figure 5.11.

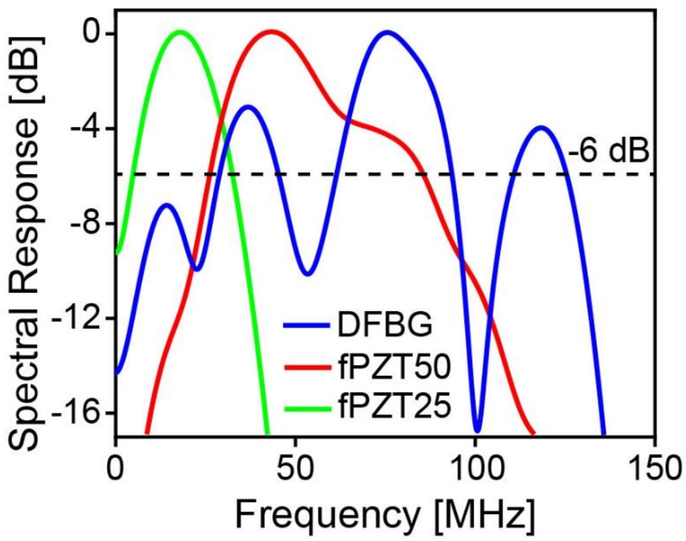

Figure 5.11 - Bandwidths of three detectors used for comparison. The fPZT25 has center frequency of approximately 25 MHz. The fPZT50 has center frequency of approximately 45 MHz. The DFBG has center frequency of approximately 75 MHz.

The sensitivity characterization process is described in detail in **Appendix C**. However, for a fair comparison, we characterized the two focused piezoelectric transducers at different distances from the detectors to the optoacoustic point source, which correspond to the positions of optimal sensitivity for each detector (their focal distances). The responses of the three detectors and the needle hydrophone used for calibration over the calibrated bandwidth of the hydrophone (10-30 MHz) are presented in Figure 5.12. Using the data from the bandwidth characterization and the needle hydrophone calibration, the sensitivity of the three detectors were presented in Table 5.2.

The optoacoustic responses of the three detectors with respect to distance are plotted in Figure 5.13. The optoacoustic source was generated by focusing the ns laser beam onto a black vinyl film. The same optical power for excitation was used for all detectors. All of the signals were normalized so that they have the same noise level and passed through a 10-30-MHz digital filter. It can be observed that the response of the DFBG is inversely proportional to the distance between the detector and the source, which perfectly represents the reduction in amplitude of a spreading spherical wave (blue dashed curve). In contrast, the amplitudes of the signal measured by the two focused piezoelectric transducers do not follow the spherical wave propagation but have their maximums at the focal distance and degrade quickly out of their focal regions. These signal amplitudes show that the sensitivities of the focused piezoelectric transducers depend on the working distance and reach their maximal (0.35 mPa. $Hz^{-1/2}$ for the fPZT25 and 0.39 mPa. $Hz^{-1/2}$ for the fPZT50) at the working distance corresponding to the focal length, while the sensitivity of the DFBG (0.42 mPa. $Hz^{-1/}2$) is independent of distance. Therefore, the DFBG is expected to be more sensitive than the two piezoelectric transducers once the optoacoustic source is offset from the focal planes by a small distance (estimated to be 150 µm for the fPZT25 and 50 µm for the fPZT50). This characteristic of the DFBG is especially beneficial in OR optoacoustic microscopy. Herein, to accelerate the imaging speed, optical scanning of the focused beam using resonant mirror is often employed. The field of view using this optical scanning technique is normally on the order of several hundreds of micrometers. A typical focused piezoelectric transducer used in the OR optoacoustic microscopy with 50-MHz center frequency has the focal spot size of just over 30 µm. This focal spot size is not large enough to cover the optical scanning field, and the sensitivity of the system would degrade quickly out of the focal spot if the acoustic focal plane is aligned on the optical focal plane. A common approach here is to slightly defocus the focused piezoelectric transducer so the acoustic sensitive region is large enough to cover the optical scanning region [171]. According to our measurement of sensitivity vs distance for the focused piezoelectric transducers, this could quickly decrease the sensitivity of the system, depending on the optical field of view.

Table 5.1 - Specification of the two focused piezoelectric transducers used for comparison with the DFBG

Name	fPZT25	fPZT50
Manufacturer	SONAXIS, France	SONAXIS, France
Model	CMF183 – PR 6V	HFM31 – PR 6V
Design center frequency [MHz]	25	50
Diameter [mm]	6	4
Focal length [mm]	6	4

Table 5.2 - Characterization result for the three detectors

	DFBG	fPZT25	fPZT50
Sensitivity in the 10-30 MHz band [mV/kPa]	394	109	62
Bandwidth with maximum response [MHz]	70-90	10-30	34-54
Sensitivity over the bandwidth with maximum response [mV/kPa]	983	109	119
Rms noise over the bandwidth with maximum response [mV]	1.8360	0.1699	0.2097
Maximum NEP over a 20 MHz bandwidth [Pa]	1.8671	1.5562	1.7604
Maximum NEPD [mPa. $Hz^{-1/2}$]	0.4175	0.3480	0.3936

b) Optical resolution optoacoustic microscopy

To demonstrate the relevant of the DFBG with OR optoacoustic microscopy, we compared the performance of a transmission-mode OR optoacoustic microscopy using the DFBG and the original pFBG [144]. The optoacoustic microscopy system used the same optical components for focusing the ns laser beam to a diffraction-limited spot, similar to the setup used for bandwidth characterization. The imaging sample is a black micro-suture having diameter range from 10

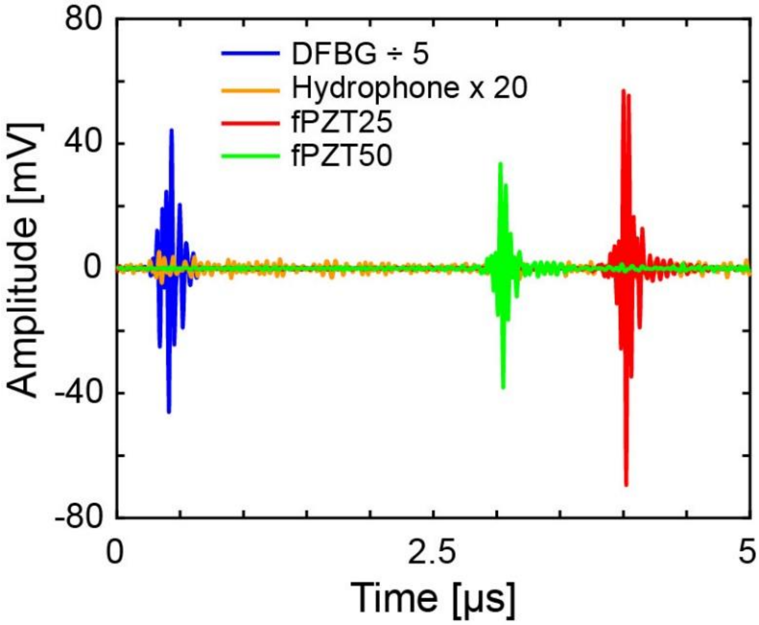

Figure 5.12 - Time domain signal of the reference needle hydrophone and the three calibrating detectors. All signals were passed through a 10-30 MHz bandpass digital filter.

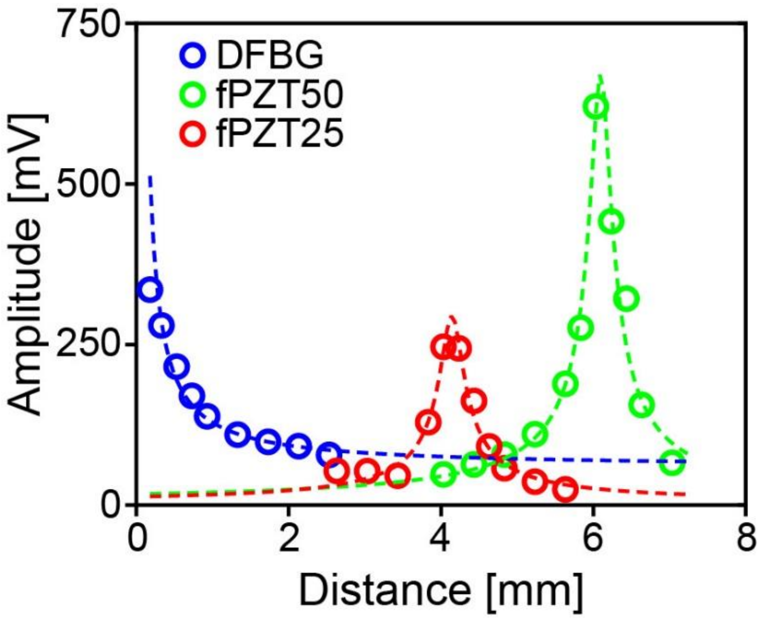

Figure 5.13 - Peak to peak responses of the DFBG and two focused piezoelectric transducers under the same OA source with respect to distance between the detector and the source. The corresponding fits are plotted in dashed curves.

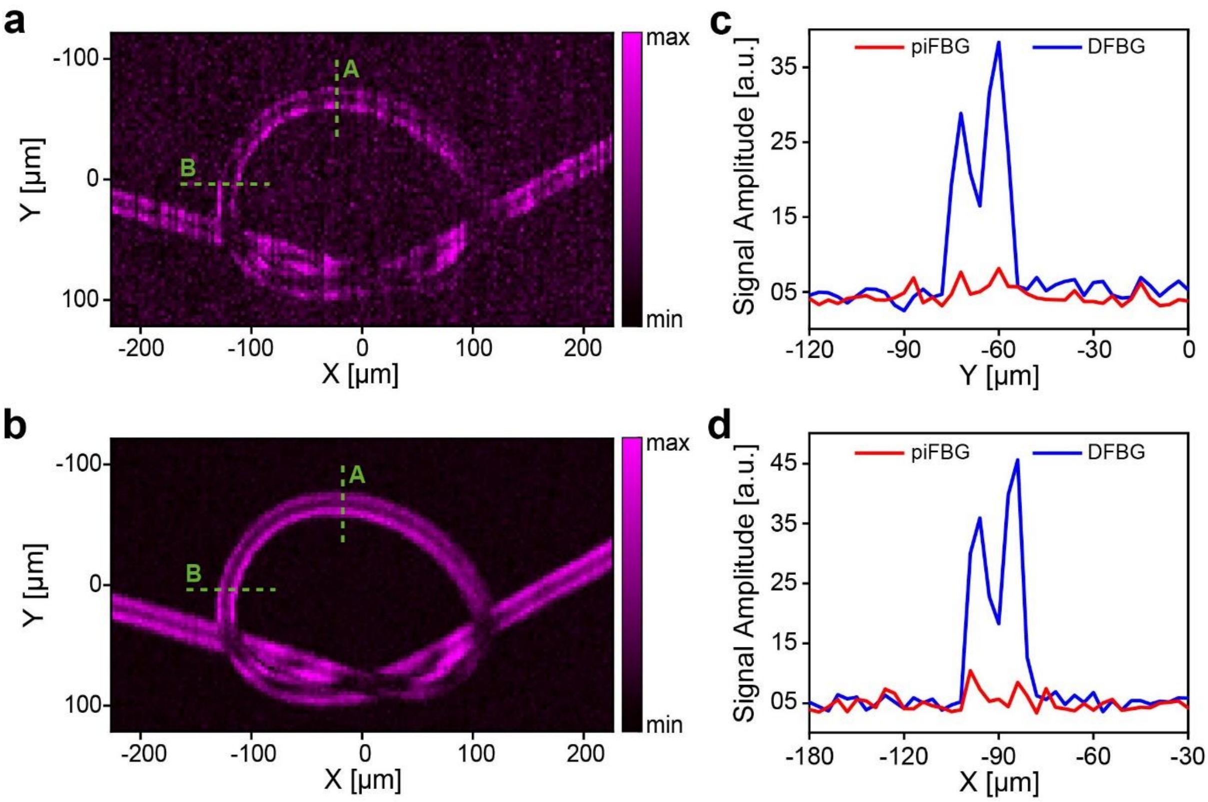

Figure 5.14 - Optical resolution OA microscopy of a knotted suture using low excitation power. (a, b) Maximum intensity projection image using the pFBG (a) and the DFBG (b) as the OA detector. (c, d) The image profile of the A-line (c) and B-line (d) in Figure 5.14a and b.

to 19 µm. The suture was knotted into a knot shape and immobilized on a 2D microscope scanning stage (MLS 201-1, Thorlabs Inc., USA. The fiber detectors were held on top of the suture sample at a distance of 0.5 mm away from the suture. Water was used for ultrasound coupling of the OA signals from the black suture to the fiber detectors.

For the optoacoustic microscopic experiment, the ns laser has pulse repetition rate of 1.35 kW and the average power of 150 µW, which correspond to a laser pulse energy of approximately 111 nJ/ pulse. This laser pulse energy is several orders of magnitude smaller than the pulse energy normally used in OA microscopy, which could reach hundreds of uJ per pulse [144,171,172]. The maximum intensity projection (MIP) of the suture phantom using a DFBG and an original pFBG detectors are exhibited in Figure 5.16. The DFBG showed a remarkable enhancement in image contrast thank to a higher sensitivity compared to the pFBG. The profiles of the suture using two detectors are shown in Figure 5.17. More than 5-fold of SNR improvement was observed by using the new DFBG detector.

c) Single-particle sensing

For the final demonstration of the sensitivity of the DFBG, we performed a single-particle sensing experiment. Herein, we would try to detect the optoacoustic signal emitting from a single microscale absorber (Figure 5.15). optoacoustic signal detection from single absorber is important in applications such as optoacoustic sensing or especially optoacoustic flow cytometry [173,174].

The chosen absorber for this experiment is black polystyrene microspheres with diameter ranging from 10 to 20 µm. To prepare the sample for this experiment, the most important requirement was to ensure there exists only one microsphere across the total optically illuminated area. To do this, we first applied a layer of optically transparent adhesive (OCA8146-2, Thorlabs, USA) onto the surface of a cover slip. A plastic tube containing the microspheres was slightly flicked to release a small amount of microsphere on top of the adhesive layer. Then we place the polyester release liner used to originally seal the adhesive tape on top of the adhesive and gently press the liner to ensure good adhesion between the microspheres and the adhesive layer. The process for preparing the sample is illustrated in Figure 5.16. After all microspheres were stably fixed by the adhesion layer, the cover slip was observed under a microscope to find a single microsphere that was well-separated from the other. Figure 5.20 shows a microsphere that was far away from the others, and this microsphere was chosen as the absorber for our experiment.

For excitation of optoacoustic signal from the microsphere, the laser power was set at 150 uW, which corresponds to pulse energy of 74 nJ/pulse. We tightly focused the excitation laser onto the microsphere and conducted optical resolution optoacoustic microscopy to measure the exact dimension of the sphere. The microscopic image of the sphere is exhibited in Figure 5.18a and the profiles of the sphere across its center are plotted in Figure 5.18b, c. The diameter of the sphere was estimated to be 22 µm.

We then slightly defocus the microscope objective to reduce the laser fluence used in the experiment (Figure 5.19a). To measure exactly the diameter of the excitation laser beam, we line-scanned the microsphere across the illumination region and obtained the profile of the optoacoustic signal across the line as depicted in Figure 5.19b. Once the microsphere was inside the illumination spot, the optoacoustic signal was emitted and obtained by the ultrasound detector. If the microsphere was out of the illumination spot, there was no absorber inside the

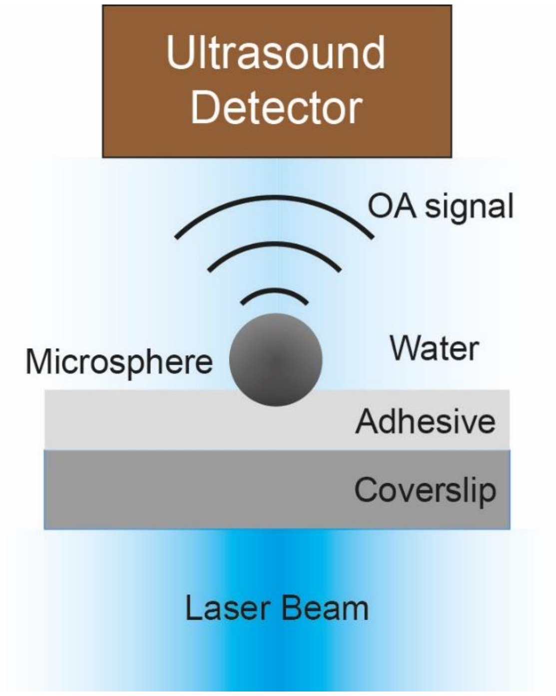

Figure 5.15 - Schematic of a single particle sensing experiment. A microsphere is immobilized on a cover slip by a transparent adhesive layer. A loosely focused laser beam radiated the microsphere, and the OA signal emitted from the microsphere is recorded by the ultrasound detectors with water acting as coupling media.

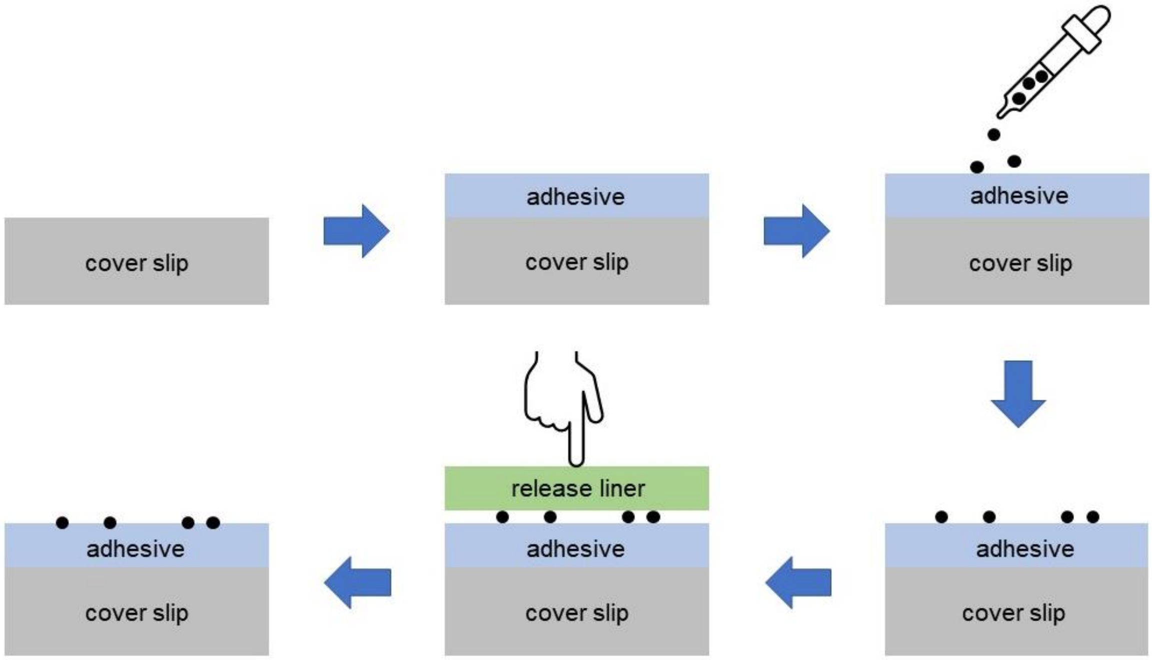

Figure 5.16 - Process of preparing the single particle sample. The transparent adhesive is applied onto the cover slip. Then a plastic tube containing the microspheres is slightly flicked to drop a small number of microspheres onto the adhesive. The release liner of the adhesive is then used to gently pressed the microspheres onto the adhesive layer to ensure strong bonding.

illumination spot and no optoacoustic signal was detected. The diameter of the illumination spot was then determined based on the plot of the optoacoustic signal amplitude in Figure 5.19b and was estimated to be 65-70 µm.

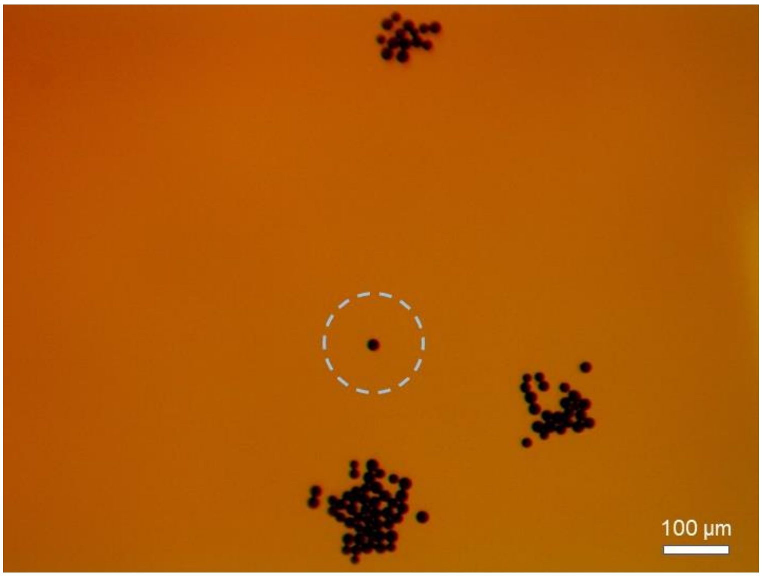

Figure 5.17 - Microscopic image of the sample. A single isolated microsphere (enclosed by dashed circle).

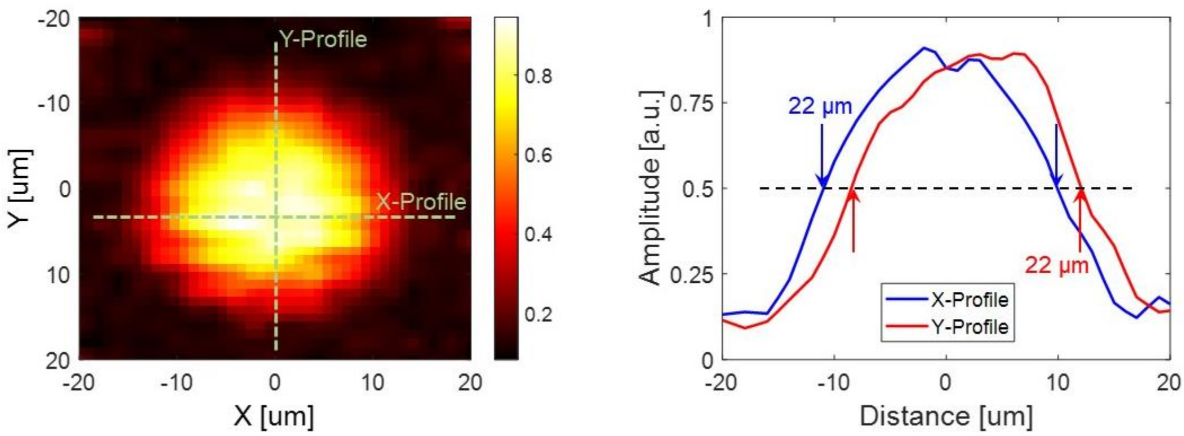

Figure 5.18 - Microscopy of the isolated microsphere in Figure 5.17. (a) Maximum intensity projection image of the sphere. (b) Profile of the X and Y line in (a).

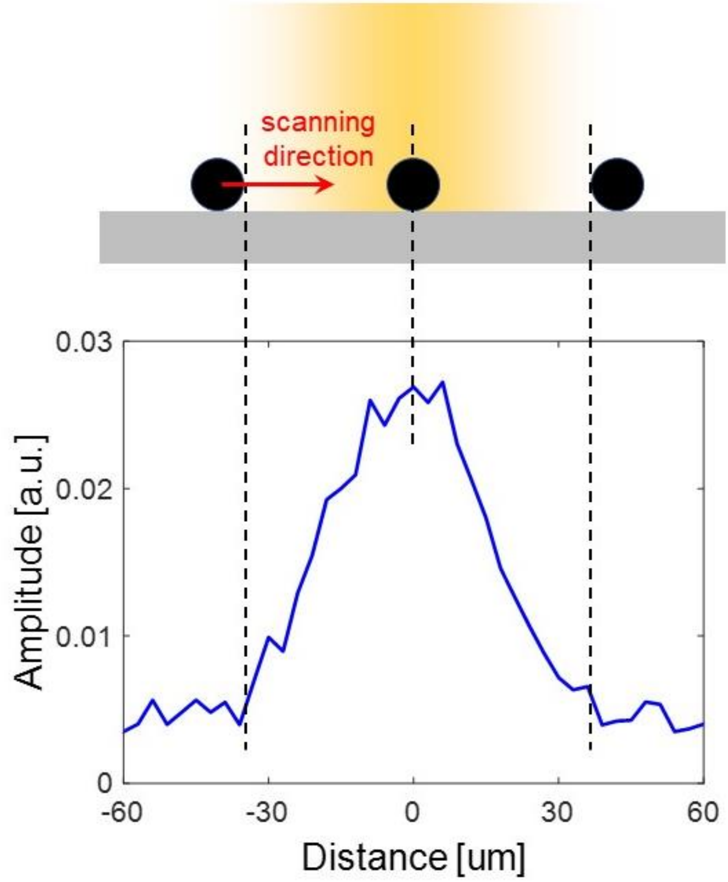

Figure 5.19 - Experiment to measure the beam spot size by scanning the microsphere across the laser beam and record the peak amplitude of the optoacoustic signal.

With this illumination spot diameter of 60 µm, the corresponding laser power and laser energy exposure used in the single particle sensing experiment were calculated to be 3.5 W/cm2 and 2.6 mJ/cm2. These levels are lower than 20% of the ANSI safety limit for visible radiation [39], so the experiment could be applied for biological absorber such as cell. All the experiments conducted with the DFBG used low laser pulse energy that is affordable by cheap laser diode [175-177], which enables the possibility of low-cost optoacoustic system.

After the sample and the exposure had been well prepared and characterized, we used two ultrasound detectors to record the optoacoustic signals emitted from the microsphere under mentioned optical excitation without any signal averaging. The first detector was the DFBG, and the second detector was the fPZT50 – which was chosen for a well-matched bandwidth characteristic with the DFBG. The distance between the microsphere and the DFBG was 0.5 mm, and this distance for the fPZ50 was 4 mm (equal to its focal length for maximal sensitivity). The OA signals recorded by two detectors are depicted in Figure 5.22. The SNR of the DFBG signal was 17 and the SNR of the fPZT50 signal was 17.9. The SNR of the signal recorded by the fPZT50 was slightly higher, probably owing to the better sensitivity of the fPZT50 compared to the DFBG. In addition, the signal recorded by the fPZT50 showed a clearer bipolar shape. Converting the time domain signals into frequency domain revealed the reason of the signal's shape. As can be seen from the spectrum of the signals (Figure 5.20), the DFBG signal possesses several dips – which is accounted for the frequency response of the DFBG itself (Figure 5.11). The fPZT50 has a smoother frequency response, which resulted in a more well-behaved signal spectrum. Both signals possess a dip at approximately 45 MHz. This dip corresponds to the acoustic frequency that induces destructive interference between the optoacoustic wave transmitted directly from the microsphere and the optoacoustic wave being reflected at the adhesive-glass interface (Figure 5.24). Taking the sound velocity of the acrylic adhesive to be 2700 m/s, this dip at 45 MHz corresponds to the distance between the microsphere and the surface of the cover slip of d = 41 µm. This distance is in good agreement with the fact that we gently pressed the microsphere into the adhesive layer with thickness D = 50 µm.

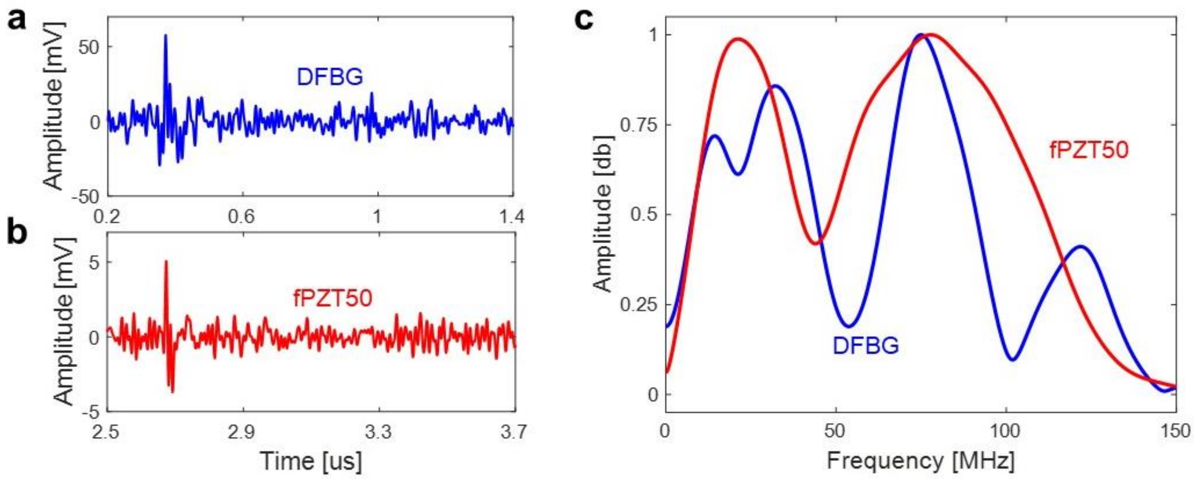

Figure 5.20 - Optoacoustic signal from the single microsphere under diffused illumination. (a, b) Time domain signals recorded by the DFBG (a) and the fPZT50 (b). (c) Frequency domain representations of the two signals in (a) and (b).

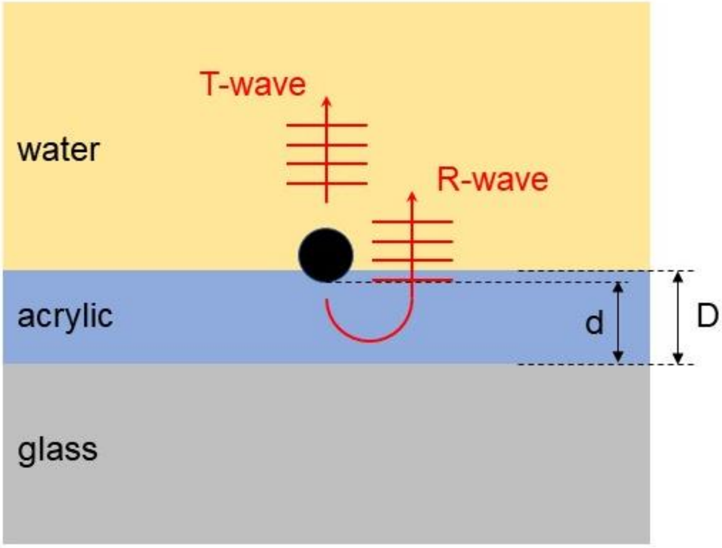

Figure 5.21 - Schematic for optoacoustic signals detected by the detector from the microsphere. The T-wave (propagating directly from the sphere to the detector) interferes with the R-wave (propagate toward the cover slip and being reflected at the interface between the cover slip and the adhesive layer).

5.4 Discussion

The fabricated DFBG demonstrated one of the best sensitivities reported to date for an optical ultrasound detector. However, unlike the original pFBG, the DFBG does not have azimuthal symmetry due to the existence of the flat polishing surface (Figure 5.22). Therefore, precise alignment to facing the sensitive surface toward the OA source must be required to maximize the sensitivity of the detector.

While we have strongly pushed the sensitivity of the detector, the consideration for detection aperture was relaxed. The aperture of the DFBG would have the line-shaped geometry similar to that of the pFBG, and thus the DFBG is not good for reconstruction-based imaging applications such as mesoscopy or tomography. A promising solution to overcome this problem is to bend the DFBG to form a focusing spot – which acts as a virtual detector as in the case of focused piezoelectric transducers. The synthetic aperture using acoustic focusing would have size on the orders of tens of micrometers, depending on the bending radius [178]. In addition, the acoustic focusing could further enhance the sensitivity of the DFBG at the acoustic focus as demonstrated in the same reference. The disadvantage of this approach is the performance deterioration out of the acoustic focal region – which is common among all focused detectors.

However, flexible optical fiber would allow adjustment of the focal distance depending on penetration depth needed, thus greatly improve the versatility of fiber-based detectors compared to piezoelectric transducers.

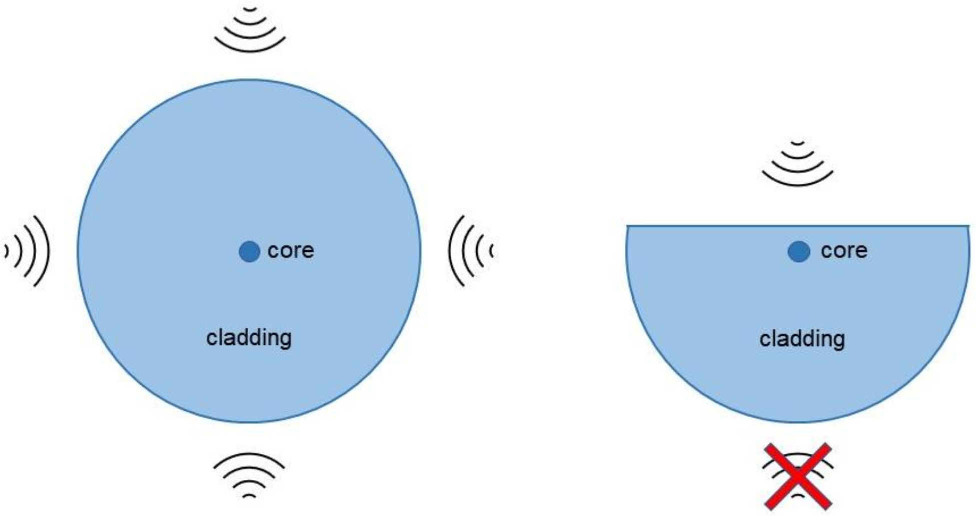

Figure 5.22 - Sensitive direction of the pFBG and DFBG. The pFBG (left) has the same sensitivity regardless of ultrasound propagation direction due to the azimuthal symmetry. The DFBG has maximum sensitivity when incident ultrasound hits the detection (polished) surface.

Chapter 6 : Conclusion and Outlook

The research presented in this dissertation aimed to advance the detection technology for optoacoustic imaging and facilitate the miniaturization of optoacoustic system for off-the-lab transition. Therefore, the thesis stated by providing basic principle of optoacoustic imaging and the differences in configuration of optoacoustic imaging modalities. The focus then shifted to optical resonators as a promising tool to overcome current challenge in detection technology of optoacoustic imaging. Various types of optical resonators were analysed and evaluated based on the theoretical approach. The pros and cons, as well as strategies to improve the performance of those resonators in optoacoustic detection have been discussed carefully. The thesis also pointed out challenge for optical resonators to achieve similar mesoscopic resolution and microscopic sensitivity to focused piezoelectric transducers.

The thesis then spends the next two chapters to present two distinct optical ultrasound detectors that could potentially overcome such challenge. The first detector, the Embedded Etalon resonator (EER) was proposed to significantly improve the optoacoustic mesoscopic resolution. The EER utilize the mode field diameter of a single mode fiber as the detection aperture, and a broad detection bandwidth of > 130 MHz. The chapter provides the transfer matrix method (TMM) as a powerful tool to model, predict, explain the EER's performance and essential tool for success fabrication of the EER. Empirical results showed that the EER has sensitivity of less than 3 mPa/√Hz and spatial resolution on the orders of tens of micrometers upto penetration depth of 8 mm. This combination of sensitivity and mesoscopic resolution is by far the best that ever demonstrated by both optical and piezoelectric detectors. In addition, the EER is encapsulated perfectly in a rigid silica rod of only 125 µm in diameter, provides great biocompatibility and offers the smallest form factor for an ultrasound detectors to-date.

The second detector, the D-shape Fiber Bragg Grating (DFBG) was proposed to boost the sensitivity of optical resonator-based detectors using a new approach: exposure of optical and ultrasound fields. The optimization of the optical and ultrasound fields in the DFBG requires precisely control of the relative position between the optical cavity with the detection surface on the order of few micrometers. In the normal direction with respect to the detection surface, this controlling was guided by the simulation of the mode field distribution in side-polished fiber waveguide. In the tangential direction with respect to the detection surface, this precise control was experimentally guided by a newly developed method call Optoacoustic Mapping of Optical Distribution (OMOD) – a first-of-its-kind method to visualize the optical distribution inside an optical resonator. Preliminary results showed that the DFBG possess a sensitivity of less than 0.5 mPa/√Hz over a 20 MHz calibration bandwidth, which is the best ever recorded for a broadband optical ultrasound detector.

In addition, both the EER and DFBG are encapsulated perfectly in rigid silica fibers of only 125 µm in diameter, provide great biocompatibility and offer the smallest possible form factor for optical ultrasound detectors. This footprint is at-least 30-folds smaller than piezoelectric transducers of comparable performance. Indeed, the world-smallest catheter was demonstrated using the EER with total size of less than 400 µm – which is small enough to fit into a 3F sheath. The research laid out in this thesis could revolutionize endoscopic imaging and intravascular imaging, taken into account that commercial intravascular ultrasound (IVUS) systems typically provide resolution that is 5 to 10 time worse than what demonstrated in this thesis over the same depth range. Moreover, commercial IVUS systems cost more than $100,000, while the IVUS catheters cost > $3000 and must be replaced after a single use, which all leave a huge potential for low-cost and miniaturized optoacoustic imaging to surpass. To achieve those goals, in addition to the specific advancements that were discussed at the end of the chapters presented the detector, several problems should further be investigated and solved within the scope of future works:

<u>Interrogation systems and environmental susceptibility</u>

The common intensity-based interrogation system of optical detector requires a narrow linewidth tunable laser, which greatly increases the cost and environmental susceptibility of the detector. Advances in pulse interferometry [100,112] have demonstrated great environmental stability as well as superior noise performance – which could greatly improve the reported NEPD of the EER and DFBG. The pulse interrogation system is often complex and requires expensive components such as femtosecond laser. However, silicon photonics in particular and photonics integrated circuits (PIC) in general are now capable of hosting almost all the components of the pulse interrogation system, offering a promising platform for miniaturization of the backend of the imaging system along with miniaturization of the frontend (detector) as presented in this thesis.

In addition, the co-integration of detector interrogation and excitation coupling should be performed via a rotary join to allow rotation of the imaging catheter.

High-repeatability batch-by-batch production

The fabrication procedure of both the EER and the DFBG involves a lot of manual steps, which resulted in moderate batch-by-batch repeatability. Fortunately, all these manual steps can be fully automated without major technical difficulties. For example, during the polishing process of the EER, the polishing setup (Figure 4.15) can be automated by inserting the fiber into a fiber polishing machine. The spectrum matching method is flexible enough to be fully encoded into computer program, wherein the computer can order the polisher to stop when desired spacer length has been reached. In the current version of the EER, the silver layer is used as it enables quick prototyping and testing of the EER. However, the reflectivity of the in-house silver coating is insufficient and the repeatability is relatively low. Deposition method such as gold sputtering or dichroic deposition could significantly enhance the quality and the batch-by-batch repeatability. For side polishing of the DFBG, the process can also be automated by optimization of the polishing time using a fiber polisher similar to the manual polishing process presented.

In vivo and clinical study

The small footprint of the optical ultrasound detectors presented would allow minimal invasive applications to be demonstrated such as laparoscopy [45], intravascular imaging [149] and potentially new applications.

Chapter 7 : Appendix

Appendix A – Transfer Matrix Method

In the Transfer Matrix Method (TMM), the optical structure is sectioned into stack of infinitely wide layers (Figure 7.1). Each layer in TMM is characterized by a 2x2 matrix that depict the relation of the amplitude of the input and output waves travelling in +z and –z directions.

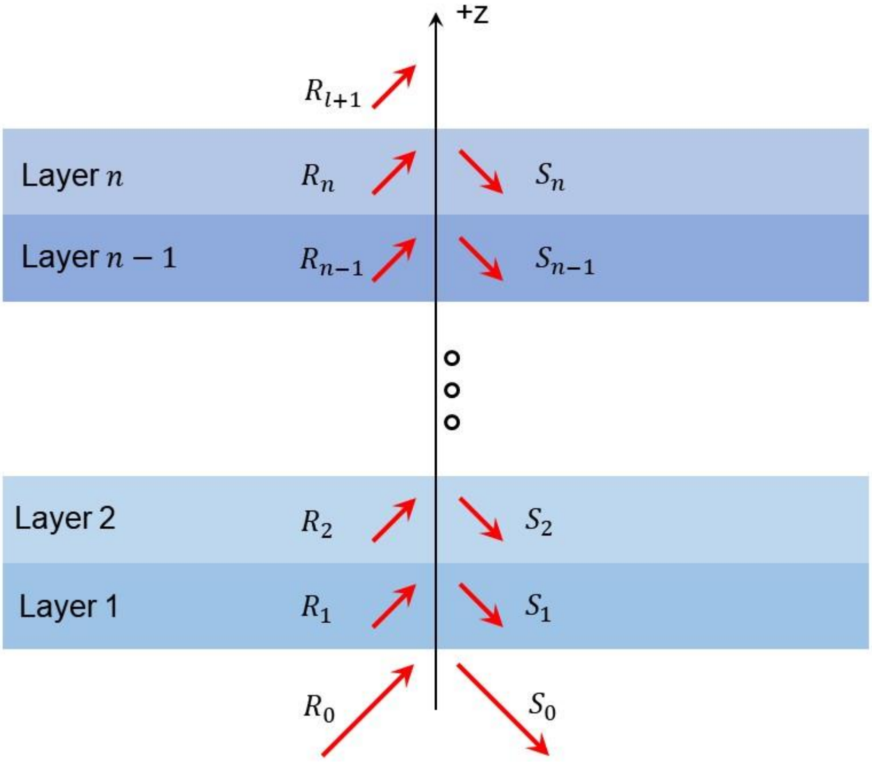

Figure 7.1 - 2D layers in transfer matrix method (TMM). Each layer $\boldsymbol{l}$ is infinitely wide in x and y direction and has thickness $\boldsymbol{d_l}$. Each layer $\boldsymbol{l}$ is characterized by a two-by-two matrix represent the change of the waves travelling in +z and -z direction within that layer compared to the previous layer $\boldsymbol{l-1}$.

The relation between the electromagnetic wave in an arbitrary layer l and in its previous layer $l-1$ can be described as:

$$\begin{bmatrix} R_l \\ S_l \end{bmatrix} = \frac{1}{2}\begin{bmatrix} (1+P)e^{ik_l d_l} & (1-P)e^{ik_l d_l} \\ (1-P)e^{-ik_l d_l} & (1+P)e^{-ik_l d_l} \end{bmatrix}\begin{bmatrix} R_{l-1} \\ S_{l-1} \end{bmatrix} \tag{7.1}$$

where k_l is the wave number in the layer l and d_l is the thickness of the layer l. The coefficient P is defined as

$$P = \frac{k_l}{k_{l-1}} = \frac{n_l}{n_{l-1}} \tag{7.2}$$

where n_l is the refractive index in the layer l. The characteristic matrix of an arbitrary of continuous layers is the product of the characteristic matrices of the corresponding layers.

Appendix B – Calculation of the Reflectivity of a Bragg Reflector

Using the TMM, the reflectivity of a single layer or a stack characterized by a matrix F as described in Appendix A can be calculated via the following equations:

$$r = -\frac{F_{21}}{F_{22}} \tag{7.3}$$

$$R = r^2 \tag{7.4}$$

where r is the field reflectance, R is the (intensity) reflectivity and $F = \begin{bmatrix} F_{11} & F_{12} \\ F_{21} & F_{22} \end{bmatrix}$.

Appendix C – System for Characterization of Optoacoustic Bandwidth

The schematic for the system used to characterize the optoacoustic bandwidth of the detectors presented in this thesis is depicted in Figure 7.2. The system comprises of two major parts: excitation part and read-out part. Table 7.1 list of all the equipment used for the system.

In the excitation part, a 515-nm ns laser beam was resized and spatially filtered by a pin hole with diameter of 25 µm. The beam was then sent to an inverted microscope, and the output from the microscope objective was focused to a spot of approximately 2.2 µm in diameter. A coverslip with 200-nm-thick gold layer sputtered on the surface was used as a target, which generates optoacoustic signal upon focusing of the laser beam onto the gold layer. The optoacoustic signal generated by this method has ultra-broad bandwidth, wherein the variation in frequency components varies by only 3 dB from 1 MHz up to 2 GHz [179]. Within the sensitive band of the detectors presented in this thesis (< 200 MHz), the bandwidth of the gold-based point source can be considered to be flat. The laser power used was approximately 150 µW to avoid permanent damage of the gold layer.

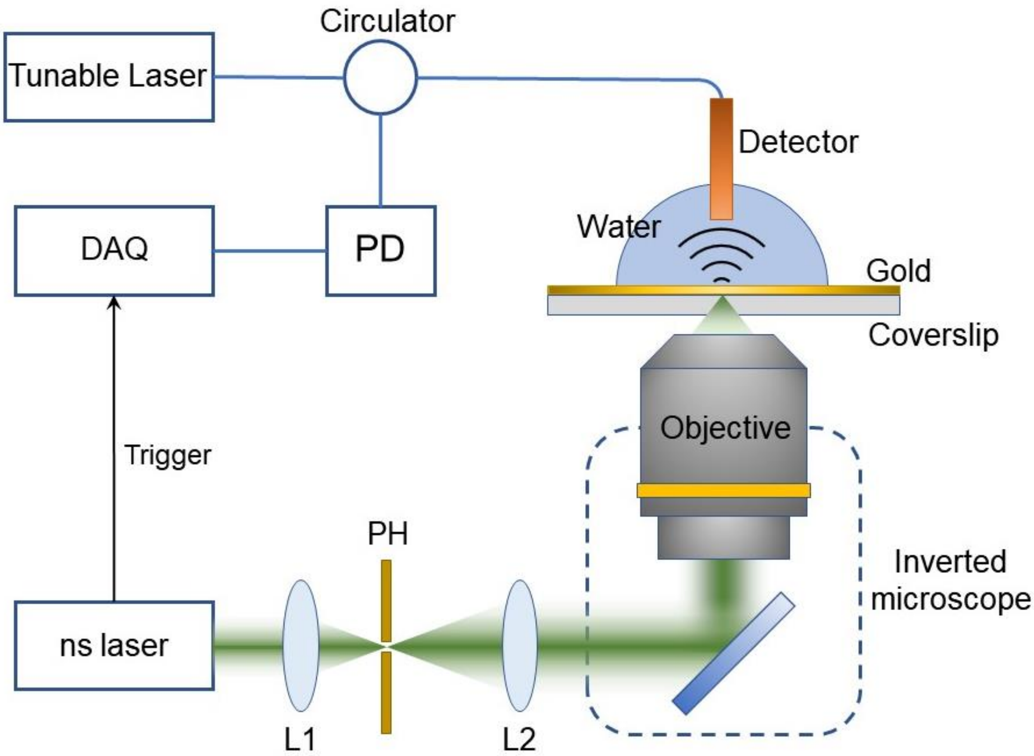

Figure 7.2 - Schematic of the setup for bandwidth characterization. ns laser: nanosecond laser. L1 and L2 are two lenses used for beam resizing. PH: pinhole. PD: photodetector. DAQ: data acquisition.

In the read-out part, the optical detectors were interrogated by a tunable laser, which emitted radiation with wavelength corresponding to the position of maximum slope in the resonant dip of the working detectors. The reflected signal from the optical detectors was directed to a balanced photodetector via a fiber circulator. The AC electrical output of the photodetector was digitalized by a data acquisition (DAQ) board for processing. For characterization of the piezoelectric transducers, the piezoelectric transducers were powered by a custom-made DC voltage power supply. The output of the piezoelectric transducers was connected directly to the DAQ board.

Table 7.1 - Equipment listing for bandwidth characterization

#	Name	Model	Manufacturer
1	ns laser	Flare PQ HP GR 2k-500	Innolight
2	Microscope objective	PLN 10x, NA = 0.25	Olympus
3	Tunable laser	ITUNX 1550B	Thorlabs Inc.
4	Photodetector	PDB480C-AC	Thorlabs Inc.
5	Fiber circulator	CTR1550PM-APC	Thorlabs Inc.
6	DAQ board	CSE123G2	Gage

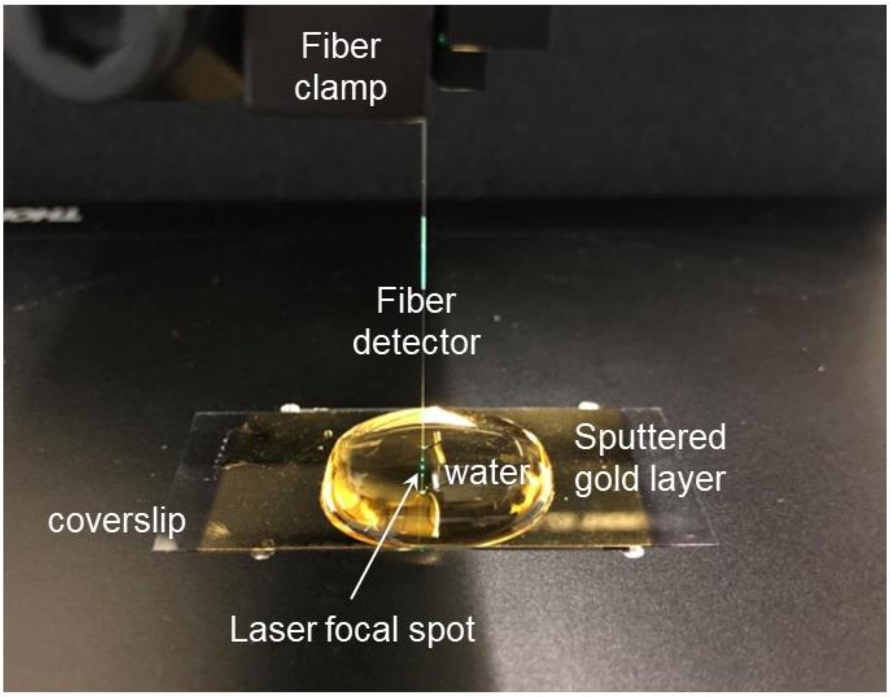

Figure 7.3 - Image of the EER during bandwidth characterization.

Appendix D – System for Characterization of Optoacoustic Sensitivity

The system for sensitivity characterization is similar to bandwidth characterization, except for the gold-sputtered coverslip is replace by a black vinyl-taped coverslip (Figure 7.4). The black vinyl tape has higher optical absorption and higher damage threshold than the gold layer, thus allowing the generation of stronger optoacoustic signal under stronger illumination (laser power of approximately 310 μW).

The reference detector was a needle hydrophone purchased from Precision Acoustic, UK with a thin polyvinylidene fluoride (PVDF) of 0.5-mm diameter as the sensitive element. The optoacoustic signal generated by the vinyl tape has frequency extending up to 60 MHz, which is large enough to sufficiently cover the calibrated bandwidth of the needle hydrophone (10-30 MHz).

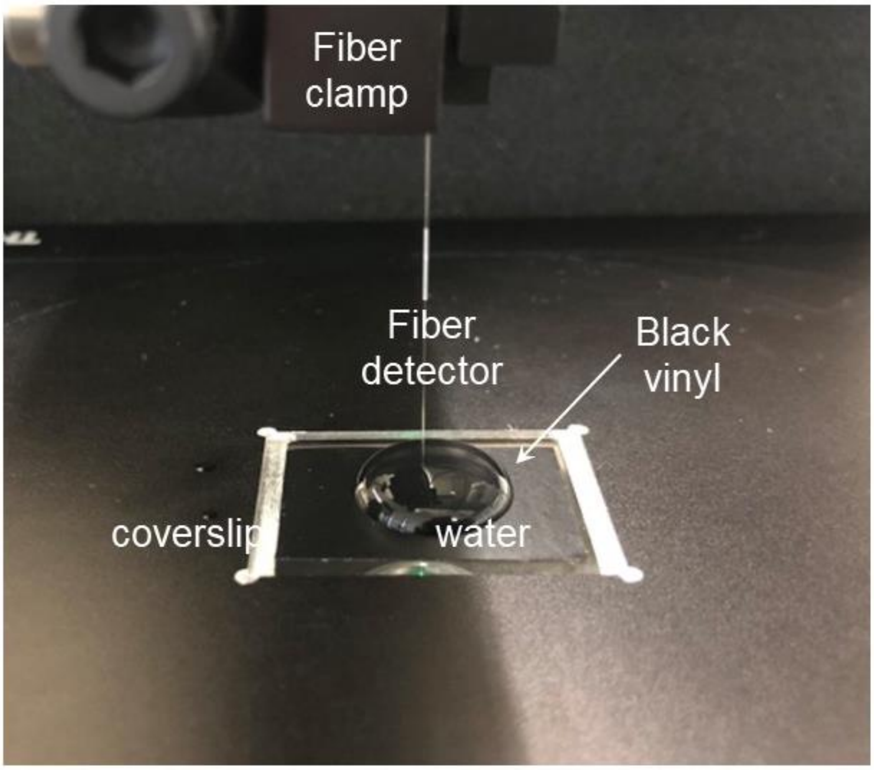

Figure 7.4 - Image of the EER during sensitivity characterization.

Appendix E – System for Characterization of Optoacoustic Point Spread Function

To characterize the PSF of the EER, an optoacoustic point source was generated by the gold film similar to the bandwidth characterization experiment. Instead of keeping the detector stationary, the EER was line-scanned over the point source by a motorized linear stage (MTS50-Z8, Thorlabs Inc.) as depicted in Figure 7.5.

The line scan data was back projected in the frequency domain [145] to reconstruct the PSF. To retrieve the PSF with high accuracy, the scanning length was keep maintaining at the value of 3-times the distance D so that it always covers the acceptance angle of the EER. The scanning step size was adjusted to follow Nyquist-Shannon sampling conditions with the step size is less than 5 times the FWHM of the reconstructed PSF.

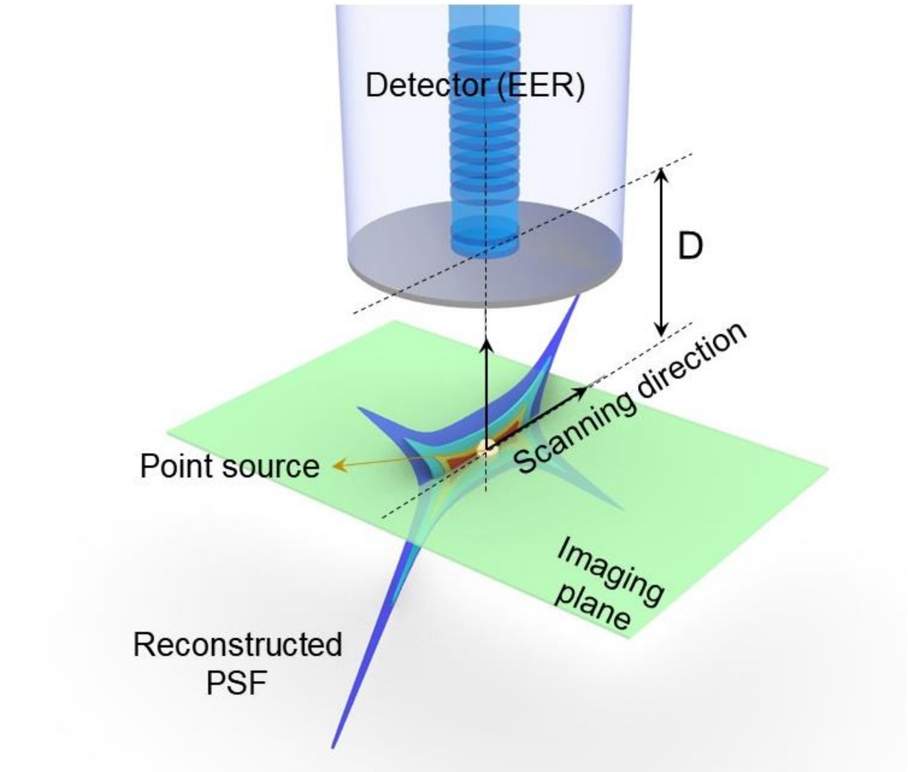

Figure 7.5 - Schematic of the experiment for PSF characterization. D is the distance between the detection surface of the detector and the imaging plane that contains the point source and being parralel to the detection surface.

Appendix F – Types of Acoustic Waves Recorded during a Line Scan

During a line scan, the detector is mostly in an offset position to the point source, so optoacoustic wave hits the detection surface of the detector at an oblique incidence. The oblique incidence at the liquid-solid interface would generate several types of acoustic wave propagating in the detectors (Figure 7.4):

1. Ordinary longitudinal wave (OL): generated at the detection aperture, propagating in the detector at longitudinal sound velocity

2. Ordinary shear wave (OS): generated at the detection aperture, propagating in the detector at shear sound speed

3. Surface acoustic wave (SAW): generated at the position that satisfies the critical angle condition for SAW generation and propagating toward the detection aperture at SAW speed (which is roughly equal to shear sound speed)

4. Edge diffracted wave (ED): generated by acoustic diffraction at the physical edge of the detector's body, which then can propagate toward the sensitive region of the detector at various speed: longitudinal sound speed (LED), shear sound speed (SED) and Rayleigh sound speed (RED).

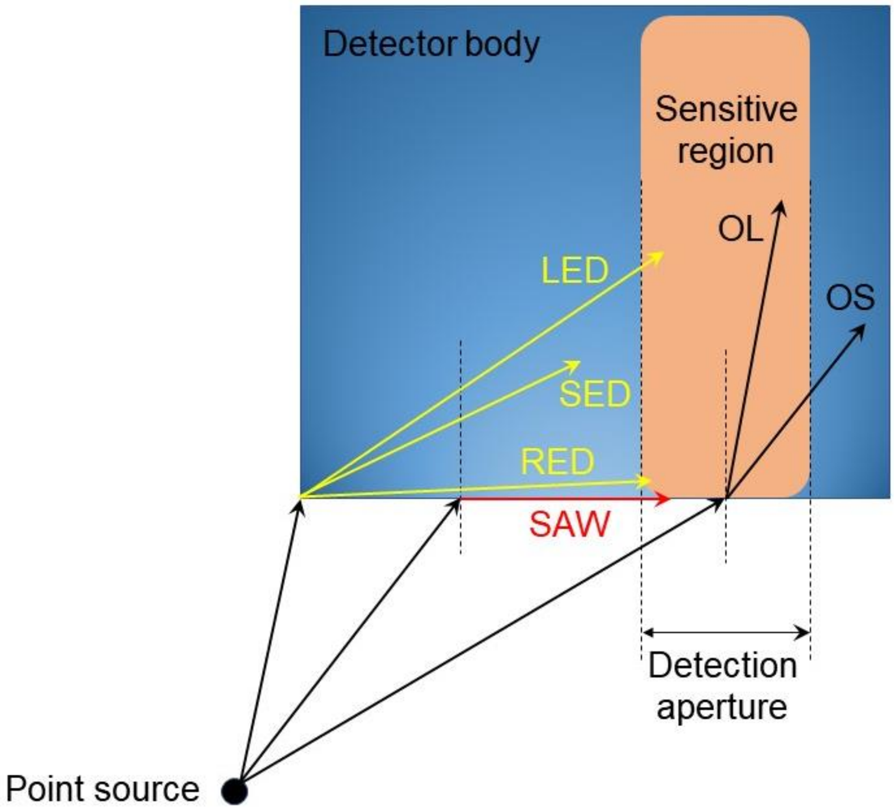

Figure 7.6 - Types of acoustic waves generated in a line scan. OL (Ordinary longitudinal wave) and OS (Ordinary shear wave) are generated directly at the detection aperture and being instantaneously detected. SAW (Surface acoustic wave) is generated outside of the detection aperture under proper incident angle and propagating toward the aperture. Edge waves (ED) is generated by acoustic diffraction at the edge of the detector and propagating toward the sensitive region at different sound speed: longitudinal (LED), shear (SED) and Rayleigh (or surface wave – RED).

Publications

1. Tai-Anh La, Okan Ülgen, Rami Shnaiderman, Vasilis Ntziachristos, “Bragg grating etalon-based optical fiber for ultrasound and optoacoustic detection”, (accepted in **Nature Communiations**, 2024)

2. Tai-Anh La, Rami Shnaiderman, Vasilis Ntziachristos, “Amplification of light-ultrasound interaction in Fiber Bragg Grating for enhanced ultrasonic sensitivity”, (manuscript in submission)

3. Okan Ülgen, Tai-Anh La, Christian Zakian, Vasilis Ntziachristos, “Optical-fiber-based polymer resonator for optoacoustic micro-tomography”, (manuscript in submission)

Reprint Permissions

Parts of this work have been principally accepted by peer-review journals or are currently in the process of submission. These elements were included in this thesis as granted through the author rights in the copyright transfer agreements of the respective publishing journals. Specifically, figures in chapter 4 were adapted from [180] and figures in chapter 5 were adapted from [181].

Bibliography

1 Bell, A. G. On the production and reproduction of sound by light. *American Journal of Science* **118** (1880). https://doi.org:10.2475/ajs.s3-20.118.305

2 Wang, L. V. Multiscale photoacoustic microscopy and computed tomography. *Nature Photonics* **3**, 503-509 (2009). https://doi.org:10.1038/nphoton.2009.157

3 Ntziachristos, V. Going deeper than microscopy: the optical imaging frontier in biology. *Nature Methods* **7**, 603-614 (2010). https://doi.org:10.1038/nmeth.1483

4 Park, J. *et al.* Quadruple ultrasound, photoacoustic, optical coherence, and fluorescence fusion imaging with a transparent ultrasound transducer. *Proceedings of the National Academy of Sciences* **118**, e1920879118 (2021). https://doi.org:10.1073/pnas.1920879118

5 Murray, C. J. L. & Lopez, A. D. Mortality by cause for eight regions of the world: Global Burden of Disease Study. *The Lancet* **349**, 1269-1276 (1997). https://doi.org:10.1016/s0140-6736(96)07493-4

6 Burke, A. P. *et al.* Coronary Risk Factors and Plaque Morphology in Men with Coronary Disease Who Died Suddenly. *New England Journal of Medicine* **336**, 1276-1282 (1997). https://doi.org:10.1056/nejm199705013361802

7 Prati, F. *et al.* Expert review document on methodology, terminology, and clinical applications of optical coherence tomography: physical principles, methodology of image acquisition, and clinical application for assessment of coronary arteries and atherosclerosis. *European Heart Journal* **31**, 401-415 (2009). https://doi.org:10.1093/eurheartj/ehp433

8 Yang, J.-M. *et al.* Simultaneous functional photoacoustic and ultrasonic endoscopy of internal organs in vivo. *Nature Medicine* **18**, 1297-1302 (2012). https://doi.org:10.1038/nm.2823

9 Joon-Mo Yang, K. M., Hao-Chung Yang, Qifa Zhou, K. Kirk Shung, and Lihong V. Wang. Photoacoustic endoscopy. *OPTICS LETTERS* **34** (2009).

10 Seeger, M., Dehner, C., Jüstel, D. & Ntziachristos, V. Label-free concurrent 5-modal microscopy (Co5M) resolves unknown spatio-temporal processes in wound healing. *Communications Biology* **4**, 1040 (2021). https://doi.org:10.1038/s42003-021-02573-5

11 Li, H. *et al.* Disposable ultrasound-sensing chronic cranial window by soft nanoimprinting lithography. *Nature Communications* **10** (2019). https://doi.org:10.1038/s41467-019-12178-6

12 Razansky, V. N. a. D. Molecular Imaging by Means of Multispectral Optoacoustic Tomography (MSOT). *Chemical Review* **110**, 2783–2794 (2010).

13 Yao, J. & Wang, L. V. Sensitivity of photoacoustic microscopy. *Photoacoustics* **2**, 87-101 (2014). https://doi.org:10.1016/j.pacs.2014.04.002

14 Wu, L. V. W. a. H. *Biomedical Optics: Principles and Imaging*. (John Wiley & Sons, 2012).

15 Szabo, T. L. *Diagnostic Ultrasound Imaging: Inside Out*. (Elsevier Academic Press, 2004).

16 Sushilov, N. V. & Cobbold, R. S. C. Frequency–domain wave equation and its time–domain solutions in attenuating media. *The Journal of the Acoustical Society of America* **115**, 1431-1436 (2004). https://doi.org:10.1121/1.1675817

17 Deán-Ben, X. L., Razansky, D. & Ntziachristos, V. The effects of acoustic attenuation in optoacoustic signals. *Physics in Medicine and Biology* **56**, 6129-6148 (2011). https://doi.org:10.1088/0031-9155/56/18/021

18 Cobbold, R. S. C. *Foundations of Biomedical Ultrasound*. (Oxford University Press, 2007).

19 Zhang, C., Maslov, K. & Wang, L. V. Subwavelength-resolution label-free photoacoustic microscopy of optical absorption in vivo. *Optics Letters* **35**, 3195-3197 (2010). https://doi.org:10.1364/OL.35.003195

20 Zhang, H. F., Maslov, K., Stoica, G. & Wang, L. V. Functional photoacoustic microscopy for high-resolution and noninvasive in vivo imaging. *Nature Biotechnology* **24**, 848-851 (2006). https://doi.org:10.1038/nbt1220

21 Zhang, H. F., Maslov, K. & Wang, L. V. In vivo imaging of subcutaneous structures using functional photoacoustic microscopy. *Nature Protocols* **2**, 797-804 (2007). https://doi.org:10.1038/nprot.2007.108

22 Yao, J. & Wang, L. V. Photoacoustic microscopy. *Laser & Photonics Reviews* **7**, 758-778 (2013). https://doi.org:https://doi.org/10.1002/lpor.201200060

23 Seeger, M. *et al.* Pushing the boundaries of optoacoustic microscopy by total impulse response characterization. *Nature Communications* **11**, 2910 (2020). https://doi.org:10.1038/s41467-020-16565-2

24 Hu, L. V. W. a. S. Photoacoustic Tomography: In Vivo Imaging from Organelles to Organs. *Science* **335**, 1458-1462 (2012). https://doi.org:10.1126/science.1216210

25 Wang, L. V. & Yao, J. A practical guide to photoacoustic tomography in the life sciences. *Nature Methods* **13**, 627-638 (2016). https://doi.org:10.1038/nmeth.3925

26 Mitcham, T., Dextraze, K., Taghavi, H., Melancon, M. & Bouchard, R. Photoacoustic imaging driven by an interstitial irradiation source. *Photoacoustics* **3**, 45-54 (2015). https://doi.org:https://doi.org/10.1016/j.pacs.2015.02.002

27 Xu, M. & Wang, L. V. Analytic explanation of spatial resolution related to bandwidth and detector aperture size in thermoacoustic or photoacoustic reconstruction. *Physical Review E* **67** (2003). https://doi.org:10.1103/PhysRevE.67.056605

28 Xu, M. & Wang, L. V. Universal back-projection algorithm for photoacoustic computed tomography. *Physical Review E* **71**, 016706 (2005). https://doi.org:10.1103/PhysRevE.71.016706

29 Luís Deán-Ben, X. & Razansky, D. Adding fifth dimension to optoacoustic imaging: volumetric time-resolved spectrally enriched tomography. *Light: Science & Applications* **3**, e137-e137 (2014). https://doi.org:10.1038/lsa.2014.18

30 Omar, M., Soliman, D., Gateau, J. & Ntziachristos, V. Ultrawideband reflection-mode optoacoustic mesoscopy. *Optics Letters* **39** (2014). https://doi.org:10.1364/ol.39.003911

31 Omar, M., Gateau, J. & Ntziachristos, V. Raster-scan optoacoustic mesoscopy in the 25–125 MHz range. *Optics Letters* **38** (2013). https://doi.org:10.1364/ol.38.002472

32 Gateau, J., Caballero, M. Á. A., Dima, A. & Ntziachristos, V. Three-dimensional optoacoustic tomography using a conventional ultrasound linear detector array: Whole-body tomographic system for small animals. *Medical Physics* **40**, 013302 (2013). https://doi.org:https://doi.org/10.1118/1.4770292

33 Omar, M., Aguirre, J. & Ntziachristos, V. Optoacoustic mesoscopy for biomedicine. *Nature Biomedical Engineering* **3**, 354-370 (2019). https://doi.org:10.1038/s41551-019-0377-4

34 Haedicke, K. *et al.* High-resolution optoacoustic imaging of tissue responses to vascular-targeted therapies. *Nature Biomedical Engineering* **4**, 286-297 (2020). https://doi.org:10.1038/s41551-020-0527-8

35 Hindelang, B. *et al.* Enabling precision monitoring of psoriasis treatment by optoacoustic mesoscopy. *Science Translational Medicine* **14**, eabm8059 (2022). https://doi.org:doi:10.1126/scitranslmed.abm8059

36 He, H. *et al.* Fast raster-scan optoacoustic mesoscopy enables assessment of human melanoma microvasculature in vivo. *Nature Communications* **13**, 2803 (2022). https://doi.org:10.1038/s41467-022-30471-9

37 Schwarz, M. *et al.* Optoacoustic Dermoscopy of the Human Skin: Tuning Excitation Energy for Optimal Detection Bandwidth With Fast and Deep Imaging in vivo. *IEEE Transactions on Medical Imaging* **36**, 1287-1296 (2017). https://doi.org:10.1109/tmi.2017.2664142

38 Aguirre, J. *et al.* Precision assessment of label-free psoriasis biomarkers with ultra-broadband optoacoustic mesoscopy. *Nature Biomedical Engineering* **1** (2017). https://doi.org:10.1038/s41551-017-0068

39 ANSI Z136.1, – Safe Use of Lasers. Laser Institute of America. (2007).

40 Liao, C. K., Li, M. L. & Li, P. C. Optoacoustic imaging with synthetic aperture focusing and coherence weighting. *Optics Letters* **29**, 2506-2508 (2004). https://doi.org:10.1364/OL.29.002506

41 Li, M.-L., Zhang, H. F., Maslov, K., Stoica, G. & Wang, L. V. Improved in vivo photoacoustic microscopy based on a virtual-detector concept. *Optics Letters* **31**, 474-476 (2006). https://doi.org:10.1364/OL.31.000474

42 Bahaa E. A. Saleh, M. C. T. *Fundamentals of Photonics*. (John Wiley & Sons, Inc., 1991).

43 Edward Zhang, J. L., and Paul Beard. Backward-mode multiwavelength photoacoustic scanner using a planar Fabry–Perot polymer film ultrasound sensor for high-resolution three-dimensional imaging of biological tissues. *Applied Optics* **47**, 561-577 (2008).

44 Morris, P., Hurrell, A., Shaw, A., Zhang, E. & Beard, P. A Fabry–Pérot fiber-optic ultrasonic hydrophone for the simultaneous measurement of temperature and acoustic pressure. *The Journal of the Acoustical Society of America* **125**, 3611-3622 (2009). https://doi.org:10.1121/1.3117437

45 Ansari, R., Zhang, E. Z., Desjardins, A. E. & Beard, P. C. All-optical forward-viewing photoacoustic probe for high-resolution 3D endoscopy. *Light: Science & Applications* **7** (2018). https://doi.org:10.1038/s41377-018-0070-5

46 Erdogan, T. Fiber Grating Spectra. *Journal of Lightwave Technology* **15**, 1277-1294 (1997).

47 Shnaiderman, R. *Silicon Photonics Sensors of Ultrasound for Optoacoustic Imaging* PhD thesis, Technischen Universität München, (2021).

48 Meltz, G., Morey, W. W. & Glenn, W. H. Formation of Bragg gratings in optical fibers by a transverse holographic method. *Optics Letters* **14**, 823-825 (1989). https://doi.org:10.1364/OL.14.000823

49 Malo, B., Hill, K. O., Bilodeau, F., Johnson, D. C. & Albert, J. Point-by-point fabrication of micro-Bragg gratings in photosensitive fibre using single excimer pulse refractive index modification techniques. *Electronics Letters* **29**, 1668-1669 (1993). <https://digital-library.theiet.org/content/journals/10.1049/el_19931110>.

50 Broer, M. M., Cone, R. L. & Simpson, J. R. Ultraviolet-induced distributed-feedback gratings in Ce3+-doped silica optical fibers. *Optics Letters* **16**, 1391-1393 (1991). https://doi.org:10.1364/OL.16.001391

51 Dong, L., Archambault, J. L., Reekie, L., Russell, P. S. J. & Payne, D. N. Bragg gratings in Ce3+-doped fibers written by a single excimer pulse. *Optics Letters* **18**, 861-863 (1993). https://doi.org:10.1364/OL.18.000861

52 Bilodeau, F. *et al.* Ultraviolet-light photosensitivity in Er3+–Ge-doped optical fiber. *Optics Letters* **15**, 1138-1140 (1990). https://doi.org:10.1364/OL.15.001138

53 Williams, D. L., Ainslie, B. J., Armitage, J. R., Kashyap, R. & Campbell, R. Enhanced UV photosensitivity in boron codoped germanosilicate fibres. *Electronics Letters* **29**, 45-47 (1993). <https://digital-library.theiet.org/content/journals/10.1049/el_19930030>.

54 Lemaire, P. J., Atkins, R. M., Mizrahi, V. & Reed, W. A. High pressure H₂ loading as a technique for achieving ultrahigh UV photosensitivity and thermal sensitivity in GeO₂ doped optical fibres. *Electronics Letters* **29**, 1191-1193 (1993). <https://digital-library.theiet.org/content/journals/10.1049/el_19930796>.

55 Bilodeau, F. *et al.* Photosensitization of optical fiber and silica-on-silicon/silica waveguides. *Optics Letters* **18**, 953-955 (1993). https://doi.org:10.1364/OL.18.000953

56 Hill, K. O., Malo, B., Bilodeau, F., Johnson, D. C. & Albert, J. Bragg gratings fabricated in monomode photosensitive optical fiber by UV exposure through a phase mask. *Applied Physics Letters* **62**, 1035-1037 (1993). https://doi.org:10.1063/1.108786

57 Anderson, D. Z., Mizrahi, V., Erdogan, T. & White, A. E. Production of in-fibre gratings using a diffractive optical element. *Electronics Letters* **29**, 566-568 (1993). <https://digital-library.theiet.org/content/journals/10.1049/el_19930379>.

58 Mihailov, S. J. *et al.* Fiber Bragg gratings made with a phase mask and 800-nm femtosecond radiation. *Optics Letters* **28**, 995-997 (2003). https://doi.org:10.1364/OL.28.000995

59 Murphy, T. E., Hastings, J. T. & Smith, H. I. Fabrication and characterization of narrow-band Bragg-reflection filters in silicon-on-insulator ridge waveguides. *Journal of Lightwave Technology* **19**, 1938-1942 (2001). https://doi.org:10.1109/50.971688

60 Wang, X., Grist, S., Flueckiger, J., Jaeger, N. A. F. & Chrostowski, L. Silicon photonic slot waveguide Bragg gratings and resonators. *Optics Express* **21**, 19029-19039 (2013). https://doi.org:10.1364/OE.21.019029

61 Zubkova, E. *et al.* Integrated Bragg waveguides as an efficient optical notch filter on silicon nitride platform. *Journal of Physics: Conference Series* **917**, 062042 (2017). https://doi.org:10.1088/1742-6596/917/6/062042

62 Husko, C., Ducharme, A., Fahrenkopf, N. M. & Guest, J. R. Phase-shifted Bragg gratings in a foundry silicon nitride platform. *OSA Continuum* **4**, 933-939 (2021). https://doi.org:10.1364/OSAC.413672

63 Bischoff, K. *et al.* Integration of Bragg gratings in aerosol-jetted polymer optical waveguides for strain monitoring capabilities. *Optics Letters* **48**, 1778-1781 (2023). https://doi.org:10.1364/OL.481801

64 Park, T.-H., Kim, S.-M. & Oh, M.-C. Polymer-waveguide Bragg-grating Devices Fabricated Using Phase-mask Lithography. *Curr. Opt. Photon.* **3**, 401-407 (2019).

65 Painchaud, Y. *et al.* in *Advanced Photonics Congress.* BW2E.3 (Optica Publishing Group).

66 Painchaud, Y., Aubé, M., Brochu, G. & Picard, M. J. in *Advanced Photonics & Renewable Energy* (2010).

67 Rayleigh, L. CXII. The problem of the whispering gallery. *The London, Edinburgh, and Dublin Philosophical Magazine and Journal of Science* **20**, 1001-1004 (1910). https://doi.org:10.1080/14786441008636993

68 Rayleigh, L. IX. Further applications of Bessel's functions of high order to the Whispering Gallery and allied problems. *The London, Edinburgh, and Dublin Philosophical Magazine and Journal of Science* **27**, 100-109 (1914). https://doi.org:10.1080/14786440108635067

69 Matsko, A. B. & Ilchenko, V. S. Optical resonators with whispering-gallery modes-part I: basics. *IEEE Journal of Selected Topics in Quantum Electronics* **12**, 3-14 (2006). https://doi.org:10.1109/jstqe.2005.862952

70 Gorodetsky, M. L., Savchenkov, A. A. & Ilchenko, V. S. Ultimate Q of optical microsphere resonators. *Optics Letters* **21**, 453-455 (1996). https://doi.org:10.1364/OL.21.000453

71 Vollmer, F., Arnold, S. & Keng, D. Single virus detection from the reactive shift of a whispering-gallery mode. *Proceedings of the National Academy of Sciences* **105**, 20701-20704 (2008). https://doi.org:10.1073/pnas.0808988106

72 Baaske, M. D. & Vollmer, F. Optical observation of single atomic ions interacting with plasmonic nanorods in aqueous solution. *Nature Photonics* **10**, 733-739 (2016). https://doi.org:10.1038/nphoton.2016.177

73 Pöllinger, M., O'Shea, D., Warken, F. & Rauschenbeutel, A. Ultrahigh-Q Tunable Whispering-Gallery-Mode Microresonator. *Physical Review Letters* **103**, 053901 (2009). https://doi.org:10.1103/PhysRevLett.103.053901

74 Asano, M. *et al.* Observation of optomechanical coupling in a microbottle resonator. *Laser & Photonics Reviews* **10**, 603-611 (2016). https://doi.org:https://doi.org/10.1002/lpor.201500243

75 Gu, F. *et al.* Single whispering-gallery mode lasing in polymer bottle microresonators via spatial pump engineering. *Light: Science & Applications* **6**, e17061-e17061 (2017). https://doi.org:10.1038/lsa.2017.61

76 Sumetsky, M., Dulashko, Y. & Windeler, R. S. Optical microbubble resonator. *Optics Letters* **35**, 898-900 (2010). https://doi.org:10.1364/OL.35.000898

77 Watkins, A., Ward, J., Wu, Y. & Nic Chormaic, S. Single-input spherical microbubble resonator. *Optics Letters* **36**, 2113-2115 (2011). https://doi.org:10.1364/OL.36.002113

78 Armani, D. K., Kippenberg, T. J., Spillane, S. M. & Vahala, K. J. Ultra-high-Q toroid microcavity on a chip. *Nature* **421**, 925-928 (2003). https://doi.org:10.1038/nature01371

79 Knapper, K. A., Heylman, K. D., Horak, E. H. & Goldsmith, R. H. Chip-Scale Fabrication of High-Q All-Glass Toroidal Microresonators for Single-Particle Label-Free Imaging. *Advanced Materials* **28**, 2945-2950 (2016). https://doi.org:https://doi.org/10.1002/adma.201504976

80 Lee, H. *et al.* Chemically etched ultrahigh-Q wedge-resonator on a silicon chip. *Nature Photonics* **6**, 369-373 (2012). https://doi.org:10.1038/nphoton.2012.109

81 Gavartin, E., Verlot, P. & Kippenberg, T. J. A hybrid on-chip optomechanical transducer for ultrasensitive force measurements. *Nature Nanotechnology* **7**, 509-514 (2012). https://doi.org:10.1038/nnano.2012.97

82 Ksendzov, A. & Lin, Y. Integrated optics ring-resonator sensors for protein detection. *Optics Letters* **30**, 3344-3346 (2005). https://doi.org:10.1364/OL.30.003344

83 Lin, S. & Crozier, K. B. Trapping-Assisted Sensing of Particles and Proteins Using On-Chip Optical Microcavities. *ACS Nano* **7**, 1725-1730 (2013). https://doi.org:10.1021/nn305826j

84 Khaled, E. E. M., Hill, S. C., Barber, P. W. & Chowdhury, D. Q. Near-resonance excitation of dielectric spheres with plane waves and off-axis Gaussian beams. *Applied Optics* **31**, 1166-1169 (1992). https://doi.org:10.1364/AO.31.001166

85 Wang, S.-J., Yang, Y.-D. & Huang, Y.-Z. Analysis of coupled microcircular resonators coupled to a bus waveguide with high output efficiency. *Optics Letters* **35**, 1953-1955 (2010). https://doi.org:10.1364/OL.35.001953

86 Son, S.-J., Kim, S., Yu, N. E. & Ko, D.-K. Bus-waveguide-width Dependence of Evanescent Wave Coupling in a Microring Resonator. *Curr. Opt. Photon.* **5**, 538-543 (2021).

87 Ming, C. & Vahala, K. in *Technical Digest. Summaries of papers presented at the Conference on Lasers and Electro-Optics. Postconference Technical Digest (IEEE Cat. No.01CH37170).* 114-116.

88 MacDonald, A. J. R. *et al.* Optical microscope and tapered fiber coupling apparatus for a dilution refrigerator. *Review of Scientific Instruments* **86**, 013107 (2015). https://doi.org:10.1063/1.4905682

89 Sherwood, T. *et al.* Microring resonators on side-polished optical fiber. *IEEE Photonics Technology Letters* **17**, 2107-2109 (2005). https://doi.org:10.1109/LPT.2005.854405

90 Conti, G. N. *et al.* in *CLEO/Europe and EQEC 2011 Conference Digest.* CK_P9 (Optica Publishing Group).

91 Liu, G. *et al.* Low-loss prism-waveguide optical coupling for ultrahigh-Q low-index monolithic resonators. *Optica* **5**, 219-226 (2018). https://doi.org:10.1364/OPTICA.5.000219

92 John D. Joannopoulos, S. G. J., Joshua N. Winn, Robert D. Meade. *Photonic Crystals: Molding the Flow of Light*. Second Edition edn, (Princeton University Press, 2008).

93 Hermannsson, P. G. *Guide Mode Resonator for Refractive Index Sensing* PhD thesis, DTU, (2015).

94 Fan, S. & Joannopoulos, J. D. Analysis of guided resonances in photonic crystal slabs. *Physical Review B* **65** (2002). https://doi.org:10.1103/PhysRevB.65.235112

95 Akahane, Y., Asano, T., Song, B.-S. & Noda, S. High-Qphotonic nanocavity in a two-dimensional photonic crystal. *Nature* **425**, 944-947 (2003). https://doi.org:10.1038/nature02063

96 Dorfner, D. F. *et al.* Silicon photonic crystal nanostructures for refractive index sensing. *Applied Physics Letters* **93** (2008). https://doi.org:10.1063/1.3009203

97 Debnath, K. *et al.* Ultrahigh-Q photonic crystal cavities in silicon rich nitride. *Optics Express* **25**, 27334-27340 (2017). https://doi.org:10.1364/OE.25.027334

98 Foreman, M. R., Swaim, J. D. & Vollmer, F. Whispering gallery mode sensors. *Advances in Optics and Photonics* **7** (2015). https://doi.org:10.1364/aop.7.000168

99 Dwivedi, S., heer, H. D. & Bogaerts, W. A Compact All-Silicon Temperature Insensitive Filter for WDM and Bio-Sensing Applications. *IEEE Photonics Technology Letters* **25**, 2167-2170 (2013). https://doi.org:10.1109/LPT.2013.2282715

100 Amir Rosenthal, D. R., and Vasilis Ntziachristos. Wideband optical sensing using pulse interferometry. *Optics Express* **20** (2012).

101 Hu, L., Liu, G., Zhu, Y., Luo, X. & Han, M. Laser Frequency Noise Cancelation in a Phase-Shifted Fiber Bragg Grating Ultrasonic Sensor System Using a Reference Grating Channel. *IEEE Photonics Journal* **8**, 1-8 (2016). https://doi.org:10.1109/jphot.2016.2527018

102 Qi Wu, Y. O. High-sensitivity ultrasonic phase-shifted fiber Bragg grating balanced sensing system. *OPTICS EXPRESS* **20**, 28353-28362 (2012).

103 Riobó, L. *et al.* Noise reduction in resonator-based ultrasound sensors by using a CW laser and phase detection. *Optics Letters* **44** (2019). https://doi.org:10.1364/ol.44.002677

104 Zhang, Z., Zhao, P., Lin, P. & Sun, F. Thermo-optic coefficients of polymers for optical waveguide applications. *Polymer* **47**, 4893-4896 (2006). https://doi.org:https://doi.org/10.1016/j.polymer.2006.05.035

105 de Cea, M., Atabaki, A. H. & Ram, R. J. Power handling of silicon microring modulators. *Optics Express* **27**, 24274-24285 (2019). https://doi.org:10.1364/OE.27.024274

106 Ding, M. *et al.* Photothermal effects in phase shifted FBG with varied light wavelength and intensity. *Optics Express* **24**, 25370-25379 (2016). https://doi.org:10.1364/OE.24.025370

107 Preisser, S. *et al.* All-optical highly sensitive akinetic sensor for ultrasound detection and photoacoustic imaging. *Biomedical Optics Express* **7** (2016). https://doi.org:10.1364/boe.7.004171

108 Ülgen, O., Shnaiderman, R., Zakian, C. & Ntziachristos, V. Interferometric optical fiber sensor for optoacoustic endomicroscopy. *Journal of Biophotonics* **14**, e202000501 (2021). https://doi.org:https://doi.org/10.1002/jbio.202000501

109 Jathoul, A. P. *et al.* Deep in vivo photoacoustic imaging of mammalian tissues using a tyrosinase-based genetic reporter. *Nature Photonics* **9**, 239-246 (2015). https://doi.org:10.1038/nphoton.2015.22

110 Ashkenazi, S. V. T. a. S. Toward a highly sensitive polymer waveguide fiber Fabry–Pérot ultrasound detector. *Journal of Biomedical Optics* **23** (2018). https://doi.org:10.1117/1.Jbo.23.10.106008

111 Guggenheim, J. A. *et al.* Ultrasensitive plano-concave optical microresonators for ultrasound sensing. *Nature Photonics* **11**, 714-719 (2017). https://doi.org:10.1038/s41566-017-0027-x

112 Rosenthal, A. *et al.* Sensitive interferometric detection of ultrasound for minimally invasive clinical imaging applications. *Laser & Photonics Reviews* **8**, 450-457 (2014). https://doi.org:10.1002/lpor.201300204

113 Yaras, Y. S., Yildirim, D. K., Kocaturk, O. & Degertekin, F. L. Sensitivity and phase response of FBG based acousto-optic sensors for real-time MRI applications. *OSA Continuum* **3** (2020). https://doi.org:10.1364/osac.385969

114 Yaras, Y. S. *et al.* Acousto-Optic Catheter Tracking Sensor for Interventional MRI Procedures. *IEEE Transactions on Biomedical Engineering* **66**, 1148-1154 (2019). https://doi.org:10.1109/tbme.2018.2868830

115 Lukas Chrostowski, M. H. *Silicon Photonics Design: From Devices to Systems*. (Cambridge University Press, 2015).

116 Ling, T., Chen, S.-L. & Guo, L. J. High-sensitivity and wide-directivity ultrasound detection using high Q polymer microring resonators. *Applied Physics Letters* **98** (2011). https://doi.org:10.1063/1.3589971

117 Chistiakova, M. V. & Armani, A. M. Photoelastic ultrasound detection using ultra-high-Q silica optical resonators. *Optics Express* **22** (2014). https://doi.org:10.1364/oe.22.028169

118 Kim, K. H. *et al.* Air-coupled ultrasound detection using capillary-based optical ring resonators. *Scientific Reports* **7** (2017). https://doi.org:10.1038/s41598-017-00134-7

119 Basiri-Esfahani, S., Armin, A., Forstner, S. & Bowen, W. P. Precision ultrasound sensing on a chip. *Nature Communications* **10** (2019). https://doi.org:10.1038/s41467-018-08038-4

120 Maxwell, A. *et al.* Polymer Microring Resonators for High-Frequency Ultrasound Detection and Imaging. *IEEE Journal of Selected Topics in Quantum Electronics* **14**, 191-197 (2008). https://doi.org:10.1109/jstqe.2007.914047

121 Huang, S.-W. *et al.* Low-noise wideband ultrasound detection using polymer microring resonators. *Applied Physics Letters* **92** (2008). https://doi.org:10.1063/1.2929379

122 Noda, S., Chutinan, A. & Imada, M. Trapping and emission of photons by a single defect in a photonic bandgap structure. *Nature* **407**, 608-610 (2000). https://doi.org:10.1038/35036532

123 Song, B.-S., Noda, S., Asano, T. & Akahane, Y. Ultra-high-Q photonic double-heterostructure nanocavity. *Nature Materials* **4**, 207-210 (2005). https://doi.org:10.1038/nmat1320

124 Kuramochi, E. *et al.* Ultrahigh-Q photonic crystal nanocavities realized by the local width modulation of a line defect. *Applied Physics Letters* **88** (2006). https://doi.org:10.1063/1.2167801

125 Zhu, E. Y., Rewcastle, C., Gad, R., Qian, L. & Levi, O. Refractive-index-based ultrasound sensing with photonic crystal slabs. *Optics Letters* **44** (2019). https://doi.org:10.1364/ol.44.002609

126 Zhu, X. *et al.* Ultrasonic detection based on polarization-dependent optical reflection. *Opt Lett* **42**, 439-441 (2017). https://doi.org:10.1364/OL.42.000439

127 Pereira, L. M. *et al.* Phase-Shifted Bragg Grating Inscription in PMMA Microstructured POF Using 248-nm UV Radiation. *Journal of Lightwave Technology* **35**, 5176-5184 (2017). https://doi.org:10.1109/jlt.2017.2771436

128 Westerveld, W. J. *et al.* Sensitive, small, broadband and scalable optomechanical ultrasound sensor in silicon photonics. *Nature Photonics* **15**, 341-345 (2021). https://doi.org:10.1038/s41566-021-00776-0

129 Li, H., Dong, B., Zhang, Z., Zhang, H. F. & Sun, C. A transparent broadband ultrasonic detector based on an optical micro-ring resonator for photoacoustic microscopy. *Scientific Reports* **4** (2014). https://doi.org:10.1038/srep04496

130 Morris, P. *A Fabry-Perot fibre-optic hydrophone for the characterisation of ultrasound fields* PhD thesis, University College London, (2008).

131 Weise, W., Wilkens, V. & Koch, C. Frequency response of fiber-optic multilayer hydrophones: experimental investigation and finite element simulation. *IEEE Transactions on Ultrasonics, Ferroelectrics, and Frequency Control* **49**, 937-946 (2002). https://doi.org:10.1109/TUFFC.2002.1020164

132 Zhang, E. & Beard, P. *Characteristics of optimized fibre-optic ultrasound receivers for minimally invasive photoacoustic detection*. Vol. 9323 PWB (SPIE, 2015).

133 Colchester, R. J. *et al.* All-Optical Rotational Ultrasound Imaging. *Scientific Reports* **9** (2019). https://doi.org:10.1038/s41598-019-41970-z

134 Amir Rosenthal, M. Á. A. C., Stephan Kellnberger, Daniel Razansky, and Vasilis Ntziachristos. Spatial characterization of the response of a silica optical fiber to wideband ultrasound. *Optics Letters* **37**, 3174-3176 (2012).

135 Hazan, Y., Levi, A., Nagli, M. & Rosenthal, A. Silicon-photonics acoustic detector for optoacoustic micro-tomography. *Nature Communications* **13** (2022). https://doi.org:10.1038/s41467-022-29179-7

136 Zhu, E. Y. *et al.* Real-time ultrasound sensing with a mode-optimized photonic crystal slab. *Optics Letters* **46** (2021). https://doi.org:10.1364/ol.430431

137 Pan, J. *et al.* Parallel interrogation of the chalcogenide-based micro-ring sensor array for photoacoustic tomography. *Nat Commun* **14**, 3250 (2023). https://doi.org:10.1038/s41467-023-39075-3

138 Nagli, M. *et al.* Silicon photonic acoustic detector (SPADE) using a silicon nitride microring resonator. *Photoacoustics* **32** (2023). https://doi.org:10.1016/j.pacs.2023.100527

139 Wißmeyer, G. *All-optical Ultrasound Detection for Optoacoustic Imaging* PhD thesis, TUM, (2019).

140 Soliman, D. M. *Augmented microscopy: Development and application of high-resolution optoacoustic and multimodal imaging techniques for label-free biological observation* Ph.D. thesis, Technischen Universität München, (2016).

141 Soliman, D., Tserevelakis, G. J., Omar, M. & Ntziachristos, V. Combining microscopy with mesoscopy using optical and optoacoustic label-free modes. *Scientific Reports* **5**, 12902 (2015). https://doi.org:10.1038/srep12902

142 Shnaiderman, R. *et al.* A submicrometre silicon-on-insulator resonator for ultrasound detection. *Nature* **585**, 372-378 (2020). https://doi.org:10.1038/s41586-020-2685-y

143 Shnaiderman, R. *et al.* Silicon-Photonics Point Sensor for High-Resolution Optoacoustic Imaging. *Advanced Optical Materials* (2021). https://doi.org:10.1002/adom.202100256

144 Wissmeyer, G., Soliman, D., Shnaiderman, R., Rosenthal, A. & Ntziachristos, V. All-optical optoacoustic microscope based on wideband pulse interferometry. *Optics Letters* **41** (2016). https://doi.org:10.1364/ol.41.001953

145 Mustafa, Q. *et al.* In Vivo Three-Dimensional Raster Scan Optoacoustic Mesoscopy Using Frequency Domain Inversion. *IEEE Transactions on Medical Imaging* **40**, 3349-3357 (2021). https://doi.org:10.1109/TMI.2021.3084356

146 Rosenthal, A., Ntziachristos, V. & Razansky, D. Acoustic Inversion in Optoacoustic Tomography: A Review. *Curr Med Imaging Rev* **9**, 318-336 (2013). https://doi.org:10.2174/15734056113096660006

147 Yuan, X., Dazi, F. & Wang, L. V. Exact frequency-domain reconstruction for thermoacoustic tomography. I. Planar geometry. *IEEE Transactions on Medical Imaging* **21**, 823-828 (2002). https://doi.org:10.1109/TMI.2002.801172

148 Yang, J.-M. *et al.* Catheter-based photoacoustic endoscope. *Journal of Biomedical Optics* **19**, 066001 (2014).

149 Zhao, T., Desjardins, A. E., Ourselin, S., Vercauteren, T. & Xia, W. Minimally invasive photoacoustic imaging: Current status and future perspectives. *Photoacoustics* **16**, 100146 (2019). https://doi.org:https://doi.org/10.1016/j.pacs.2019.100146

150 Pietrow, P. K. *et al.* Pain after Percutaneous Nephrolithotomy: Impact of Nephrostomy Tube Size. *Journal of Endourology* **17**, 411-414 (2003). https://doi.org:10.1089/089277903767923218

151 Carroll, L. *et al.* Photonic Packaging: Transforming Silicon Photonic Integrated Circuits into Photonic Devices. *Applied Sciences* **6** (2016). https://doi.org:10.3390/app6120426

152 Marchetti, R., Lacava, C., Carroll, L., Gradkowski, K. & Minzioni, P. Coupling strategies for silicon photonics integrated chips [Invited]. *Photonics Research* **7** (2019). https://doi.org:10.1364/prj.7.000201

153 Mu, X., Wu, S., Cheng, L. & Fu, H. Y. Edge Couplers in Silicon Photonic Integrated Circuits: A Review. *Applied Sciences* **10** (2020). https://doi.org:10.3390/app10041538

154 Amir Rosenthal, D. R., and Vasilis Ntziachristos. High-sensitivity compact ultrasonic detector based on a pi-phase-shifted fiber Bragg grating. *Optics Letters* **36**, 1833-1835 (2011). https://doi.org:10.1364/OL.36.001833

155 Antman, Y., Clain, A., London, Y. & Zadok, A. Optomechanical sensing of liquids outside standard fibers using forward stimulated Brillouin scattering. *Optica* **3** (2016). https://doi.org:10.1364/optica.3.000510

156 Beard, P. C., Perennes, F. & Mills, T. N. Transduction mechanisms of the Fabry-Perot polymer film sensing concept for wideband ultrasound detection. *IEEE Transactions on Ultrasonics, Ferroelectrics, and Frequency Control* **46**, 1575-1582 (1999). https://doi.org:10.1109/58.808883

157 Gao, H. *et al.* Investigation on the Thermo-Optic Coefficient of Silica Fiber Within a Wide Temperature Range. *Journal of Lightwave Technology* **36**, 5881-5886 (2018). https://doi.org:10.1109/JLT.2018.2875941

158 Bashan, G. *et al.* Forward stimulated Brillouin scattering and opto-mechanical non-reciprocity in standard polarization maintaining fibres. *Light: Science & Applications* **10** (2021). https://doi.org:10.1038/s41377-021-00557-y

159 Hu, P., Li, L., Lin, L. & Wang, L. V. Spatiotemporal Antialiasing in Photoacoustic Computed Tomography. *IEEE Transactions on Medical Imaging* **39**, 3535-3547 (2020). https://doi.org:10.1109/TMI.2020.2998509

160 Wissmeyer, G., Pleitez, M. A., Rosenthal, A. & Ntziachristos, V. Looking at sound: optoacoustics with all-optical ultrasound detection. *Light: Science & Applications* **7** (2018). https://doi.org:10.1038/s41377-018-0036-7

161 Finlay, M. C. *et al.* Through-needle all-optical ultrasound imaging in vivo: a preclinical swine study. *Light: Science & Applications* **6**, e17103-e17103 (2017). https://doi.org:10.1038/lsa.2017.103

162 Westerveld, W. *Silicon photonic micro-ring resonators to sense strain and ultrasound* PhD thesis, Technische Universiteit Delft, (2014).

163 Chen, S.-M. T. a. C.-L. Side-polished fibers. *Applied Optics* **31** (1992).

164 Zhao, J. *et al.* Rough Side-Polished Fiber With Surface Scratches for Sensing Applications. *IEEE Photonics Journal* **7**, 1-7 (2015). https://doi.org:10.1109/jphot.2015.2423288

165 Li, C. *et al.* A sensitivity-enhanced flexible acoustic sensor using side-polished fiber Bragg grating. *Measurement* **117**, 252-257 (2018). https://doi.org:10.1016/j.measurement.2017.12.027

166 Heo, J., Lee, K. T., Kim, R. K. & Baac, H. W. Side-Polished Fiber-Optic Line Sensor for High-Frequency Broadband Ultrasound Detection. *Sensors (Basel)* **19** (2019). https://doi.org:10.3390/s19020398

167 Zhang, P. *et al.* Side-polished flexible SPR sensor modified by graphene with in situ temperature self-compensation. *Biomed Opt Express* **10**, 215-225 (2019). https://doi.org:10.1364/BOE.10.000215

168 Li, C. *et al.* D-Shaped Fiber Bragg Grating Ultrasonic Hydrophone With Enhanced Sensitivity and Bandwidth. *Journal of Lightwave Technology* **37**, 2100-2108 (2019). https://doi.org:10.1109/jlt.2019.2898233

169 Rosenthal, A., Razansky, D. & Ntziachristos, V. High-sensitivity compact ultrasonic detector based on a pi-phase-shifted fiber Bragg grating. *Optics Letters* **36**, 1833-1835 (2011). https://doi.org:10.1364/OL.36.001833

170 Fallahkhair, A. B., Li, K. S. & Murphy, T. E. Vector Finite Difference Modesolver for Anisotropic Dielectric Waveguides. *Journal of Lightwave Technology* **26**, 1423-1431 (2008). https://doi.org:10.1109/JLT.2008.923643

171 Kellnberger, S. *et al.* Optoacoustic microscopy at multiple discrete frequencies. *Light: Science & Applications* **7** (2018). https://doi.org:10.1038/s41377-018-0101-2

172 Shnaiderman, R. *et al.* Fiber interferometer for hybrid optical and optoacoustic intravital microscopy. *Optica* **4** (2017). https://doi.org:10.1364/optica.4.001180

173 Seeger, M., Stiel, A. C. & Ntziachristos, V. In vitro optoacoustic flow cytometry with light scattering referencing. *Scientific Reports* **11** (2021). https://doi.org:10.1038/s41598-021-81584-y

174 Jin, T. *et al.* On-Chip Multicolor Photoacoustic Imaging Flow Cytometry. *Analytical Chemistry* **93**, 8134-8142 (2021). https://doi.org:10.1021/acs.analchem.0c05218

175 Erfanzadeh, M. & Zhu, Q. Photoacoustic imaging with low-cost sources; A review. *Photoacoustics* **14**, 1-11 (2019). https://doi.org:10.1016/j.pacs.2019.01.004

176 Stylogiannis, A. *et al.* Continuous wave laser diodes enable fast optoacoustic imaging. *Photoacoustics* **9**, 31-38 (2018). https://doi.org:10.1016/j.pacs.2017.12.002

177 Erfanzadeh, M., Kumavor, P. D. & Zhu, Q. Laser scanning laser diode photoacoustic microscopy system. *Photoacoustics* **9**, 1-9 (2018). https://doi.org:10.1016/j.pacs.2017.10.001

178 Guan, B.-O., Jin, L., Ma, J., Liang, Y. & Bai, X. Flexible fiber-laser ultrasound sensor for multiscale photoacoustic imaging. *Opto-Electronic Advances* **4** (2021). https://doi.org:10.29026/oea.2021.200081

179 Strohm, E. M., Berndl, E. S. L. & Kolios, M. C. High frequency label-free photoacoustic microscopy of single cells. *Photoacoustics* **1**, 49-53 (2013). https://doi.org:https://doi.org/10.1016/j.pacs.2013.08.003

180 Tai-Anh La, O. Ü., Rami Shnaiderman, Vasilis Ntziachristos. Bragg grating etalon-based optical fiber for ultrasound and optoacoustic detection. *accepted in Nature Communications* (2024).

181 Tai-Anh La, R. S., Vasilis Ntziachristos. Amplification of light-ultrasound interaction in Fiber Bragg Grating for enhanced ultrasonic sensitivity. (manuscript in submission).